Supermassive Black Hole Masses with multi-object Reverberation Mapping

Umang Malik

A thesis submitted for the degree of
Doctor of Philosophy
of The Australian National University
Research School of Astronomy and Astrophysics

July 2023

Declaration

I hereby declare that the work in this thesis is that of the candidate alone, except where indicated below or in the text of the thesis. The work was undertaken between February 2019 and July 2023 at the Australian National University (ANU), Canberra. It has not been submitted in whole or in part for any other degree at this or any other university.

This thesis has been submitted as a Thesis by Compilation in accordance with the relevant ANU policies. Each of the three main chapters is therefore a completely self-contained article, which has been published in, or submitted to, a peer-reviewed journal. The status of each article and extent of the contribution of the candidate to the research and authorship is indicated below:

- Chapter 2: **Malik, U.**; Sharp, R.; Martini, P.; Davis, T. M.; Tucker, B. E.; Yu, Z.; Penton, A.; Lewis, G. F.; Calcino, J.; *Observational window effects on multi-object reverberation mapping*, 2022, MNRAS, 516, 3238-3253.

  U. Malik conducted all simulations and analysis, wrote all text and created all figures.

  Part of Section 2.2.2 in this chapter is published in the Monthly Notices of the Royal Astronomical Society (in Section 2 and A1) as: Penton, A.; **Malik, U.**; Davis, T. M.; Martini, P.; Yu, Z.; Sharp, R.; Lidman, C.; Tucker, B. E.; Hoormann, J. K. et al. (61 additional authors not shown), *OzDES Reverberation Mapping Program: Lag recovery reliability for 6-yr C* IV *analysis*, 2022, MNRAS, 509, 4008-4023.

  U. Malik wrote all text in these sections of this paper.

- Chapter 3: **Malik, U.**; Sharp, R.; Penton, A.; Yu, Z.; Martini, P.; Lidman, C.; Tucker, B. E.; Davis, T. M.; Lewis, G. F.; Aguena, M.; Allam, S.; Alves, O.; Andrade-Oliveira, F.; Asorey, J.; Bacon, D.; Bertin, E.; Bocquet, S.; Brooks, D.; Burke, D. L.; Carnero Rosell, A.; Carollo, D.; Carrasco Kind, M.; Carretero, J.; Costanzi, M.; da Costa, L. N.; Pereira, M. E. S.; De Vicente, J.; Desai, S.; Diehl, H. T.; Doel, P.; Everett, S.; Ferrero, I.; Frieman, J.; García-Bellido, J.; Gerdes, D. W.; Gruen, D.; Gruendl, R. A.; Gschwend, J.; Hinton, S. R.; Hollowood, D. L.; Honscheid, K.; James, D. J.; Kuehn, K.;

Marshall, J. L.; Mena-Fernández, J.; Menanteau, F.; Miquel, R.; Ogando, R. L. C.; Palmese, A.; Paz-Chinchón, F.; Pieres, A.; Plazas Malagón, A. A.; Raveri, M.; Rodriguez-Monroy, M.; Romer, A. K.; Sanchez, E.; Scarpine, V.; Sevilla-Noarbe, I.; Smith, M.; Soares-Santos, M.; Suchyta, E.; Swanson, M. E. C.; Tarle, G.; Taylor, G.; Tucker, D. L.; Weaverdyck, N.; Wilkinson, R. D.; *OzDES Reverberation Mapping Program: Hβ lags from the 6-year survey*, 2023, MNRAS, 520, 2009-2023.

U. Malik conducted all analysis, wrote all text and created all figures. Data was obtained by OzDES/DES.

- Chapter 4: **Malik, U.**; Sharp, R.; Penton, A.; Yu, Z.; Martini, P.; Tucker, B. E.; Davis, T. M.; Lewis, G. F.; Lidman, C.; Aguena M.; Alves, O.; Annis, J.; Asorey, J; Bacon, D.; Brooks, D.; Carnero Rosell, A.; Carretero, J.; Cheng, T.-Y.; da Costa, L. N.; Pereira, M. E. S.; De Vicente, J.; Doel, P.; Ferrero, I.; Frieman, J.; Giannini, G.; Gruen, D.; Gruendl, R. A.; Hinton, S. R.; Hollowood, D. L.; James, D. J.; Kuehn, K.; Marshall, J. L.; Mena-Fernández, J.; Menanteau, F.; Miquel, R.; Ogando, R. L. C.; Palmese, A.; Pieres, A.; Plazas Malagón, A. A.; Reil, K.; Romer, A. K.; Sanchez, E.; Schubnell, M.; Smith, M.; Suchyta, E.; Swanson, M. E. C.; Tarle, G.; To, C.; Weaverdyck, N.; Wiseman, P.; *OzDES Reverberation Mapping Program: Stacking analysis with Hβ, Mg*II *and C*IV, submitted to MNRAS in July 2023

  U. Malik conducted all analysis, wrote all text and created all figures. Data was obtained by OzDES/DES and the data reduction from calibrated spectra to light curves was done by A. Penton and Z. Yu.

The candidate also made contributions to the following articles during the course of the candidature:

- Yu, Z.; Martini, P.; Penton, A.; Davis, T. M.; Kochanek, C. S.; Lewis, G. F.; Lidman, C.; **Malik, U.**; Sharp, R.; Tucker, B. E. et al. (48 additional authors not shown), *OzDES Reverberation Mapping Program: MgII Lags and R-L relation*, 2023, MNRAS, 522, 4132

- Eltvedt, A. M.; Shanks, T.; Metcalfe, N.; Ansarinejad, B.; Barrientos, L. F.; Sharp, R.; **Malik, U.** et al. (18 additional authors not shown), *The VST ATLAS Quasar Survey I: Catalogue*, 2023, MNRAS, 521, 3384

- Grayling, M.; Gutiérrez, C. P.; Sullivan, M.; Wiseman, P.; Vincenzi, M. et al. (including **Malik, U.**; 70 additional authors not shown), *Core-collapse Supernovae in the Dark Energy Survey: Luminosity Functions and Host Galaxy Demographics*, 2023, MNRAS, 520, 684

- Vincenzi, M.; Sullivan, M.; Möller, A.; Armstrong, P.; Bassett, B. A.; Brout, D. et al. (including **Malik, U.**; 77 additional authors not shown), *The Dark Energy Survey Supernova Program: Cosmological biases from supernova photometric classification*, 2023, MNRAS, 518, 1106

- Dixon, M.; Lidman, C.; Mould, J.; Kelsey, L.; Brout, D.; Möller, A.; Wiseman, P. et al. (including **Malik, U.**; 70 additional authors not shown), *Using host galaxy spectroscopy to explore systematics in the standardization of Type Ia supernovae*, 2022, MNRAS, 517, 4291

- Möller, A.; Smith, M.; Sako, M.; Sullivan, M.; Vincenzi, M.; Wiseman, P. et al. (including **Malik, U.**; 76 additional authors not shown), *The dark energy survey 5-yr photometrically identified type Ia supernovae*, 2022, MNRAS, 514, 5159

- Tucker, D. L.; Wiesner, M. P.; Allam, S. S.; Soares-Santos, M.; Bom, C. R. et al. (including **Malik, U.**; 130 additional authors not shown), *SOAR/Goodman Spectroscopic Assessment of Candidate Counterparts of the LIGO/Virgo Event GW190814*, 2022, ApJ, 929, 115

- Guise, E.; Hönig, S. F.; Almeyda, T.; Horne, K.; Kishimoto, M.; Aguena, M. et al. (including **Malik, U.**; 58 additonal authors not shown), *Multiwavelength optical and NIR variability analysis of the Blazar PKS 0027-426*, 2022, MNRAS, 510, 3145

- DES Collaboration et al. (including **Malik, U.**; 111 additional authors not shown) *Dark Energy Survey Year 3 results: A 2.7% measurement of baryon acoustic oscillation distance scale at redshift 0.835*, 2022, Physical Review D, 105, 043512

- Zovaro, H. R. M.; Riseley, C. J.; Taylor, P.; Nesvadba, N. P. H.; Galvin, T. J.; **Malik, U.**; Kewley, L. J. *Revisiting the giant radio galaxy ESO 422-G028 - I. Discovery of a neutral inflow and recent star formation in a restarted giant*, 2022, MNRAS, 509, 4997

- Penton, A.; **Malik, U.**; Davis, T. M.; Martini, P.; Yu, Z.; Sharp, R.; Lidman, C.; Tucker, B. E.; Hoormann, J. K. et al. (61 additional authors not shown), *OzDES reverberation mapping program: Lag recovery reliability for 6-yr C*IV *analysis*, 2022, MNRAS, 509, 4008

- Carnero Rosell, A.; Rodriguez-Monroy, M.; Crocce, M.; Elvin-Poole, J.; Porredon, A.; Ferrero, I. et al. (including **Malik, U.**; 102 additional authors not shown), *Dark Energy Survey Year 3 results: galaxy sample for BAO measurement*, 2022, MNRAS, 509, 778

- Yu, Z.; Martini, P.; Penton, A.; Davis, T. M.; **Malik, U.**; Lidman, C.; Tucker, B. E.; Sharp, R. et al. (58 additional authors not shown), *OzDES Reverberation Mapping Program: the first MgII lags from 5 yr of monitoring*, 2021, MNRAS, 507, 3771

- Morgan, R.; Soares-Santos, M.; Annis, J.; Herner, K.; Garcia, A.; Palmese, A.; Drlica-Wagner, A. et al. (including **Malik, U.**; 95 additional authors not shown), *Constraints on the Physical Properties of GW190814 through Simulations Based on DECam Follow-up Observations by the Dark Energy Survey*, 2020, ApJ, 901, 83

- Lidman, C.; Tucker, B. E.; Davis, T. M.; Uddin, S. A.; Asorey, J.; Bolejko, K.; DES Collaboration et al. (including **Malik, U.**; 97 additional authors not shown), *OzDES multi-object fibre spectroscopy for the Dark Energy Survey: results and second data release*, 2020, MNRAS, 496, 19

Umang Malik

Acknowledgements

I have wanted to be an astrophysicist since I was 8 years old. It is with immense pride that I present this thesis to you, after managing to retain and rejoice in the sense of wonder that was fostered within me 18 years ago. The past four years have been an absolute roller-coaster ride with euphoric highs an rock-bottom lows. I owe a debt of gratitude to so many for helping to keep me on the rails. Not many PhD students can say that they survived a global pandemic, bushfires, and their early 20s with their sanity intact—but I can, thanks to the following people.

Firstly, I want to thank my primary supervisor, Rob Sharp, for taking my 21-year-old self under your wing. I'm grateful for your patience, unwavering support, and British humour (which, I won't lie, took me a moment to understand). I will fondly look back upon our many nights of (unfortunately weather-affected) observing. I thank my co-supervisor, Brad Tucker, for your contagious enthusiasm and support through everything. Thanks to the guidance from you both, I leave Stromlo not only as a better scientist, but also a stronger person, ready to tackle whatever challenges may come.

I have been fortunate to be part of the OzDES Reverberation Mapping team, with Paul Martini, Tamara Davis, Chris Lidman, Geraint Lewis, Zhefu Yu, Andrew Penton, and Janie Hoormann. I have felt continuously encouraged and inspired by each member of this team, and I am very proud of the science we have done together.

Next, I would like to thank my Stromlo peers. Each day on the mountain (or locked-down at home) has been such a joy in your company. I particularly cherish the friendships I formed with Georgie Taylor, Stephanie Monty, Piyush Sharda, Harrison Abbot, Rajsekhar Mohapatra, Lyla Jung, Madeleine McKenzie, Jamie Soon, Aldo Mura, Adam Rains, Henry Zovaro, and Noelia Martinez. Badminton, birthdays, and BBQs with you all made Canberra home. An extra special thank you to Georgie—my office mate, travel buddy, soul sister—for literally everything. It can't be put into words.

I'd also like to thank my friends outside astronomy—Beth, Manik, Sonali, Elona and Deepa—for providing much-needed distraction from the PhD bubble and always being there for me. To my partner, Shash—thank you for sharing your calm with me and bringing fun into my life when I needed it most. I'm looking forward to post-PhD life with you.

Finally, I will forever be grateful to my parents and my brother for nurturing my passion and encouraging me to follow it. I could not have achieved any of this without your constant love and support. Thank you.

Abstract

Reverberation mapping uses light echoes to infer the masses of supermassive black holes (SMBH) in active galactic nuclei (AGN). By effectively substituting for spatial resolution with temporal resolution, this technique overcomes the limits faced by other methods reliant on high angular resolution instruments, allowing the study of SMBH evolution over cosmic history. Reverberation measurements have been used to constrain the relationship between the size of the broad-line region and luminosity of AGN. This Radius-Luminosity ($R - L$) relation is used to estimate single-epoch virial black hole masses, and has been proposed for use to standardise AGN to determine cosmological distances. However, the intensity of observational resources required has impeded greater application.

This has necessitated the commencement of multi-object spectroscopic surveys, monitoring an order of magnitude more AGN and extending to high redshifts. In this thesis, I explore the intricacies of performing reverberation mapping on this 'industrial-scale', and deliver results from the six-year Australian Dark Energy Survey (OzDES) Reverberation Mapping Program; one of two multi-object surveys completed to-date.

There are complex interactions between the window function, emission-line lag and variability timescales, which are further complicated by time dilation with redshift. My comprehensive simulations demonstrate the impact of each component of the global observational window function on reverberation lag recovery for a diverse population of AGN. I find the presence of a significant seasonal gap dominates the lag recovery efficacy of any given campaign strategy; more so than the cadence or baseline of the data.

With an appreciation of the challenges imposed by the limited spectroscopic cadence and significant seasonal gaps in the OzDES data, I successfully recover reverberation lags for eight AGN at $0.12 < z < 0.71$ from the OzDES Hβ sample, probing higher redshifts than the bulk of Hβ measurements made to date. The results from this multi-object spectroscopic survey are consistent with previous measurements made by dedicated source-by-source campaigns (which had significantly higher cadence), and with the observed dependence on accretion rate.

Given the overall lag recovery efficacy of only ∼10% for the entire OzDES sample, I use the novel stacking technique to extract the maximum information from our data. The data sparsity is ameliorated through the stacking of cross correlations from physically similar sources to recover average reverberation lags. I present average lags recovered for the Hβ, Mg II and C IV samples, and multi-line measurements for redshift bins where two lines are accessible. Our results demonstrate that stacking has the potential to improve upon constraints on the $R - L$ relation, which have been derived using only individual source measurements thus far.

This thesis reveals both the challenges and the potential of industrial-scale reverberation mapping. With the imminence of the next generation of multi-object surveys, including LSST, TiDES and SDSS-V, this work highlights the urgency to prioritise observing fields with longer seasonal visibility—not only to improve lag recovery for more sources, but also to mitigate signal aliasing. Although I demonstrate the ability of stacking to partially compensate for data sparsity, only by optimising the observational window function can we harness the full potential of reverberation mapping.

Contents

1

Introduction

Active galactic nuclei (AGN) are the extremely luminous cores of active galaxies, which are believed to be powered by supermassive black holes that are accreting material. In fact, distant AGN, more commonly known as quasars, are the most luminous objects in the Universe. There is strong evidence that supermassive black holes (SMBHs) reside in the hearts of most, if not all, galaxies. Although most galaxies are presently inactive, it is posited that they went through an active phase at some point in their history, and that SMBH and galaxy growth are correlated. Given their ubiquity and high luminosities, AGN can be used to probe the growth and evolution of SMBHs over most of cosmic history.

The first observations of the extragalactic sources we now know as AGN were made eighty years ago, however, explanation of their peculiar spectra evaded astronomers for years. The discovery of more exotic AGN phenomena, such as radio jets, further complicated consolidation of this class of object. We now understand that AGN encompass a variety of sources, but all exhibit the following characteristics: strong emission lines (narrow, broad, or both) and variability across all wavelengths (notably in X-rays). This variable continuum emission is reprocessed by various regions around the central SMBH, producing light 'echoes'. By making repeated observations across different wavelengths we can trace these light echoes and use them to measure the size of the emitting region. This technique is known as reverberation mapping (RM).

Presently, RM is the only method which can be used to directly measure SMBH masses beyond our local Universe, as it does not require high spatial resolution to resolve the gravitational sphere-of-influence of the SMBH. Although this is a very powerful method with valuable applications, it has been underutilised due to the intensity of observational resources required. More recently, multiplexed spectroscopy has facilitated the concurrent observation of hundreds of AGN. The Australian Dark Energy Survey (OzDES) employed this novel technology to conduct one of the first multi-object RM surveys, pushing to new regimes. In this thesis, I will review the past RM efforts before presenting results from the pioneering OzDES RM Program, and explore how future multi-object surveys can perform to their full potential.

1.1 Active Galactic Nuclei

The first class of AGN to be discovered, now known as Seyfert galaxies, appeared to be regular spiral galaxies but with bright point-like centres that produced peculiar spectra exhibiting high-ionisation broad emission lines superimposed on stellar-like absorption spectra (Seyfert 1943). Then, in the 1960's, wide-field radio surveys identified radio emission from point sources not associated with any known objects. Star-like optical counterparts were later detected by Matthews & Sandage (1963), referred to as 'quasi-stellar objects' and later shortened to 'quasars'. However, the spectra had broad emission lines indicative of fast-moving gas, as observed for Seyfert galaxies. Schmidt (1963) measured the spectrum of one of these sources, 3C 273, and deduced that the emission lines were red-shifted; indicating the source originated at a cosmological distance, and thus was far brighter and further away than any other object discovered until then.

Seyfert galaxies and quasars comprise the two largest groups of active galaxies. Initially it was not known that the two classes were physically related. The general distinction between them is that the host galaxies of Seyferts are visible, as the radiation emitted by the nucleus is comparable to that emitted by stars in the galaxy, whereas in quasars, the nuclear emission is greater by a factor of 100 or more; therefore appearing as point sources (Peterson 1997).

The radiation emitted from these compact (*i.e.* unresolved) sources is far too great to be attributed to stars and gas alone. Rapid flux variations over timescales as short as minutes, as seen from X-ray observations, imply that the size of the emitting region must be smaller this light-crossing time (McHardy 1988; Mushotzky et al. 1993). Given these size constraints, and mass constraints from the Eddington limit, the only plausible mechanism for how such large amounts of radiation could be generated within this small volume is the accretion of matter by a supermassive black hole at the centre of the galaxy (Hoyle & Fowler 1963; Salpeter 1964; Zel'dovich 1964; Lynden-Bell 1969; Rees 1984). The presence of these SMBHs has since been confirmed observationally (Ferrarese & Ford 2005).

Various types of AGN have been identified. They are distinguished by the observed luminosity, presence of radio emission, and from the presence and width of certain emission lines in their spectra. Other types of AGN include radio galaxies, blazars, and low-ionisation nuclear emission-line regions galaxies (LINERs). One of the hallmarks of all AGN is their variable continuum emission across the entire electromagnetic spectrum. Spectroscopically, AGN can be further categorised as Type 1, from the presence of broad emission lines, or Type 2, if only narrow emission lines are present (Peterson 1997).

The unified model for AGN attributes the differences between the various types of AGN to the orientation of the black hole and its surrounding material relative to the observer (Antonucci 1993; Urry & Padovani 1995). In this model, AGN are surrounded by highly ionised gas present in the high-density broad-line region (on the order of light days to weeks in size), and low-density narrow-line region, as well as a dusty torus. The central black hole is located at the centre and is accreting the surrounding material. As illustrated in Figure 1.1, depending on the orientation of the torus, and thus the degree to which the radiation emitted from the interior is obscured, different types of AGN can be observed. Other models and more complex factors are discussed by Netzer (2015), however this simple model suffices here.

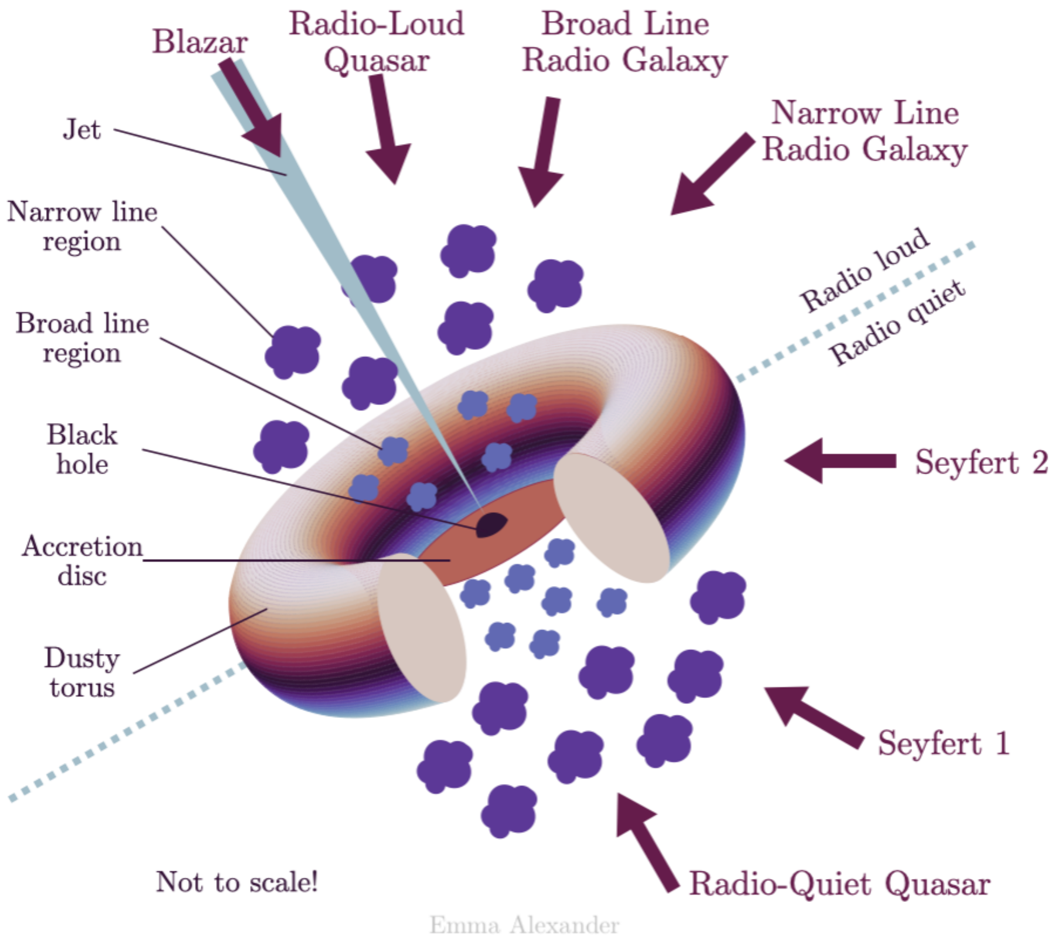

Figure 1.1: Schematic diagram of the unified model for AGN. The arrows indicate which type of AGN would be observed from various viewing angles. Credit: Emma Alexander, licensed under CC-BY.

1.1.1 Co-evolution with host galaxy

A number of empirical relationships have been found between the SMBH mass and certain host galaxy properties, such as the stellar velocity dispersion of the bulge; the $M_{\rm BH} - \sigma^{*}$ relation (Ferrarese & Merritt 2000; Gebhardt et al. 2000a), and with the bulge luminosity; the $M_{\rm BH} - L_{\rm bulge}$ relation (Magorrian et al. 1998), for both quiescent and active galaxies. These relations suggest that the evolution of AGN and their host galaxies are closely linked.

One way in which AGN and their host galaxies may co-evolve is through the process of AGN feedback (Silk & Rees 1998; King 2003). Feedback can occur through radiative processes, e.g. in which the radiation emitted by the AGN heats the interstellar medium (ISM), or through kinetic processes, e.g. in which the AGN drives outflows of gas and dust from the galaxy. Negative feedback may regulate the growth of the host galaxy by driving gas and dust outwards or preventing the ISM from cooling and collapsing, thereby quenching star formation. Alternately, positive AGN feedback induced by winds or outflows can compress the ISM and trigger star formation. However, feedback is not observed to play a significant role in co-evolution for all AGN, as it is dependent on factors such as galaxy type and size, and mergers. For a review of AGN-host co-evolution and feedback processes see Kormendy & Ho (2013) and Fabian (2012).

1.2 Supermassive black hole masses

To understand the co-evolution of SMBHs and their host galaxies, and the growth of SMBHs over cosmic time, we require accurate and precise SMBH mass measurements. There are several methods that can be used to directly measure the mass of SMBHs:

- Stellar dynamics: At the centre of our galaxy, the radial velocities of several individual stars orbiting Sgr A* were measured using near-IR adaptive optics observations, confirming Sgr A* as a SMBH of $\sim 4 \times 10^6 M_\odot$ (Ghez et al. 2008; Genzel et al. 2010). For extragalactic sources, the line-of-sight velocities of bulk stellar motions in the galactic nucleus are measured using spatially resolved spectroscopy. Stellar dynamical models are constrained with this kinematic data to measure the mass of the SMBH (e.g., Gerhard 1993; Kormendy & Richstone 1995; Gebhardt et al. 2000a, 2011). The Schwarzschild (1979) orbit superposition method is the most widely used modelling technique (McConnell & Ma 2013; Saglia et al. 2016). As this method requires high spectral resolution to resolve the absorption lines, and high angular resolution to resolve the very centre of the galaxy, it is generally only used for nearby quiescent galaxies, but has also been done with weak AGN (Onken et al. 2014).

- Gas dynamics: The radial velocities of ionised gas disks are measured from spectra and modelled dynamically (Harms et al. 1994; den Brok et al. 2015). However, gas kinematics aren't necessarily dictated by the gravitational potential of the central SMBH alone (Cappellari et al. 2002), and this method also requires high spatial resolution. As with stellar dynamical masses, this method is largely dependent on the model and its assumptions, which can significantly affect the measured mass (Gebhardt & Thomas 2009).

- Megamasers: The rotation curve of the megamaser disk is measured from water emission at 22 GHz using very long baseline radio interferometry (VLBI) (Miyoshi et al. 1995; Greenhill et al. 2003; Kuo et al. 2011). This method can only be used in Type 2 AGN with water masers, which need to be viewed at an inclination angle within a few degrees of edge on, and is therefore inapplicable for large samples.

- Spectroastrometry: The GRAVITY instrument on the Very Large Telescope Interferometer (VLTI) has been used to spatially resolve the broad-line region in 3C 273 and IRAS 09149-6206, recovering the size and structure (Gravity Collaboration et al. 2018; GRAVITY Collaboration et al. 2020).

- VLBI: The Event Horizon Telescope spatially resolved the shadow of the SMBHs in M87 and the Milky Way (Sgr A*) using a global network of radio telescopes, achieving an angular resolution of $\sim 20\mu$as (Event Horizon Telescope Collaboration et al. 2019, 2022). The size of this ring was used to measure the SMBH mass.

However, each of these methods require exceptionally high spatial resolution to resolve the small angular size of the gravitational sphere-of-influence of the SMBH. Consequently, these methods have been restricted to SMBHs in the nearby Universe ($z < 0.2$), and the latter method to the very nearest galaxies. The RM technique can measure direct SMBH masses for Type 1 AGN by resolving the innermost regions in the time domain, thereby circumventing the need for high angular resolution. Some of the most luminous AGN (*i.e.*, quasars) have been observed at redshifts as high as $z \sim 7.6$ (Bañados et al. 2018; Wang et al. 2021); equivalent to a look-back time of ~12.8 Gyr. Therefore RM of AGN provides the unique opportunity to trace the evolution of supermassive black holes and galaxies over most of the history of the Universe.

1.3 Reverberation Mapping

The central SMBH in AGN are surrounded by hot accretion disks, which produce intrinsically stochastic variable continuum emission arising due to magneto-rotational instabilities (Balbus & Hawley 1991; Tang et al. 2023). This continuum emission ionises the broad-line region (BLR), which reprocesses this radiation, emitting a broad emission-line spectrum. Some of the strongest observed broad emission lines are the Balmer-series lines (e.g. H$\alpha\,\lambda6563$, H$\beta\,\lambda4861$), Mg II $\lambda2798$ and C IV $\lambda1549$. The variability of the ionising continuum emission drives correlated changes in the flux of the broad emission lines over time (Blandford & McKee 1982; Peterson 1993). The delay due to light travel-time between the continuum emission from the central source and the reprocessed emission from the BLR allows measurement of the radius of the BLR, $R_{\rm BLR}$.

To demonstrate how this reverberation response appears, we assume a simple model of the BLR as a thin ring of gas clouds with a radius R, as shown in Figure 1.2. The continuum emission from the accretion disk is emitted outward in all directions from the centre of this ring. At an angle θ from the line of sight, the emission reprocessed by the BLR has travelled a distance R to the BLR and is additionally delayed by the time taken for the light to travel to the observer. In this model, the time delay as a function of θ is

$$\tau(\theta) = (1 + \cos\theta)\frac{R}{c} \tag{1.1}$$

The mean time delay τ can therefore be measured as

$$\tau = \frac{R}{c}\int_0^{2\pi}(1 + \cos\theta)d\theta/2\pi = \frac{R}{c} \tag{1.2}$$

In reality, the reverberation response will depend on the geometry, orientation, and structure of the BLR. The mean time delay τ, also referred to as the reverberation

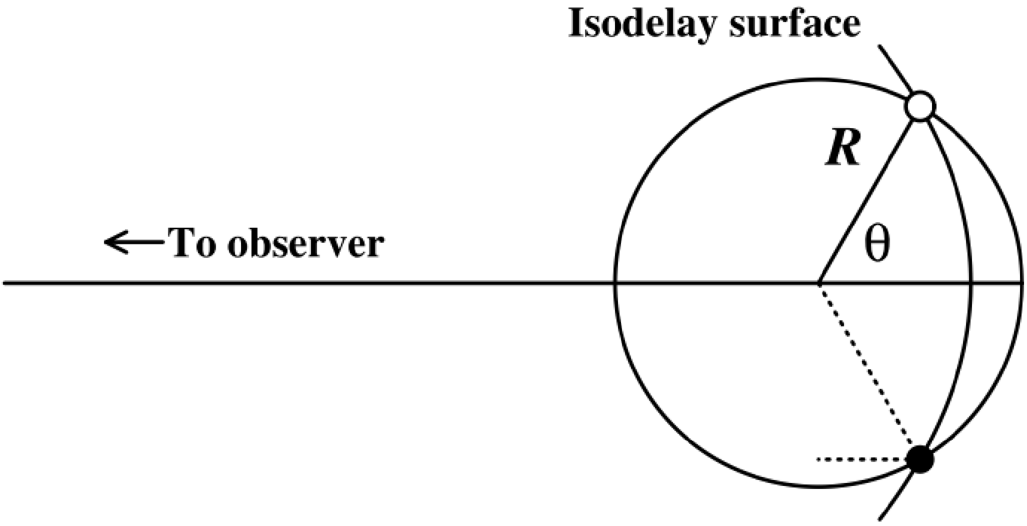

Figure 1.2: Figure 7 in Peterson (2001): A diagram showing the reverberation response of a thin ring of BLR clouds. The intersection points of the isodelay surface and the ring show the location of the BLR clouds that are observed to be responding simultaneously. The dotted line shows the light-travel time delay of the BLR emission reprocessed by one of these clouds that would be observed relative to the continuum emission.

lag, can be recovered by cross-correlating light curves tracing the changing continuum and emission-line flux, which provides a measurement of the responsivity-weighted radius of the BLR. It is assumed that the BLR is in virial equilibrium with the SMBH, and therefore bound in Keplerian orbits. The velocity dispersion of the BLR, ΔV, can be estimated from the width of the BLR emission lines, which are the ensemble average of the BLR cloud emission, with each cloud presenting a different Doppler shift. The mass of the central SMBH, $M_{\rm BH}$, can then be calculated from the measured $R_{\rm BLR}$ and ΔV using

$$M_{\rm BH} = f\frac{R_{\rm BLR}\Delta V^2}{G} \tag{1.3}$$

The geometry, orientation, and kinematics of the BLR are encapsulated by the dimensionless scale factor f, which is calibrated using sources with independent measurements from RM and the $M_{\rm BH} - \sigma_*$ relation (Ferrarese & Merritt 2000; Gebhardt et al. 2000a; Onken et al. 2004; Woo et al. 2015).

There are three key simplifying assumptions of the RM method, originally stated by Peterson (1993). Firstly, we assume that the central source of the continuum emission is significantly smaller than the BLR, i.e. that it is essentially a point source. Secondly, we assume reverberation lag is much longer than the recombination time for the BLR gas, and therefore the BLR cloud response time can be considered negligible. Thirdly, we assume the relationship between the observed continuum and reprocessed emission is approximately linear for small variations. With these assumptions, we can use

$$\Delta L(V,t) = \int_0^\infty \Psi(V,\tau)\Delta C(t-\tau)d\tau, \tag{1.4}$$

to describe the response of the emission-line flux, $\Delta L(V,t)$, at time t to the variable continuum flux, $\Delta C(t)$, that was emitted at a time τ earlier. The transfer function, $\Psi(V,\tau)$, describes the structure and kinematics of the BLR, which is a function of line-of-sight velocity, V (Blandford & McKee 1982). Velocity-resolved RM can be used to recover this transfer function, or 'velocity-delay map', for an AGN, thus providing bespoke information about the geometry, inclination and kinematics of the BLR (Peterson 2001).

Under the simple assumption all AGN have a similar ionising spectrum and BLR density, we can use the ionisation parameter, U, to predict the radius of the BLR using

$$U = \frac{L_{\rm ion}}{4\pi r^2 n_e c} \tag{1.5}$$

where $L_{\rm ion}$ is the luminosity of ionising photons, r is the distance to the ionised BLR, and n_e is the electron density (Davidson 1972). Therefore, photoionisation equilibrium predicts that the radius of the BLR should scale with AGN luminosity as $r \propto L^\alpha$ where $\alpha = 0.5$.

Although this describes the process for reverberation mapping of the BLR specifically, RM can also be done by measuring the time lag between: optical emission and X-ray observations to measure the radius of the innermost orbit of the accretion disk, multi-band optical/UV observations to measure the size of the accretion disk, or optical and infra-red observations to measure the dust sublimation radius (see Figure 1.3; Cackett et al. 2021).

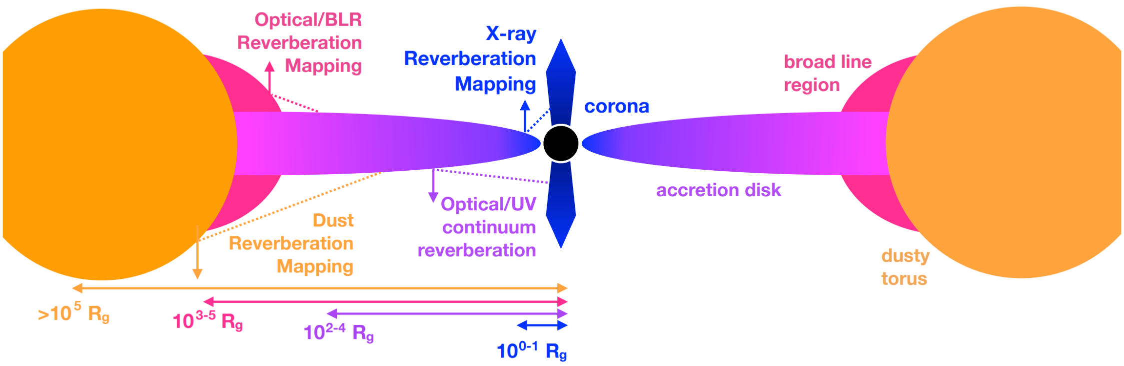

Figure 1.3: Figure 1 in Cackett et al. (2021): A cross-sectional schematic of an AGN highlighting the main components relevant to the four types of RM: X-ray, optical/UV continuum, BLR, and dust reverberation, labelled with general radial scales from the black hole, where R_G is the gravitational radius ($R_G = GM/c^2$).

1.3.1 Results from early surveys

Due to limits of technology at the time, the first RM campaigns (conducted during the 1980-90s) were generally conducted with relatively small (1-to-2m class) ground-based telescopes, and were only able to monitor a small sample of AGN on a source-by-source basis. As high S/N spectra are required to measure the variability of the emission-line fluxes, the majority of the sources monitored were bright, relatively nearby ($z < 0.1$) Seyfert galaxies. The duration of these surveys ranged from several months to years, with observations taken frequently (every few days to once a week) (Bentz & Katz 2015). These campaigns were able to successfully recover reverberation lags for dozens of AGN, however the sampling was generally insufficient to recover velocity-delay maps (Horne et al. 2004).

As many of the monitored sources were at low redshifts, most results were obtained using the Hβ emission line (4861 Å), as it appears within the rest-frame optical wavelength range. The results allowed the predicted relationship between the AGN luminosity and the radius of the BLR ($R - L$ relation) to be constrained, for the Hβ emission line. The initial results exhibited considerable scatter, and recovered a steeper than expect slope of $\alpha \sim 0.7$ (Kaspi et al. 2000; Bentz et al. 2006). Subsequent studies re-measured many lags with higher sampled data to obtain more accurate measurements, and subtracted the contribution of the host galaxy luminosity using high-resolution Hubble Space Telescope images (Bentz et al. 2009, 2013). The slope of the revised $R - L$ relation, shown in Figure 1.4, was found to be consistent with the theoretical prediction from photoionisation models of $\alpha \sim 0.5$, and exhibited rms scatter of only 0.13 dex.

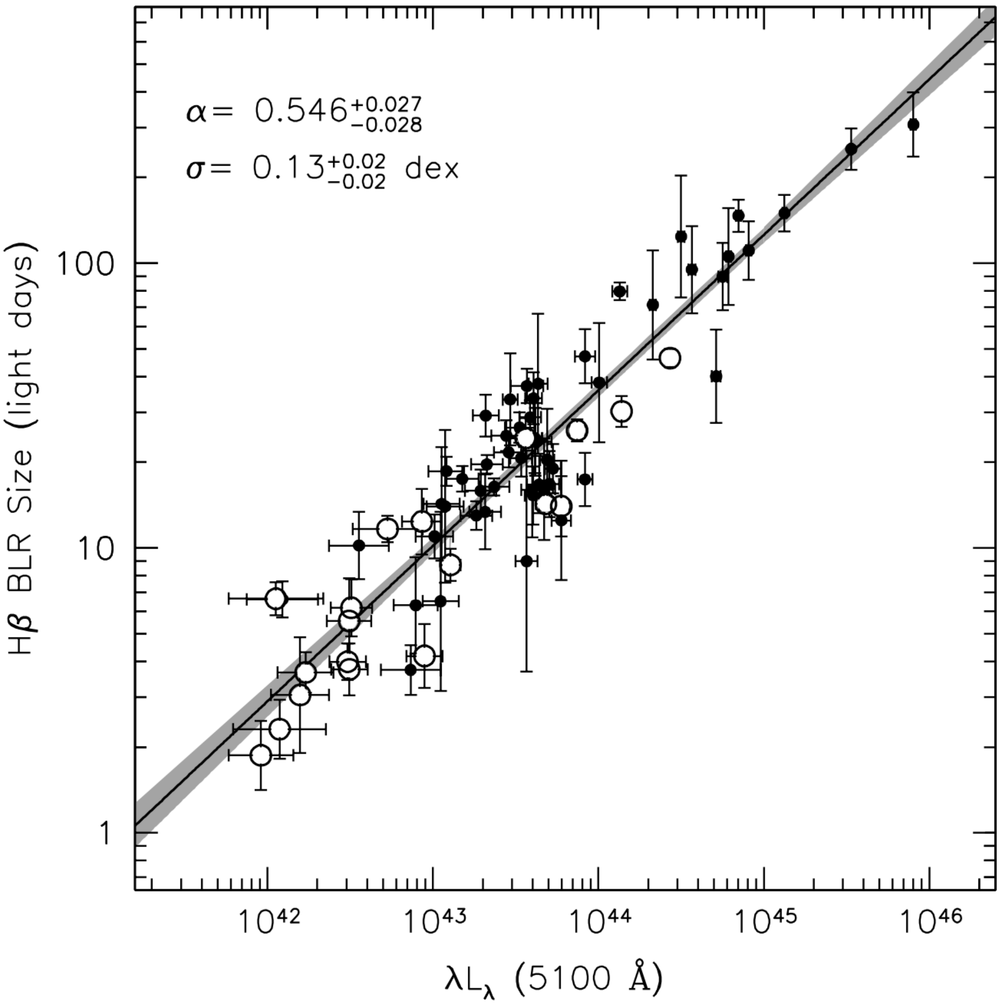

Figure 1.4: Figure 11 in Bentz et al. (2013): The best fit Hβ Radius-Luminosity relation (solid line) and range from the uncertainties on this fit (shaded region), constrained using the full collection of measurements available at the time from the literature (black points) and new measurements added by Bentz et al. (2013) (open-circle points).

Lags recovered using higher ionisation emission lines (e.g., C IV) were found to be shorter than lags recovered using lower ionisation emission lines (e.g., Hβ) (Gaskell & Sparke 1986; Dietrich et al. 1993). Therefore, higher ionisation emission lines were found to respond more rapidly to continuum variations, demonstrating the ionisation stratification of the BLR.

As of 2015, RM had been used to recover lags and measure black hole masses for 63

AGN via dedicated source-by-source monitoring (see results compiled by the AGN Black Hole Mass Database, Bentz & Katz 2015). Most measurements were made with Hβ, as Mg II and C IV are only visible within the rest-frame optical range at higher redshifts. As the reverberation lag is proportional to the AGN luminosity, and time dilation increases with redshift, making RM measurements at high redshifts requires many years of monitoring, particularly for the higher luminosity AGN. Only a handful of lags had been previously recovered using the C IV line, including one measurement for an AGN at $z = 2.2$ (Peterson et al. 2005; Kaspi et al. 2007), and only one lag with Mg II (Metzroth et al. 2006).

1.3.2 Applications of the Radius-Luminosity relation

Single-epoch black hole masses

With a well-calibrated $R - L$ relation, SMBH masses can be estimated using only a single AGN spectrum, bypassing the need to conduct observationally intensive RM for each AGN (Wandel et al. 1999). The emission-line width and continuum luminosity are measured from the spectrum, and the BLR radius is inferred from this luminosity using the $R-L$ relation, allowing the BH mass to be estimated using Equation 1.3. However, the only well calibrated $R - L$ relation exists for the Hβ line (Bentz et al. 2013). In order to measure SMBH masses at higher redshifts, this relation was extrapolated for the Mg II (McLure & Jarvis 2002; Onken & Kollmeier 2008; Woo et al. 2018) and C IV lines (Vestergaard 2002; Vestergaard & Peterson 2006), as too few RM measurements existed to establish the mass scaling relations for these lines independently. The Hβ mass scaling relation was re-calibrated for Mg II and C IV using UV spectra of the reverberation mapped sample with Hβ lags. This single-epoch method was used to estimate the SMBH masses of AGN up to $z \sim 4-5$, which were found have $M_{\rm BH} \sim 10^9 M_\odot$ at only 1.5 Gyr after the Big Bang (Vestergaard 2002). This finding has prompted much discussion about possible formation models for these early, massive BHs (Inayoshi et al. 2020).

These mass scaling relations allowed SMBH masses to be estimated for large spectroscopic samples comprising tens to hundreds of thousands of AGN, to study the evolution of SMBH growth (e.g., SDSS DR5, DR7, DR16, Shen et al. 2008, 2011;

Kelly & Shen 2013; Wu & Shen 2022). However, there are significant uncertainties on the order of ∼0.5 dex on these BH mass estimates, due to our limited understanding of BLR structure and kinematics, and the small number of available reverberation measurements, among other factors (Shen 2013). One of the largest contributions to this is the uncertainty in the calibration of the virial scale factor, f.

The virial factor, f, is empirically calibrated on the assumption that SMBH masses measured by RM should be consistent with those predicted by the $M - \sigma*$ relation observed for inactive galaxies (Ferrarese & Merritt 2000; Gebhardt et al. 2000a; Tremaine et al. 2002). It is measured as the shift required to align the $M-\sigma*$ relation for AGN with the fiducial $M - \sigma*$ relation for inactive galaxies, using measurements of the stellar velocity dispersion, $\sigma*$, for AGN with RM measurements (Gebhardt et al. 2000b; Onken et al. 2004; Woo et al. 2010; Park et al. 2012; Grier et al. 2013b). The latest widely accepted average scale factor, $\langle f \rangle$, is 4.47±1.25, based on a sample of ∼30 AGN (Woo et al. 2015).

Another source of uncertainty is that the Hβ $R-L$ relation has been calibrated using RM measurements made for mainly relatively nearby Seyfert galaxies, which only represent the low-redshift, low-luminosity subset of the general AGN population (Shen 2013). Therefore, the extrapolation of the mass scaling relations calibrated on this $R - L$ relation to the general AGN population is potentially unreliable.

AGN as 'standardisable' candles

A standard candle is an object with a known intrinsic luminosity, L, from which the distance to the source can be determined using the inverse square law

$$F(z) = \frac{L}{4\pi D(z)_L^2} \tag{1.6}$$

where $F(z)$ is the observed flux of the object, and $D(z)_L$ is the luminosity distance to the object. By measuring distances to these objects, and comparing it to their redshifts, we can probe the expansion history of the Universe.

Riess et al. (2011) showed that not only is the Universe expanding at an accelerating rate (Riess et al. 1998; Perlmutter et al. 1999), but that the Universe decelerated before it accelerated. Current models of dark energy are best discriminated by probing the point when the Universe shifted from decelerating to accelerating ($\sim 0.7 < z < 1.2$).

Type Ia supernovae (SNe Ia) are the most commonly used luminosity-distance indicator, however, due to their intrinsic luminosity, they are difficult to observe beyond $z \sim 1.5$ (Riess et al. 2004). While we can find SNe Ia at these relatively high redshifts, currently only ∼20 have been found at $z > 1$ (Scolnic et al. 2022). AGN have been proposed as an alternative standard candle, as they have several key advantages:

- AGN are observable at redshifts as high as $z \sim 7.6$ (Bañados et al. 2018; Wang et al. 2021).
- There are more of them. It is estimated that at least 1 in 10 galaxies have AGN. Not only are SNe Ia rare events, but they are even less likely to be produced in the early Universe due to the time scale of formation of the progenitor systems (Pritchet et al. 2008).
- AGN are not transient, as such, and are visible reliably for years. To detect short-lived SNe Ia, high cadence long-term monitoring over a wide field-of-view is required.

Therefore AGN have great potential for cosmology; they are abundant, would allow us to probe further into the Universe, and present the opportunity to measure distances across the majority of the Universe with a single probe, eliminating cross-probe systematics.

As all AGN do not have the same luminosity, they need to be standardised before using them to determine luminosity distances, much like SNe Ia. Given the dependence of the reverberation lag on the intrinsic absolute luminosity of the AGN, this can be used to measure the luminosity distance to the source. This method was used to create the first Hubble diagram using reverberation-mapped AGN, shown in Figure 1.5 (Watson et al. 2011; Martínez-Aldama et al. 2019). By using AGN as standard candles in cosmology, our understanding of the nature of dark energy and the evolution of the expansion of the Universe will no longer be limited to $z < 1$

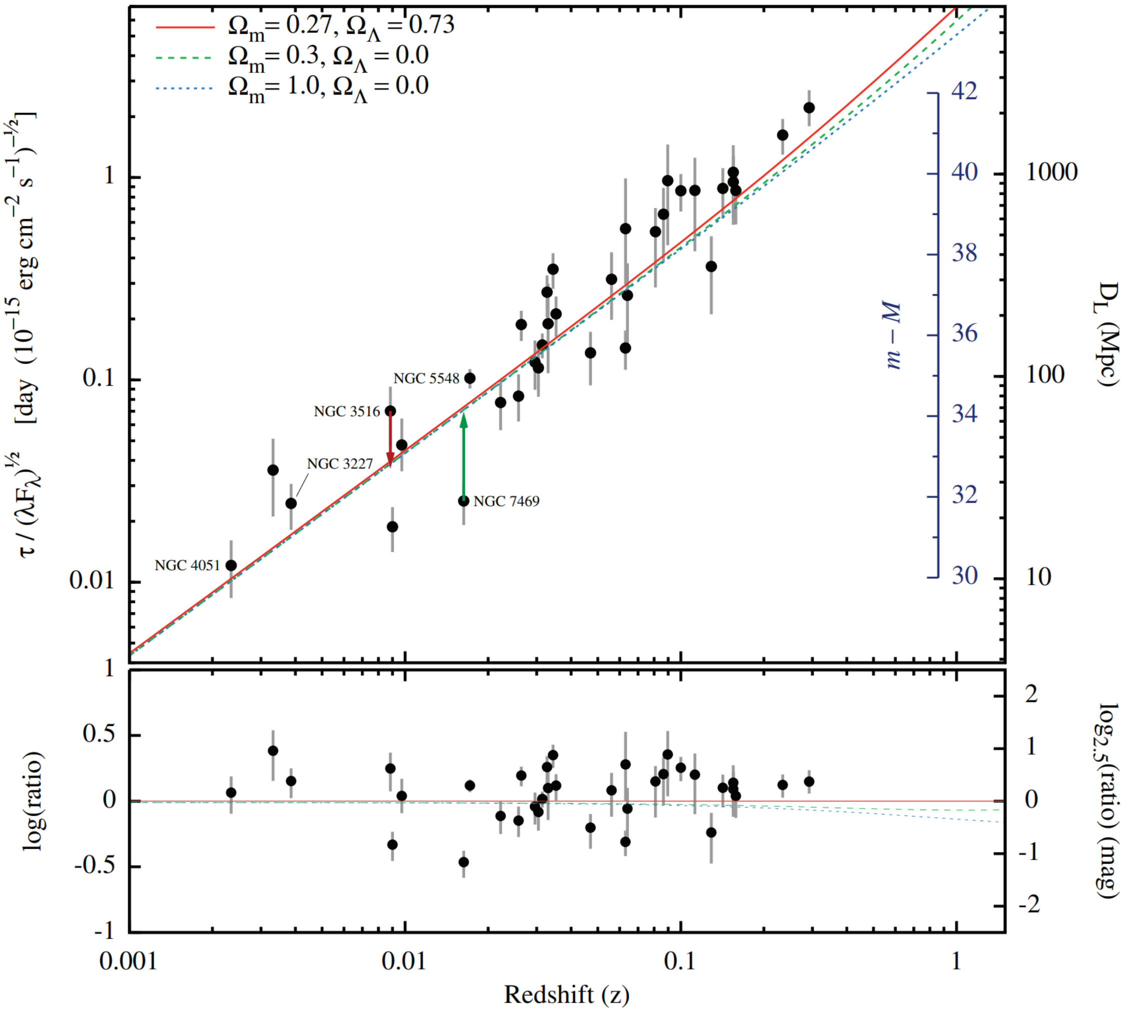

Figure 1.5: Figure 2 in Watson et al. (2011): The luminosity distance indicator $\tau/\sqrt{F}$ plotted as a function of redshift for 38 AGN with Hβ lag measurements.

(King et al. 2014).

The factors limiting the further application of this method are the intrinsic scatter in the Hβ $R - L$ relation, and the lack of RM measurements at $z > 0.3$ precluding the calibration of the $R - L$ relations for Mg II and C IV.

1.3.3 Recent RM campaigns

These important applications have been hindered by significant uncertainties arising from the limited range of source properties probed by the reverberation-mapped sample, and poor understanding of the true structure and kinematics of the BLR in AGN (Shen 2013).

To address the latter limitation, a number of surveys have conducted observationally intensive velocity-resolved RM, which can be used to measure the individual virial scale factor f for each AGN (e.g., Bentz et al. 2010; Grier et al. 2013a, 2017; Du et al. 2018; U et al. 2022), or measure the BH mass directly without f using dynamical modelling (e.g., CARAMEL, Brewer et al. 2011; Pancoast et al. 2011, 2014a). One example is the AGN Space Telescope and Optical Reverberation Mapping (AGN STORM) program, which used space- and ground-based telescopes to monitor NGC 5548 with daily cadence to recover high-fidelity velocity-delay maps (De Rosa et al. 2015; Horne et al. 2021). AGN STORM also observed a strange period where the BLR response was decoupled from the continuum variability for a few days; challenging the fundamental assumptions of the RM method (Goad et al. 2016; Dehghanian et al. 2019b). The BLR structure and size has also been resolved spatially using spectroastrometry (Gravity Collaboration et al. 2018). However, despite these efforts, a single average scale factor is still required to estimate BH masses for large samples, and its uncertainty is limited by the scatter in the $M - \sigma*$ relation.

Although the constraints on the $R - L$ relation for Hβ from Bentz et al. (2013) seemed promising, RM measurements made more recently by programs targeting a more diverse range of sources have seen an increase in the intrinsic scatter in this relation. The super-Eddington accreting massive black holes (SEAMBH) program conducted RM for over 40 high-luminosity AGN with high accretion rates (Du et al. 2014; Wang et al. 2014a; Du et al. 2015, 2016, 2018; Hu et al. 2021). Many of the lags recovered by this program were observed to lie below the Bentz et al. (2013) relation. The mechanism proposed to explain these shorter lags is self-shadowing effects of slim accretion disks resulting in anisotropic ionising radiation (Wang et al. 2014b). Although this program studied AGN with a more diverse range of properties, it only targeted AGN at $z < 0.4$.

As mentioned earlier, very few measurements have been made at high redshifts with the Mg II or C IV line from traditional source-by-source RM monitoring. To address this, over the past decade, two RM surveys utilised multi-object spectroscopy (MOS) to efficiently monitor large samples of AGN over a wide range of redshift and luminosities: the Australian Dark Energy Survey (OzDES) RM Program (2013–2019; King et al. 2015) and the Sloan Digital Sky Survey RM Project (SDSS-RM, 2014–2020; Shen et al. 2015). Below I describe the OzDES RM Program, which is the focus of this thesis, before discussing the recent results from these MOS-RM surveys.

1.4 Australian Dark Energy Survey (OzDES)

The Dark Energy Survey (DES) conducted a wide-field survey covering 5000 deg^2 of the sky in the g, r, i, z filters, with the Dark Energy Camera (DECam) on the 4m Blanco telescope at Cerro Tololo Inter-American Observatory (CTIO) in Chile (Flaugher et al. 2015; Dark Energy Survey Collaboration et al. 2016). Additionally, DES observed 10 legacy deep fields covering a total of 27 deg^2, with $\sim$6 day cadence from 2013 to 2018 (with additional science verification data taken in 2012), to detect SNe Ia and other transients as part of the Supernova Program (Diehl et al. 2018). These 10 deep fields comprise the ELAIS, XMM-LSS, Chandra deep-field South, and SDSS Stripe 82 fields (Kessler et al. 2015). To best accommodate the visibility of each of the deep fields, they were observed over a 5-6 month season ($\sim$ August to January).

The Australian Dark Energy Survey (OzDES) performed the spectroscopic follow-up of the 10 deep fields, with the 2dF multi-object fibre positioning system (Lewis et al. 2002) and the AAOmega spectrograph (3700–8800 Å, Sharp et al. 2006) on the 3.9m Anglo-Australian Telescope (AAT) at Siding Spring Observatory (Yuan et al. 2015; Childress et al. 2017; Lidman et al. 2020). The AAT and Blanco telescope have the same 2 deg^2 field of view (FOV), as shown in Fig. 1.6, making the AAT ideal to follow up the DES deep fields. OzDES observed over the same 5-6 month season with approximately monthly cadence, over 6 years, from 2013 to 2019. After the conclusion of the Supernova Program, additional DECam observations were taken monthly in the 2018–19 season to continue concurrency with OzDES, resulting in a total photometric monitoring baseline of 7 years for the deep fields.

The primary scientific goals of OzDES were to follow up SNe discovered by DES

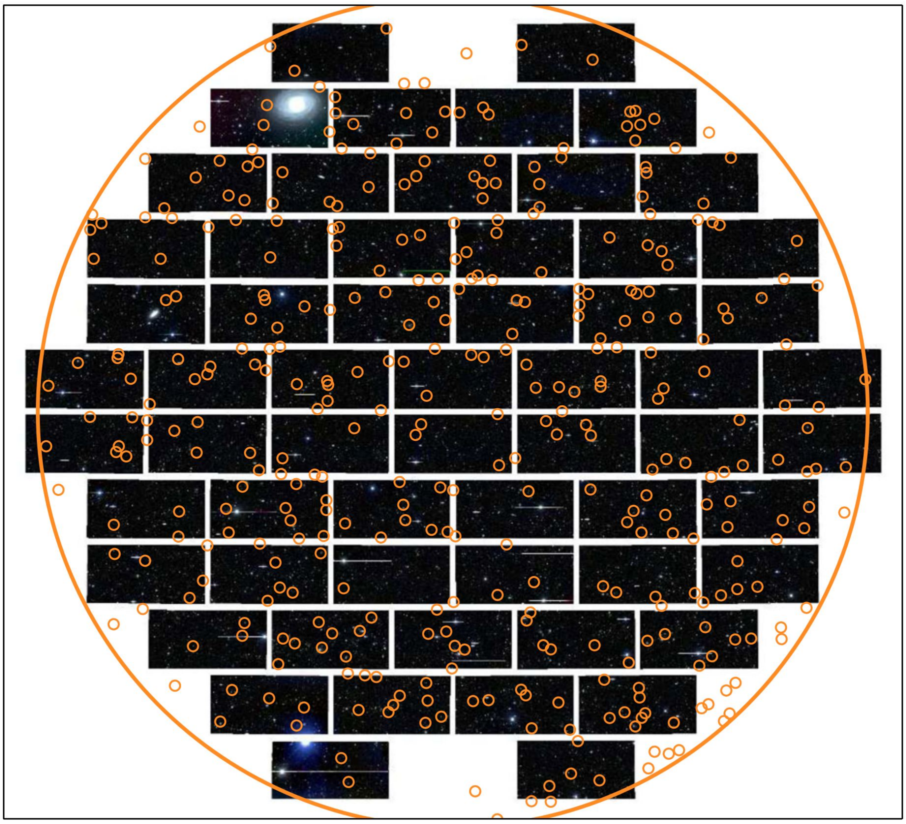

Figure 1.6: Figure 1 from Yuan et al. (2015): The background image shows the DECam CCDs in their mosaic formation across its 2-degree FOV. Overlaid is the 2dF spectrograph FOV (large orange circle) with its 392 optical fibres (small circles), configured for one of the OzDES fields. Almost one quarter of these fibres were dedicated to observing AGN for the RM program, for each of the 10 field configurations.

in order to measure host galaxy redshifts and for spectroscopic classification, as well as recovering lags for AGN using RM. As stated in the name of the survey, SNe Ia are being used to measure the dark energy equation of state parameter, from the consistently calibrated sample of SNe Ia detected by DES alone (aside from the anchoring low-z sample) in order to minimise systematic uncertainties (Abbott et al. 2019). In addition to measuring SMBH masses from RM, OzDES will also investigate the aforementioned potential of AGN to be used as an alternative 'standardisable' candle to determine cosmological luminosity distances.

1.4.1 OzDES Reverberation Mapping Program

As part of the OzDES RM Program, 735 AGN were monitored, at redshifts $0.1 < z < 4.0$ with apparent magnitudes $17.2 < r_{\rm AB} < 22.3$. The distributions of the

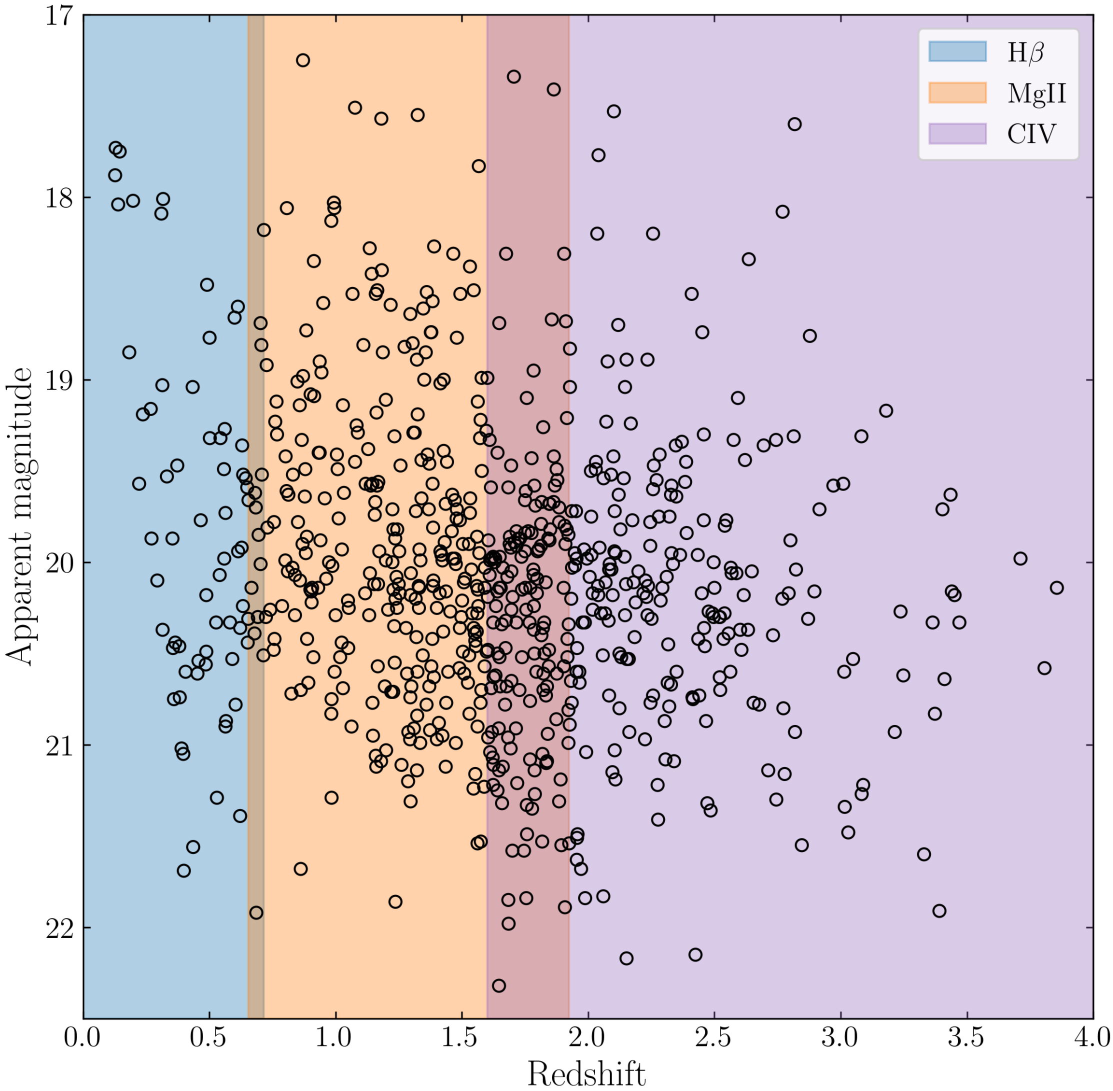

Figure 1.7: Distribution of redshifts and apparent magnitudes for the 735 AGN monitored by OzDES for RM. The shaded regions indicate the redshift range over which the particular emission-line is visible. The ranges are: $0 < z < 0.72$ for Hβ , $0.65 < z < 1.92$ for Mg II, and $z > 1.60$ for C IV.

redshifts and magnitudes of these targets are shown in Figure 1.7. This sample was selected from the wider sample of quasars detected by DES (King et al. 2015). The DES quasar selection is detailed by Tie et al. (2017), and briefly described here. First, all point sources in the DES fields were identified, and cuts based on colour were used to select the quasars, from DES Year 1, VISTA Hemisphere Survey (K band; McMahon et al. 2013), and Wide-Field Infrared Survey (WISE; Wright et al. 2010) photometry covering the near-infrared to optical wavelength range. Probabilistic modelling and variability selection were used to further refine the sample, which has completeness $> 85\%$, measured by comparing the region of

DES overlapping with the highly complete SDSS Stripe 82 quasar sample (Peters et al. 2015). The resulting sample of 1263 spectroscopically confirmed quasars was reduced to our final sample of 735 AGN after screening for sources that fell within DECam chip gaps, had low flux signal-to-noise, or with emission lines compromised by the transition between the red and blue arms of AAOmega (King et al. 2015; Hoormann et al. 2019).

The time-series photometry of the 10 DES deep fields yielded high quality continuum light curves for our AGN sample, covering a 7-year baseline, in the g, r and i-bands. The time-series emission line measurements were made using the spectra obtained by OzDES. Since the sources are at various redshifts, their spectra are redshifted accordingly, and only certain emission-lines are visible in the $3700-8800$ Å wavelength range of AAOmega. Therefore different emission-lines have to be used for different sources. To measure the flux from the emission lines, the nearby continuum level also needs to be measured. The following ranges were defined considering the visibility of the emission-line and nearby continuum for our sample. The Hβ emission-line is visible for sources at $z < 0.72$, Mg II at $0.65 < z < 1.92$ and C IV at $z > 1.60$. In the overlapping ranges both emission lines are able to be used independently to recover the lags.

Spectroscopy requires significantly more time investment than photometry: at least 2×2400s exposures were required for each field to achieve sufficient spectral signal-to noise for all sources (Childress et al. 2017), as opposed to a total exposure time of ∼1000s per field for the photometry (Kessler et al. 2015). OzDES was awarded 100 nights in total on the AAT, however, since ∼ 4 nights were required to obtain a single epoch of data for each of the 10 fields, and ∼ 30% of time was lost due to poor weather or suboptimal conditions, ∼ 4 spectroscopic epochs have been obtained for each field per year, with roughly monthly cadence, resulting in 18-25 total epochs, depending on the field (Lidman et al. 2020).

1.4.2 Results from MOS-RM

OzDES and SDSS-RM conducted similar AGN sample selection, but their observational strategies had one key difference: cadence. SDSS-RM observed 849 AGN at $0.1 < z < 4.5$, flux limited to $i_{\mathrm{AB}} < 21.7$ (Shen et al. 2019a), over a 6 month season (January to July) from 2014 to 2020. As SDSS-RM targeted a single 7 deg^2 field, they were able to observe with higher cadence: ~ 4 days in 2014 (yielding 32 epochs), bimonthly from 2015–17 (12 epochs per year) and monthly from 2018–20 (6 epochs per year) (Shen et al. 2019b). This was done so their lag recovery would be more sensitive to shorter lags. Here I briefly summarise the available lag results from these MOS-RM surveys.

As for the SEAMBH program, the Hβ lags recovered by SDSS-RM were found to lie below the Bentz et al. (2013) relation, as shown in Figure 1.8, significantly increasing the intrinsic scatter in the relation. However, their AGN did not have high accretion rates, so it was unclear why this was occurring. Simulations by Fonseca Alvarez et al. (2020) found that the observed deviation is unlikely to be a consequence of observation bias (as only one 6-month season of data was available at the time), and rather ascribed it to a change in the shape of the ionising spectral energy distribution (SED).

The next MOS-RM results were two C IV lags recovered by OzDES, using the first four years of data available at the time (Hoormann et al. 2019), which were consistent with the small sample of existing results. Following this, SDSS-RM recovered dozens of new lags with Mg II and C IV, using the first 4 years of their data. However, there is significant intrinsic scatter in the results (Grier et al. 2019; Homayouni et al. 2020). This has cast doubt on the reliability of lags recovered with MOS-RM. Partially in attempt to address this, simulations conducted by Li et al. (2019) and Penton et al. (2022) compared the performance of the two widely used lag recovery methods, and investigated the selection criteria of high-quality lags. The recent Mg II lag results using the complete OzDES data show reduced intrinsic scatter through the use of more strict selection criteria (Yu et al. 2021, 2023). The OzDES C IV results using the complete survey data are currently in preparation, with 25 preliminary lags recovered for AGN up to $z = 2.8$.

Aside from results for BLR RM, the DES photometry was also used to recover accretion disk lags (Mudd et al. 2018; Yu et al. 2020b).

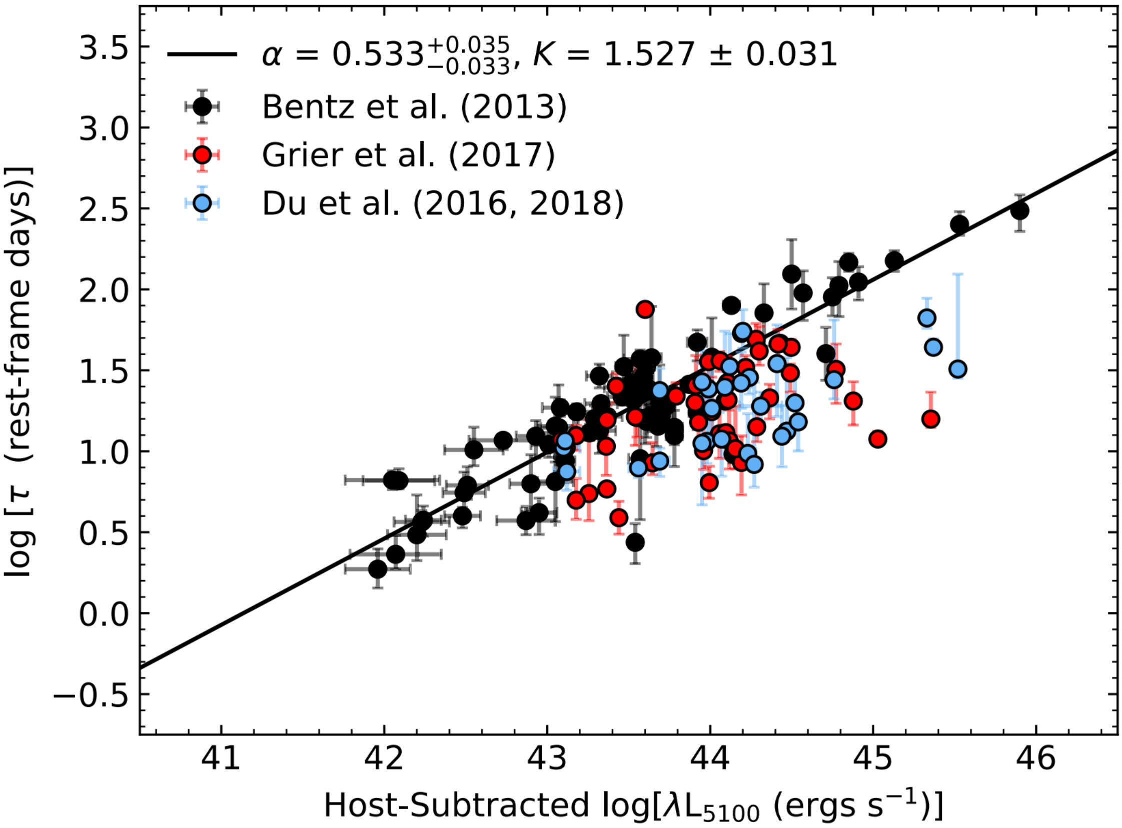

Figure 1.8: Figure 1 in Fonseca Alvarez et al. (2020): The Hβ $R-L$ relation, with lag measurements from Bentz et al. (2013) (also shown in Figure 1.4), and more recent measurements made by Grier et al. (2017); Du et al. (2016, 2018). The black line shows the best fit $R-L$ relation from Bentz et al. (2013). Many of the lags from SDSS-RM (red points) and SEAMBH (blue points) lie below this relation.

1.5 Thesis Outline

In this thesis, I explore the next generation of reverberation mapping, with multi-object surveys. The limited number of measurements made at $z > 0.4$ encouraged MOS-RM surveys to observe hundreds of AGN, to broaden the reverberation-mapped sample, and constrain $R-L$ relations for Mg II and C IV. However, these programs have highlighted the challenges involved with scaling RM up to this 'industrial-scale' format. I note that aside from the SDSS-RM Hβ results, no other MOS-RM results had been published when I started my candidature. The state of the field has advanced dramatically as the MOS-RM results have been published over the past 4 years. As such, the work presented in this thesis was conducted dynamically, as findings were being presented. Here I briefly introduce each of the chapters of this thesis.

Chapter 2: Observational window effects on multi-object reverberation mapping

In Chapter 2, I investigate how the design of MOS-RM surveys impacts their efficacy. During preliminary lag recovery for the OzDES RM Program, it became clear that we would be limited by the low sampling of our survey. Using bespoke simulations, I examine how lag recovery efficacy changes when the cadence, season length and baseline of the survey is varied. After identifying the the key factors limiting lag recovery efficacy, I simulate a grid of AGN over the accessible range of redshift and luminosity to demonstrate various scenarios for upcoming MOS-RM surveys.

Chapter 3: OzDES Reverberation Mapping Program: Hβ lags from the 6-year survey

In Chapter 3, I present new reverberation lags measured from the OzDES RM Program Hβ sample. OzDES notably had lower spectroscopic sampling than earlier traditional RM surveys, making the recovery of the shorter lags expected for the Hβ sample particularly challenging. I measure SMBH masses for the successful lag recoveries, and compare the consistency of our results with earlier measurements on the $R-L$ relation. In conjunction with the findings from the previous chapter, these results show promise for future RM programs to make further measurements which can reduce the intrinsic scatter in this important $R-L$ relation.

Chapter 4: OzDES Reverberation Mapping Program: Stacking analysis with Hβ, Mg II and C IV

In Chapter 4, I apply the stacking technique developed by Fine et al. (2012, 2013) to recover average reverberation lags across the redshift-luminosity parameter space probed by the OzDES RM sample. This method is able to overcome some, but not all, of the issues imposed by the less-than-ideal window function that has limited the overall individual lag recovery efficacy of OzDES to $\sim 10\%$. I compare our average stacked lags with the complete sample of individual RM measurements available for each emission line, and examine the promising potential of this technique which, until now, has had limited use.

Chapter 5: Conclusion

Finally, in Chapter 5, I summarise the results of this thesis and briefly discuss avenues for future research.

2

Observational window effects on multi-object reverberation mapping

This chapter is published in the Monthly Notices of the Royal Astronomical Society as: **Malik, U.**; Sharp, R.; Martini, P.; Davis, T. M.; Tucker, B. E.; Yu, Z.; Penton, A.; Lewis, G. F.; Calcino, J., *Observational window effects on multi-object reverberation mapping*, 2022, MNRAS, 516, 3238-3253.

Part of Section 2.2.2 in this chapter is published in the Monthly Notices of the Royal Astronomical Society (in Section 2 and A1) as: Penton, A.; **Malik, U.**; Davis, T. M.; Martini, P.; Yu, Z.; Sharp, R.; Lidman, C.; Tucker, B. E.; Hoormann, J. K. et al. (61 additional authors not shown), *OzDES Reverberation Mapping Program: Lag recovery reliability for 6-yr C*IV *analysis*, 2022, MNRAS, 509, 4008.

Abstract

Contemporary reverberation mapping campaigns are employing wide-area photometric data and high-multiplex spectroscopy to efficiently monitor hundreds of active galactic nuclei (AGN). However, the interaction of the window function(s) imposed by the observation cadence with the reverberation lag and AGN variability time scales (intrinsic to each source over a range of luminosities) impact our ability to recover these fundamental physical properties. Time dilation effects due to the sample source redshift distribution introduces added complexity. We present comprehensive analysis of the implications of observational cadence, seasonal gaps and campaign baseline duration (*i.e.,* the survey window function) for reverberation lag recovery. We find the presence of a significant seasonal gap dominates the efficacy of any given campaign strategy for lag recovery across the parameter space, particularly for those sources with observed-frame lags above 100 days. Using OzDES as a baseline, we consider the implications of this analysis for the 4MOST/TiDES campaign providing concurrent follow-up of the LSST deep-drilling fields, as well as upcoming programs. We conclude that the success of such surveys will be critically limited by the seasonal visibility of some potential field choices, but show significant improvement from extending the baseline. Optimising the sample selection to fit the window function will improve survey efficacy.

2.1 Introduction

The innermost regions of active galactic nuclei (AGN) provide a crucial window for the understanding of supermassive black hole (SMBH) physics and galaxy evolution. Within the local Universe, this zone can be resolved to within the gravitational sphere of influence through the use of the highest angular resolution instruments (e.g., Gebhardt et al. 2000a; Greene et al. 2010; Gebhardt et al. 2011; Kuo et al. 2011; Event Horizon Telescope Collaboration et al. 2019). Beyond the local Universe the achievable angular resolution becomes inadequate to resolve the environments of even the most massive black hole systems. We must turn to indirect techniques to probe the structure of such systems.

Reverberation Mapping (RM) provides a powerful opportunity to probe the structure of even the most distant of these compact systems. By resolving the innermost regions of AGN in the time-domain, the variable continuum emission from an accretion disk triggers a *reverberation* response in the surrounding environment and this signal can be inverted to reveal otherwise unresolvable physical detail. The broad line region (BLR) produces an emission-line spectrum in which the flux of the emission lines reverberates in response to the variability of the ionising continuum emission (Blandford & McKee 1982; Peterson & Horne 2004). The delay τ, due to light travel time between the continuum emission from the compact core and the emission from the BLR, allows the radius of the BLR ($R_{\mathrm{BLR}} \sim c\tau$) to be inferred. The velocity dispersion of the BLR (ΔV) can be estimated from the width of the broadened emission lines. The mass of the central black hole (M_{BH}) can then be measured using the virial theorem:

$$M_{\mathrm{BH}} = f\frac{R_{\mathrm{BLR}}\Delta V^2}{G}, \tag{2.1}$$

where f is the virial coefficient; a dimensionless scale factor that accounts for the geometry, orientation, and kinematics of the BLR (Woo et al. 2015).

This technique has been used to measure the masses of over 100 SMBHs, establishing RM as the primary method of SMBH mass measurement at $z > 0.1$ at present. The tight correlation found between the AGN luminosity and the radius of the BLR ($R-L$ relation; e.g., Bentz et al. 2009) has facilitated the use of indirect virial BH mass estimators using single-epoch spectroscopy (e.g., Shen et al. 2011). Watson et al. (2011) proposed using the $R-L$ relation to standardise AGN for use in cosmology. Although RM is a powerful technique with many applications, its full potential is yet to be reached. Few measurements have been made for the Mg II and C IV emission lines, preventing the $R-L$ relations for these lines from being better constrained. This has also meant that the subset of AGN for which most RM measurements have been made are limited to local AGN, which are not representative of the general AGN population (Shen et al. 2008; Shen 2013). It is necessary to probe the full range of AGN luminosities to improve virial BH mass estimates for the broader population.

Time-domain photometric and spectroscopic monitoring is required to successfully conduct RM of the BLR, since the technique relies on tracing the stochastic variability of AGN. To mitigate the bias towards local AGN, recent 'industrial-scale' RM campaigns have probed new regions of the AGN luminosity-redshift parameter space, with a particular focus at high-redshifts. This includes the Australian Dark Energy Survey (OzDES) RM Program (King et al. 2015) and Sloan Digital Sky Survey RM Project (SDSS-RM, Shen et al. 2015), which began in 2013 and 2014, respectively. Developments with multi-object spectroscopy have enabled these surveys to monitor large AGN samples. The success of lag recovery is highly dependent on the observational window, therefore the cadence, season length and baseline must be optimised to achieve the goals of the survey.

The observational window function (both photometric and spectroscopic) of any observing campaign imposes structure on the light curve sampling for a RM survey. Long baseline time-series photometry is readily obtainable through contemporary wide-field surveys (e.g., Dark Energy Survey, LSST). Obtaining concurrent spectroscopy is more challenging, due to the large multiplex of a wide field-of-view required. Facility choice is furthered restricted by the need for a large telescope aperture, essential to achieve sufficient signal-to-noise in the spectroscopic data for practical integration times. Improved facility access, and broad appeal across a range of survey applications, drives many surveys to equatorial fields to facilitate access to the survey program from both hemispheres. Observing equatorial fields immediately restricts field visibility and imposes a significant seasonal gap on the data.

The RM technique relies on recovering the lag between observed continuum and emission-line light curves using cross-correlation, which is highly dependent on how the light curves are sampled. The effect of the observational window on lag recovery has been studied in a limited capacity. White & Peterson (1994) investigated the minimum required sampling interval (*i.e.,* cadence) for accurate recovery, and Welsh (1999) identified improvement with extending the duration of light curves. However both these studies were limited to studying the recovery for local AGN with lags less than a month long, on an individual source basis. For contemporary large-scale surveys, King et al. (2015) and Shen et al. (2015) conducted simulations of the OzDES and SDSS-RM surveys, respectively. The simulations tested some program alterations and extensions, which highlighted improvements with extending the season length and baseline, but this was not used to alter the implemented survey design. Recent RM results from these programs (Grier et al. 2017; Hoormann et al. 2019; Grier et al. 2019; Homayouni et al. 2020; Yu et al. 2021; Penton et al. 2022) show how the observational window presents challenges for recovery of these high-z AGN lags, such as aliasing due to seasonal gaps. In addition, lag recovery depends on the signal-to-noise of the flux measurements and observed variability of the AGN. After combining these factors we see how complex lag recovery can be, and the need for a comprehensive study of how it can be improved.

There are factors in the success of RM which can be controlled, and those that can not. It is possible that the observed variability of a source is simply unfavourable (e.g., monotonic behaviour, Kaspi et al. 2007), or that some sources do not reverberate ideally (e.g., BLR 'holiday', Goad et al. 2016; Dehghanian et al. 2019a). As more RM surveys are completed, a better understanding of such phenomena can be achieved. The signal-to-noise of spectroscopic measurements, particularly at high redshifts, also presents a challenge. Presently RM surveys must focus on the factors that can be controlled: the survey window. In this work, we present a detailed investigation of each component of the global window function which describes the survey sampling. In Section 2.2 we describe the AGN light curve model, window functions, and lag recovery methods. Section 2.3 presents simulations designed to probe the 3-dimensional parameter space of cadence, season length and baseline to see how the accuracy and precision of the lag recovery changes. We then extend this to a subsample of simulated AGN with a range of expected lags before conducting high-resolution simulations for a grid of AGN probing a wide region of redshift-luminosity parameter space. We simulate the efficacy of a future planned 'industrial-scale' RM survey and potential extensions that could improve its success. We discuss the implications and caveats of our work in Section 2.4 and summarise our key results in Section 2.5.

2.2 Modelling observational window functions

The DES deep survey targeted legacy supernovae fields across a wide range in declination, with all regions followed up with multi-object spectroscopy conducted by OzDES. We model the resulting observational window function for RM using this contemporary survey as an initial baseline. The OzDES window function is largely representative of the window functions of current and planned large-scale RM surveys (e.g., Shen et al. 2015; Kollmeier et al. 2017; Brandt et al. 2018; Swann et al. 2019; The MSE Science Team et al. 2019). The custom window functions we apply probe the window function parameter space by modelling surveys that could be performed by contemporary facilities. To conduct our simulations, we created mock AGN light curves to which we could apply our custom window functions. In this section we introduce the OzDES survey, used as our base model survey, and describe how we create mock light curves. We then explain the custom window functions, and the lag recovery methods used for this work.

2.2.1 OzDES Reverberation Mapping Program

As part of the broader Dark Energy Survey (DES), the DES supernovae (SNe) program repeatedly observed 10 deep fields, covering 27 deg^2 of the sky, in the g, r, i and z filters, with the Dark Energy Camera (DECam) on the 4m Blanco telescope at Cerro Tololo Inter-American Observatory (CTIO) (Dark Energy Survey Collaboration et al. 2016). These fields comprise of the ELIAS, XMM-Large Scale Structure, Chandra deep-field South, and SDSS Stripe 82 fields. The deep fields were observed over a 5-6 month campaign season (from September to January) each year, from September 2013 to January 2019. The photometric observations were obtained, on average, every 6 days during each season. This cadence, designed principally for detection of transient events such as type-Ia SNe, provides continuum light curves for AGN reverberation mapping. Wide-field multi-object spectroscopy for the SNe program was provided by the OzDES program. OzDES performed the spectroscopic follow-up of the deep fields with the 2dF multi-object fibre positioning system and the AAOmega spectrograph (Sharp et al. 2006) on the 3.9m Anglo-Australian Telescope (AAT), with a monthly cadence over the same 6-year baseline

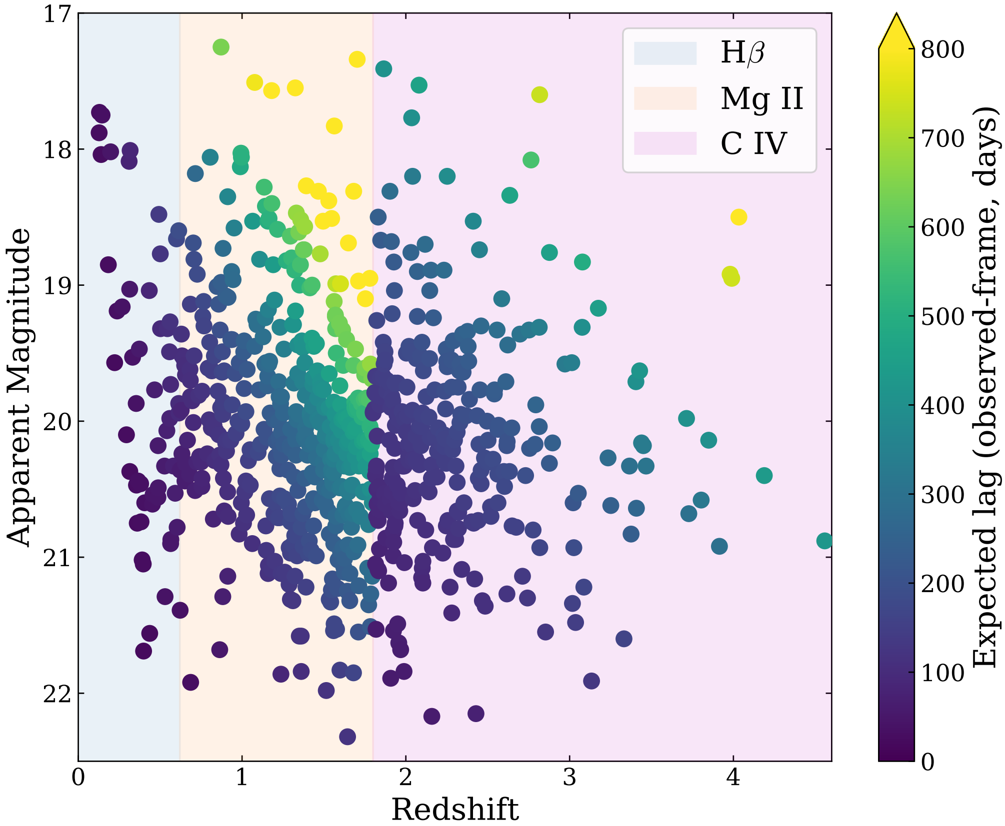

Figure 2.1: Distribution of redshifts and r band apparent AB magnitudes for the 771 AGN monitored by OzDES for RM, and their expected observed-frame lags from published $R - L$ relations. The relations from Bentz et al. (2013), Trakhtenbrot & Netzer (2012) and Hoormann et al. (2019) were used for the Hβ (0< z <0.62), Mg II (0.62< z <1.78) and C IV (z >1.78) emission lines, respectively.

(Yuan et al. 2015; Childress et al. 2017; Lidman et al. 2020). The primary scientific goals of OzDES were to follow-up supernovae discovered by DES, by using their spectra to determine host-galaxy redshifts and for classification, and to conduct RM of AGN.

As part of the OzDES RM program, 771 AGN have been monitored, at redshifts $0.12 < z < 4.5$ with apparent magnitudes $17.2 < r_{\rm AB} < 22.3$. The distributions of the redshifts and magnitudes of these targets are shown in Figure 2.1, which also shows the expected observed-frame lags for our sample. The sample was screened for sources that fell within DECam chip gaps, or with emission lines compromised by the transition between the red and blue arms of AAOmega (see King et al. 2015; Tie et al. 2017, for more details). The SDSS-RM sample follows a similar distribution (Shen et al. 2015).

We continued photometric observations with DECam in 2019, and spectroscopic observations with the AAT in 2020. Due to COVID-19 disruptions closing the observatory in 2020, we continued the photometric observations with DECam in 2021. This will partially bridge the gap to the Legacy Survey of Space and Time (LSST) conducted with the Vera Rubin Observatory, which will also be observing the ELIAS, XMM-LSS and Chandra DFS, as three of its four deep-drilling fields. This will also provide continuity to the spectroscopic follow-up of the LSST deep-drilling fields by SDSS-V (Kollmeier et al. 2017) and the Time-Domain Extragalactic Survey (TiDES; Swann et al. 2019), which we discuss in §2.3.3.

2.2.2 Light curves

The damped random walk (DRW) model developed by Kelly et al. (2009) was used to create simulated continuum light curves. It has been shown to provide an adequate representation of the intrinsically stochastic behaviour exhibited by AGN, as seen in their continuum light curves. A DRW is a random walk with an additional term that pushes deviations back to the mean value. It is characterised by two parameters, the damping timescale and the amplitude, which are unique to the source. Kozłowski et al. (2010) and MacLeod et al. (2010) extended this work and compared this model to more observed AGN light curves, applying the DRW model to directly constrain the variability parameters. MacLeod et al. (2010) determined the correlations between the variability parameters and physical AGN properties, including luminosity and black hole mass, using photometric light curves for ∼8,000 spectroscopically confirmed quasars in the Stripe 82 field, which were monitored over a 10 year baseline by the Sloan Digital Sky Survey (SDSS). The DRW model has been widely used for RM simulations (Shen et al. 2015; King et al. 2015; Li et al. 2019; Penton et al. 2022). Although AGN variability has been observed to deviate from the DRW on short time-scales (Mushotzky et al. 2011; Kasliwal et al. 2015; Smith et al. 2018), this has been found to not affect lag measurements (Yu et al. 2020b).

The procedure we used to generate the simulated light curves is detailed below (reproduced from Section 2.1 and A1 in Penton et al. 2022). The required inputs are the source redshift and apparent magnitude, from which each of the model parameters are derived. For each simulated source, the expected rest-frame lag was estimated using the $R - L$ relations for the Hβ (0< z <0.62) (Bentz et al. 2013), Mg II (0.62< z <1.78) (Trakhtenbrot & Netzer 2012) and C IV (z >1.78) (Hoormann et al. 2019) emission lines, and multiplied by $(1 + z)$ to obtain the input observed-frame lag, τ_{input}. Unless otherwise stated, the light curves, input lags and timescales we refer to are in the observed frame.

The simulated AGN light curves were generated with daily cadence of the photometric and spectroscopic light curves, then appropriately down-sampled by the window function. The photometric and spectroscopic fluxes have 3% and 10% observational uncertainties applied, respectively, approximately representative of the DES and OzDES survey data (Dark Energy Survey Collaboration et al. 2016; Lidman et al. 2020).

Continuum and emission-line light curves

The following parameters are required to model the continuum and emission-line light curves for an AGN:

- mean of the lightcurve, μ;
- damping timescale, τ_D, in days;
- long-term structure function, SF_∞, in mag;
- lag, τ, in days.

The damping timescale (also referred to as the relaxation time or characteristic time-scale) is the average time it takes for the random walk to return to the mean. The amplitude of the DRW can be described a function of the standard deviation of the DRW known as the structure function, $SF(\Delta t)$. The simulated light curves for the OzDES AGN sample need to be generated for a survey baseline of at least $\Delta t = 7$ years. The asymptotic value of the structure function at large Δt is:

$$SF(\Delta t \gg \tau_D) \equiv SF_\infty = \sqrt{2}\sigma \tag{2.2}$$

where σ is the long-term standard deviation of the variability.

The continuum lightcurve, in magnitudes, is defined by a damped random walk with a mean μ, and variable term $\Delta C(t)$:

$$C(t) = \mu + \Delta C(t) \tag{2.3}$$

where μ is the monochromatic continuum flux density at a given wavelength, converted to an apparent magnitude. The variable term at $t = 0$ is $\Delta C(t_0) = \sigma G(1)$, where σ is as defined in Equation 2.2, and $G(1)$ is a random number drawn from a Gaussian distribution with a mean of 0 and standard deviation of 1. Subsequent variable terms are given by:

$$\Delta C(t_{i+1}) = \Delta C(t_i) \exp\left(\frac{-|t_{i+1} - t_i|}{\tau_D}\right) + \sigma G(1) \left[1 - \exp\left(\frac{2|t_{i+1} - t_i|}{\tau_D}\right)\right]^{\frac{1}{2}} \tag{2.4}$$

Blandford & McKee (1982) interpret the emission-line flux variations as a response to continuum variations using:

$$\Delta L(t) = \int \Psi(\tau) \Delta C(t - \tau) \mathrm{d}\tau, \tag{2.5}$$

where $\Delta L(t)$ is the emission-line light-curve flux relative to its mean value, $\Psi(\tau)$ is the transfer function, $C(t)$ is the variable component of the continuum lightcurve flux and τ is the lag. The transfer function describes the BLR emission-line flux response to a delta function variation of the continuum flux. It has the effect of smoothing the emission-line lightcurve and shifting it, relative to the continuum lightcurve, by the lag τ. We convolve the continuum lightcurve with a top-hat transfer function to generate the smoothed and shifted emission-line lightcurve. As the true form of $\Psi(\tau)$ is complex and related to the geometry and kinematics of the BLR (Peterson 2001), we use the top-hat as an approximation. As in Zu et al. (2011), we use a top-hat transfer function of the form:

$$\Psi(t) = \begin{cases} \frac{1}{w} & \tau - w/2 < t < \tau + w/2 \\ 0 & \text{otherwise} \end{cases}, \tag{2.6}$$

Table 2.1: Coefficients of the power law relation defined for the damping timescale and structure function.

	τ_D	SF_∞
A	2.4	-0.51
B	0.17	-0.48
C	0.03	0.13
D	0.21	0.18

where w is the width of the top-hat. Following King et al. (2015) we adopt $w = 0.1\tau$.

To generate light curves for the AGN sample monitored by the OzDES RM program, the four parameters described above $(\mu, \tau, \tau_D, SF_\infty)$ were used to create a bespoke simulation for each source. The parameters were found using the apparent r-band AB magnitudes and redshifts unique to each source, as described in the following section.

Variability time-scale, τ_D, and amplitude, SF_∞

MacLeod et al. (2010) determined the following power law relationship between τ_D and SF_∞ and the physical properties of AGN:

$$\begin{aligned}\log_{10}(\alpha) = A_\alpha + B_\alpha \log_{10}\left(\frac{\lambda}{4000}\right) + C_\alpha(M_i + 23) \\ + D_\alpha \log_{10}\left(\frac{M_{\rm BH}}{10^9 M_\odot}\right)\end{aligned} \tag{2.7}$$

where α refers to τ_D (in days) or SF_∞ (in mag), λ (Å) is the rest-frame continuum wavelength, M_i is the absolute i-band magnitude of the source and $M_{\rm BH}$ is the mass of the black hole (in solar masses). The coefficients are given in Table 2.1. The correlations were found after converting timescales to the rest-frame of the sources, therefore the estimated τ_D values were multiplied by $(1+z)$ to create simulated light curves in the observed frame.

The black hole mass that is often used in simulations of this type is that predicted from the following Gaussian distribution used by MacLeod et al. (2010):

$$P(\log_{10} M_{\rm BH}|M_i) = \frac{1}{\sqrt{2\pi\sigma^2_{M_{\rm BH}}}} \exp[-\frac{(\log_{10} M_{\rm BH} - \log_{10} \overline{M}_{\rm BH})^2}{2\sigma^2_{M_{\rm BH}}}] \tag{2.8}$$

with mean $\log_{10} \overline{M}_{\rm BH} = 2.0 - 0.27 M_i$ and standard deviation $\sigma_{M_{\rm BH}} = 0.58 + 0.011 M_i$ which signifies the dispersion in the black hole population.

2.2.3 Window functions

The dominant observational effect on lag recovery is expected to be the survey window function. For our simulations we apply custom window functions to model observed light curves. We apply a custom window function that samples the original simulated light curves with a desired baseline, season length, and photometric or spectroscopic cadence (for the continuum and emission-line light curves, respectively). To be representative of the uneven sampling of surveys, we permit a scatter range for the cadence (e.g., 14 ± 4 days), drawing the dates from a uniform distribution.

2.2.4 Lag Recovery

One of the most widely used lag recovery techniques is the interpolated cross-correlation function (ICCF, Gaskell & Peterson 1987). In order to focus on the effects of the window function over the critical variables, we chose not to use the more complex `JAVELIN` (Zu et al. 2011) methodology in this work. For comparisons of the ICCF and `JAVELIN` lag recovery methods, see Li et al. (2019), Yu et al. (2020b), and Penton et al. (2022).

We use the ICCF method as described by Peterson et al. (1998), and summarised here. The recovered lag and its uncertainty are measured using the flux randomisation and random subset sampling (FR/RSS) method. Since the ICCF method does not directly use the flux measurement uncertainties when computing the cross correlation function (CCF), flux randomisation accounts for the uncertainties by shifting the original flux values by Gaussian deviates based on the standard deviation on the fluxes. The random subset sampling accounts for the effect of any one flux measurement on the lag measurements, by randomly selecting light curve points with replacement (resulting in a sample ∼37% smaller than the original set). Both the continuum and emission-line light curve are altered by this FR/RSS process. A CCF is computed with the continuum light curve and the linearly interpolated

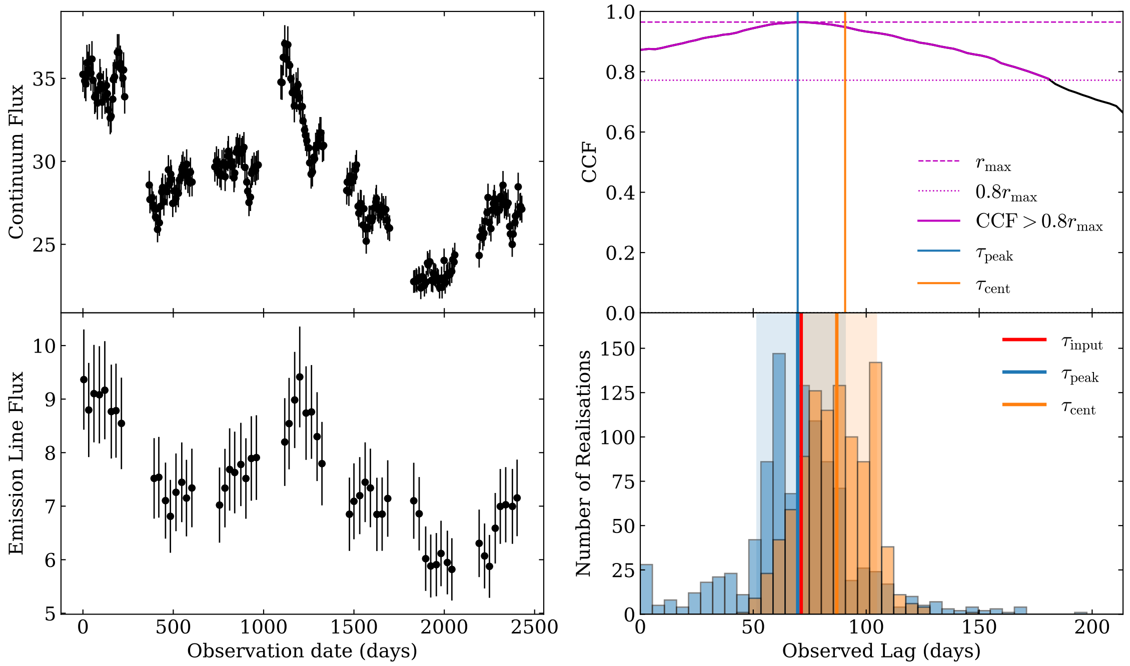

Figure 2.2: Example of the interpolated cross-correlation function (ICCF), applied to a pair of simulated light curves. The left panels show the simulated continuum and emission-line light curves. The top right panel shows the cross-correlation function computed using ICCF, highlighting the section of the CCF used to compute the centroid, and the peak lag and centroid lag measurement from this CCF. The bottom right panel shows the cross-correlation centroid distribution (CCCD) in orange, and the cross-correlation peak distribution (CCPD) in blue, with the vertical lines and shaded regions indicating the recovered lag and its uncertainty, from each distribution. The red line indicates the input observed-frame lag, τ_{input}, for the source.

emission-line light curve, which are cross correlated as a function of time lag. The light curve is linearly interpolated at a specified time lag spacing. Another CCF is computed using the linearly interpolated continuum light curve and the emission-line light curve. The final CCF is the average of these two CCF's. The lag is the time at which the peak of the final CCF occurs.

A cross-correlation peak distribution (CCPD) is obtained with the lags found from 1000 Monte Carlo realisations of FR/RSS. The recovered lag is taken to be the median of the CCPD, and the uncertainties are the upper and lower limits which contain 68.27% of the realisations (equivalent to 1σ uncertainties of a normal distribution). An example is shown in Figure 2.2. The centroid measurement is also commonly used, as recommended by Peterson & Horne (2004), which is computed as the median of the CCF values $> 0.8r_{\mathrm{max}}$ counted out from the peak of the CCF.

In this work the peak lag was found to be more accurate and consistent than the centroid lag, when dealing with various CCF shapes (which arise due to varied light curve sampling). For example, as shown in Figure 2.2, the centroid measurements were often skewed toward the centre of the lag prior range due to the broad, flat shape of the CCF, and our use of a non-negative lag prior. We investigate the effect of the lag prior in §2.3.2.

When computing the CCF, we use the PyCCF python code (Sun et al. 2018), setting the interpolation grid spacing to be 3 days. We set the r_{max} threshold to be 0, and disable the automatic use of the p-value test to set the r_{max} threshold.

2.3 Results

2.3.1 Window function parameter space

There are three critical components to the observational window function: observation cadence, the length of the seasonal gap, and the survey duration. In principle the cadence of photometric and spectroscopic data can be varied independently. However initial experimentation indicated that, under the assumption that photometric data is highly likely to be available with greater frequency than the associated spectroscopy, the cadence of said photometry has limited bearing on lag recovery. We therefore proceed with a simplified model for observational cadence, varying photometric and spectroscopic observations in lockstep.

To probe the observational window parameter space, we conducted three sets of simulations: the first keeping the baseline of the survey fixed (reflecting the 6 year OzDES survey) while varying the cadence and season length, the second keeping the cadence constant (weekly photometry and monthly spectroscopy) while varying the baseline and season length, and the third keeping the season length constant (5 months) while varying the cadence and baseline.

To model various survey cadences the light curves were down-sampled sequentially over 10 levels, ranging from daily photometry and spectroscopy, to weekly photometry and monthly spectroscopy. This last down-sampling level approximately models

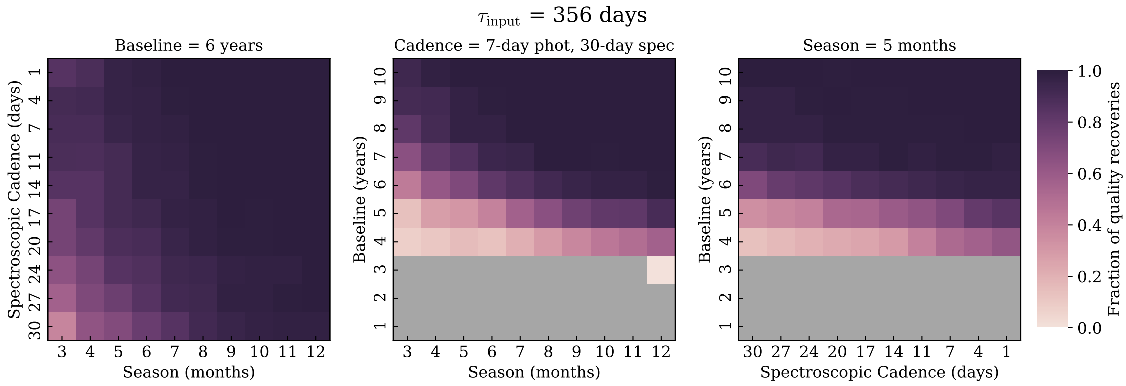

Figure 2.3: The fraction of quality lag recoveries, across the window function parameter space, for a source with $\tau_{\rm input}$=356 days. The fixed component of the window function is labelled above each panel. The blank regions are where the baselines of the light curves were shorter than the lag prior range.

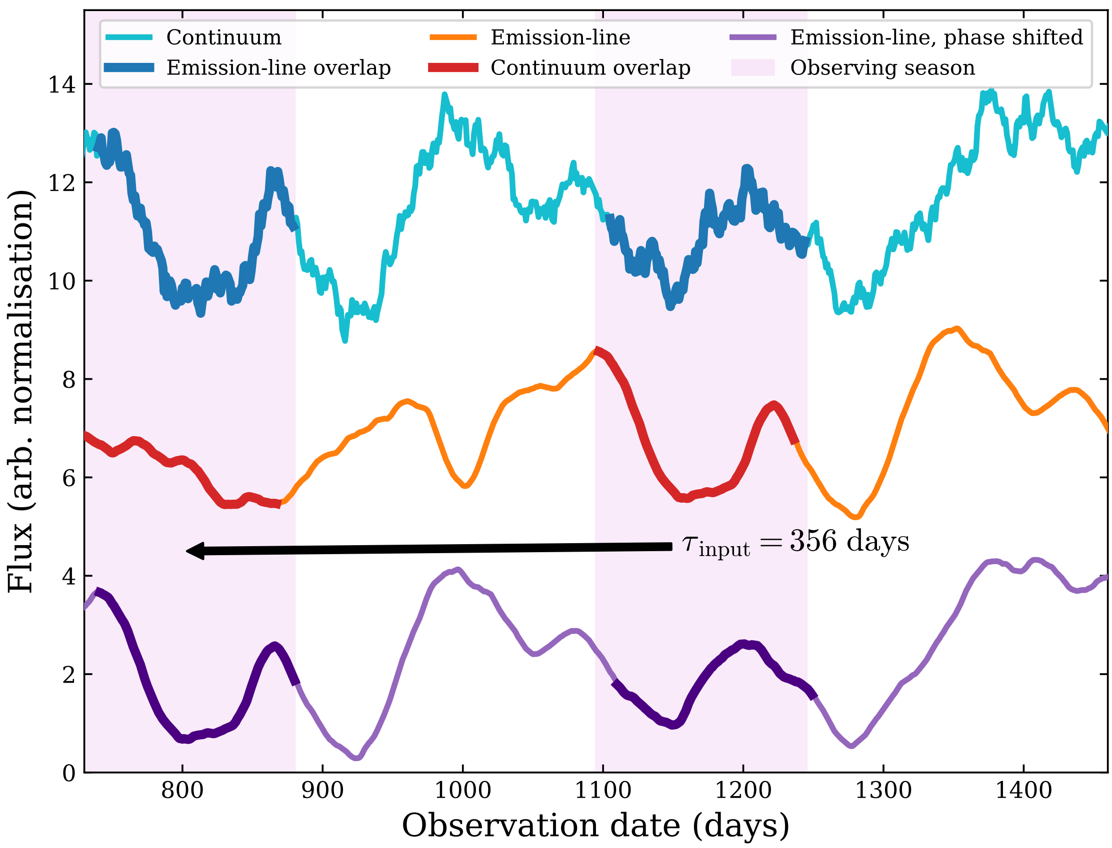

Figure 2.4: A 2-year section of simulated continuum and emission-line light curves, at daily cadence, with $\tau_{\rm input}$=356 days. For clarity, the light curve flux errors are not shown here. The phase-corrected emission-line light curve is shown at the bottom. The darkened portions of the light curves indicate where the continuum and emission-line light curves overlap within the observing seasons. As the emission-line light curve lags the continuum by 356 days, the reverberation is seen almost exactly one year later.

the DES and OzDES observational cadence. More densely sampled photometry was chosen as it is more readily obtainable and has been shown to improve lag recovery (Shen et al. 2015). The season length was extended by one month at a time, starting from 3 months up to the maximum possible season length of 12 months. The baseline was extended successively by one year, from 1 year to 10 years. Each window function was applied to 100 pairs of light-curve realisations created for a source.

To best demonstrate the interactions between the lag and various window function timescales, we simulated sources with $\tau_{\rm input}$ ~2 months, ~5 months, ~12 months, and ~18 months.

Our goal is to determine, across the observational parameter space, the fractional recovery of accurate lag measurements with acceptable precision. For each simulated input lag value, we consider the fractional recovery rate for each survey window function realisation. We require a quality lag recovery to be within 10% (and 100 days) of $\tau_{\rm input}$, and ≥ 4 times the statistical uncertainty on the lag measurement provided by ICCF. Following King et al. (2015), we use a lag prior of 0 to $3\tau_{\rm expected}$.

Figure 2.3 shows the fraction of quality recoveries for a source with a lag of $\tau_{\rm input}=$ 356 days, through the window function parameter space. For this source with a lag close to one year, there is extensive overlap between the photometry and spectroscopy, albeit from campaign seasons in different years, as shown in Figure 2.4. This lag can be recovered with short seasons and low cadence, with a sufficiently long baseline. Even subtle variability features seen within short seasons will be directly observed in the emission-line light curve. The first results from OzDES (Hoormann et al. 2019) were for C IV sources with observed lags $\approx$ 1 year, as they could be reliably recovered when only the first four years of data were recorded.

We repeat this for sources with various input lags. Figure 2.5 shows the fraction of quality recoveries for a selection of sources with various observed-frame lags, through the window function parameter space. For a source with an input lag of $\tau_{\rm input} = 142$ days, there is significant improvement in the fraction of quality recoveries as the seasonal gap is reduced. As this lag is almost 5 months in the observed frame, it is challenging to recover when the season length is equal to or shorter than the

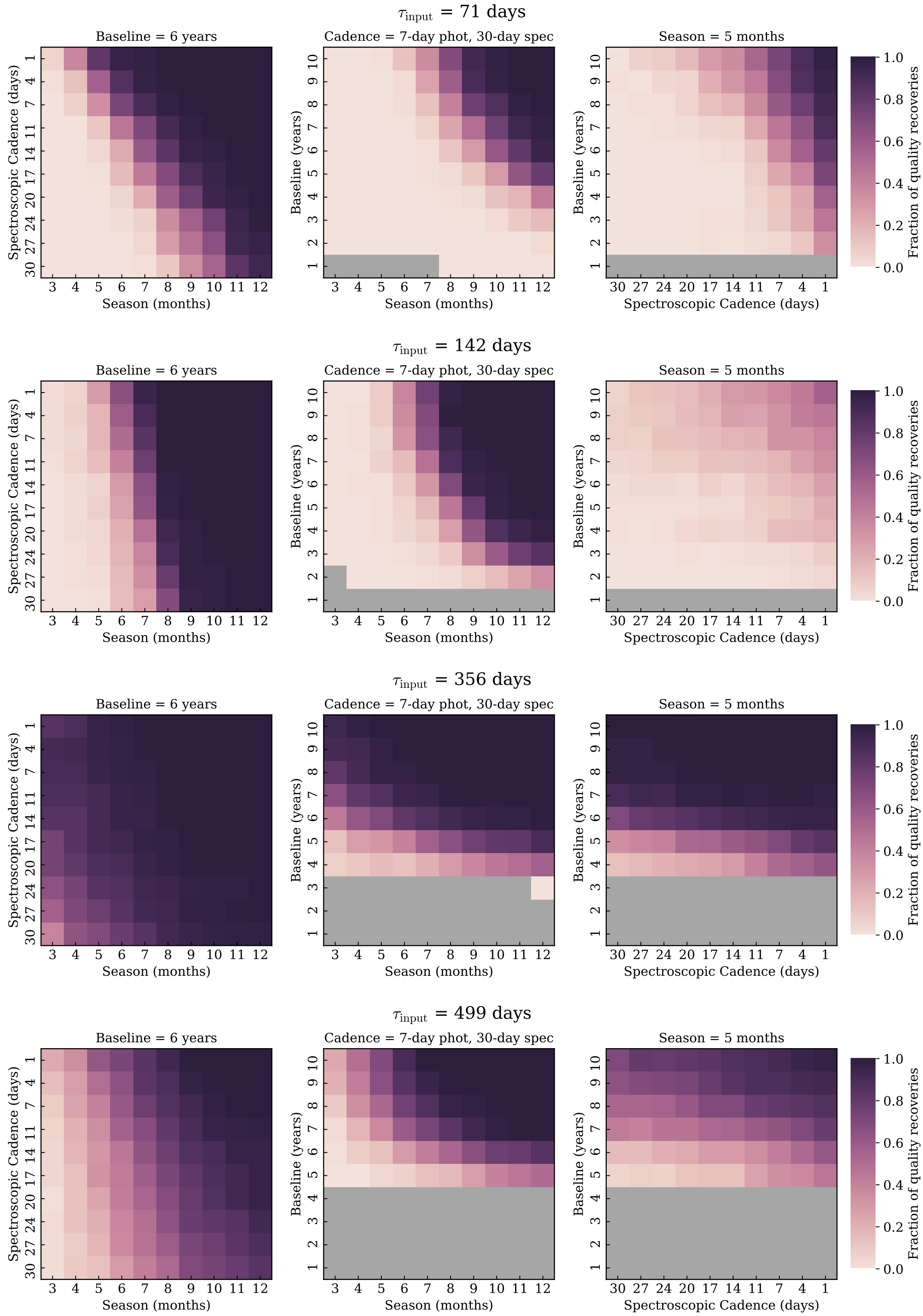

Figure 2.5: Each row presents the fraction of quality lag recoveries for sources with various input lags, which are labelled above each row, across the window function parameter space. The fixed component of the window function is labelled above each panel. The blank regions are where the baseline of the light curves is shorter than the lag prior range.

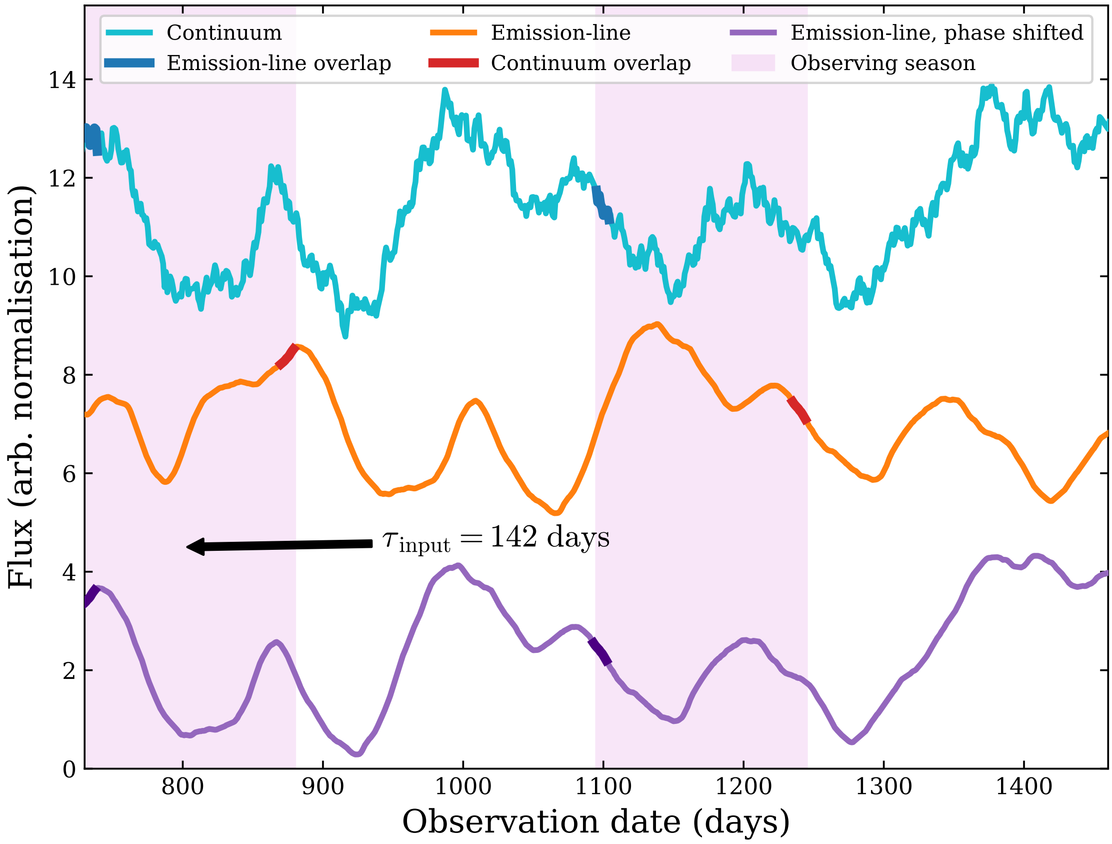

Figure 2.6: A 2-year section of simulated continuum and emission-line light curves, at daily cadence, with $\tau_{\rm input} = 142$ days. For clarity, the light curve flux errors are not shown here. The phase-corrected emission-line light curve is shown at the bottom. The darkened portions of the light curves indicate where the continuum and emission-line light curves overlap within the observing seasons. As the emission-line light curve lags the continuum by 142 days, the direct reverberation response begins when the observing season ends, so it cannot be observed.

lag. The direct response of the broad-line region to the variability of the ionising continuum occurs mainly outside of the 5-month observing season, as shown in Figure 2.6. Recovery of a reverberation signal from such a source would therefore rely on higher-order correlation timescales, such as the variability relaxation time, as presented by (e.g., Grier et al. 2019; Homayouni et al. 2020; Yu et al. 2021).

We see similar trends for the source with $\tau_{\rm input} = 500$ days (Figure 2.5). This is expected as this lag coincides with the second seasonal gap. However, the second order effect due to the damping timescale results in the lag being moderately recoverable even with seasonal gaps present, as information is present in the smoother long-term variations seen on timescales longer than the lag itself.

For a source with a lag of $\tau_{\text{input}} = 71$ days (and with a fixed survey baseline of 6 years) there is significant overlap between the photometric and spectroscopic window function within each campaign season. Unsurprisingly, we find that increasing the observational cadence improves the precision of lag recovery, although it has limited impact on accuracy, which requires closing the seasonal gap (maximising the overlap between photometry and spectroscopy with each campaign season) to achieve significant improvement. The light-echo in the emission-line light curve for this source begins around 71 days, therefore, as with the 142-day lag, we require a long enough season length to provide sufficient overlap to allow lag recovery. We see the relatively short lag can still be well recovered with the fixed cadence, if there is a sufficiently long baseline and extended season length. As the baseline or season length increase, the chance increases of seeing favourable structure to variability (*i.e.,* significant large flux excursions from the mean on short timescales).

2.3.2 Quality vs. Quantity

We extend these simulations to a sub-sample of OzDES sources. These sources were selected based on their expected lags, to cover the range of expected observed-frame lags for this sample. As most of our sources have expected observed-frame lags up to 1000 days (Figure 2.1), we set this as the upper limit for these simulations. We apply window functions that vary one component at a time, using a constant number of data points. This allows us to directly compare how each component of the window function affects the recovery of a particular lag. We added approximately 90 photometric epochs and 20 spectroscopic epochs to the base OzDES window function, by independently changing one component of the original window function. In addition to applying the base OzDES window function, we conducted three sets of simulations with the following window function changes: only the season extended (from 5 to 9 months), with the baseline extended (from 6 to 10 years), and with increased cadence (from (7,30) to (4,18) days for the (continuum, emission-line) light curves, respectively).. Lags were recovered for each of 100 pairs of light curve realisations created for each simulated source.

The top panel of Figure 2.7 shows the median and 1σ scatter of the recovered lags

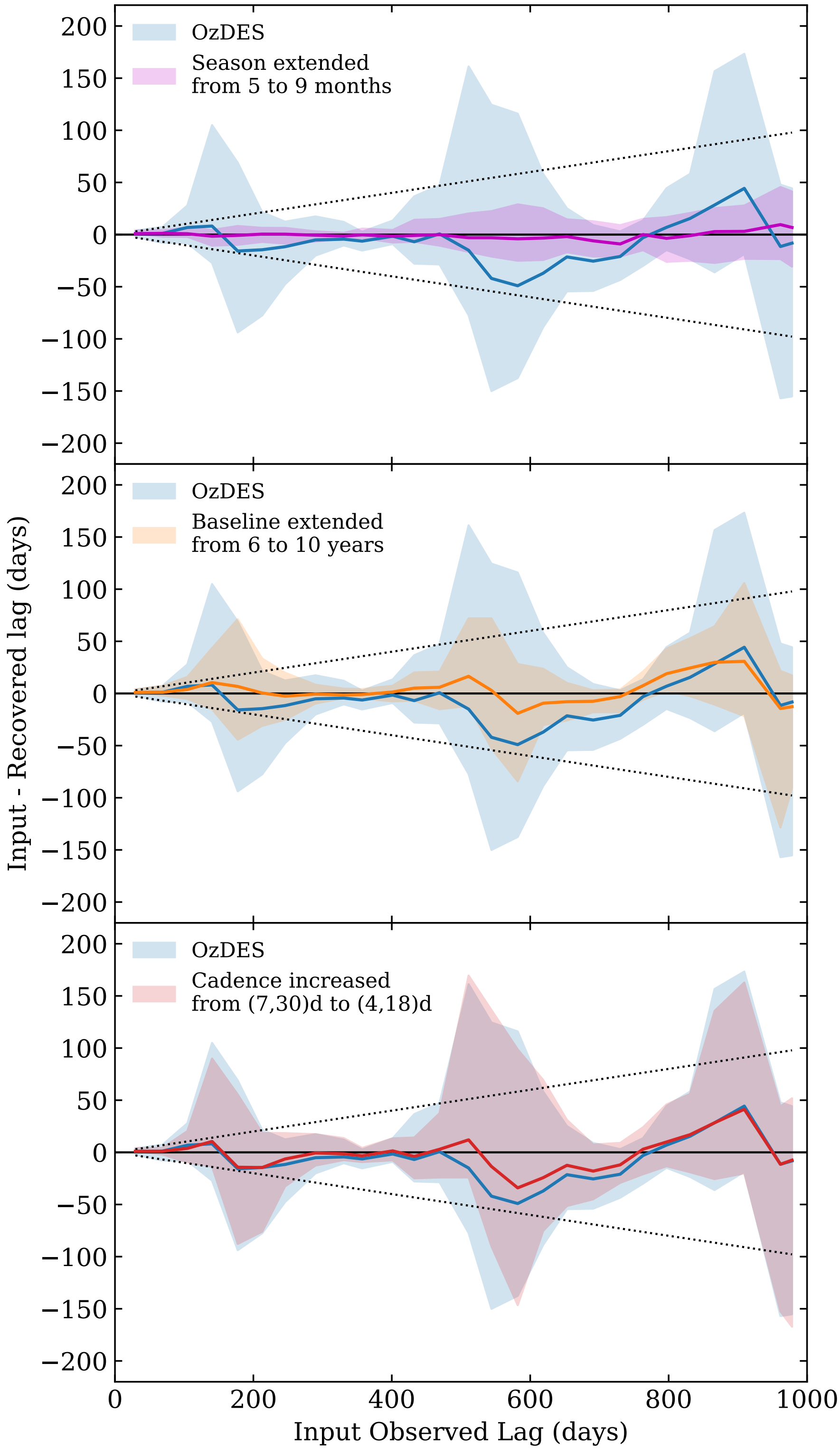

Figure 2.7: The median (solid lines) and 1σ scatter (shaded regions) of recovered lags from 100 realisations, at each input lag. The results of the simulations with the original OzDES window function are shown in blue, along with the results of the following window functions (top to bottom): extended season, extended baseline, and increased cadence. The black dotted lines indicate 10% of the input lag, which is our criteria for a correct recovery.

for the simulations in which only the season was extended, compared to the results with original OzDES window function. The same is shown in the middle panel of Figure 2.7, for the case with the baseline extended, and in the bottom panel for case with increased cadence. The lags reported here have been recovered from ICCF directly, without any recovery criteria applied.

When sampled by the OzDES window function we see the results expected from the trends observed in §2.3.1. There is broad scatter in the recovered lags where the input lag is $n+1/2$ years long, where n is an integer number of years (*i.e.*, coincident with seasonal gaps). Input lags coinciding with the annual seasonal overlap are recovered accurately, regardless of the window function applied (at the observational data densities considered). The scatter in the lags is significantly reduced across all input lags when the season length is extended. The extension of the baseline reduces the scatter to a greater extent than increasing the cadence. Although the lags are recovered more accurately in these latter cases, a considerable number of lags remain outside the limits for a correct recovery. In these simulations we clearly see the advantage of extending the season length for a large-scale survey hoping to recover lags ranging from tens to hundreds of days.

Effect of the lag prior

There is little consistency within the literature for the priors placed on lag recovery in RM analyses. Whilst there is no objective way to choose a prior, they need to be wide enough to avoid confirmation bias, but also not so wide as to lose the lag in noise or aliasing signals. We investigate the effect of changing the lag prior on lag recovery. Our initial simulations used $0 \rightarrow 3$ times the expected lag $\tau_{\rm exp}$ (which is the same as the $\tau_{\rm input}$ for our simulations), with a maximum allowed prior of 1300 days (about two-thirds of a 6-year baseline). We repeat the lag estimation process using the following lag priors, in order of most broad to most narrow:

- $\pm$ 1300 days
- $\pm 3\tau_{\rm exp}$, with a lower bound of -1300 and upper bound of 1300 days.
- $(1 \pm 2)\tau_{\rm exp}$, with a lower bound of 0 and upper bound of 1300 days.

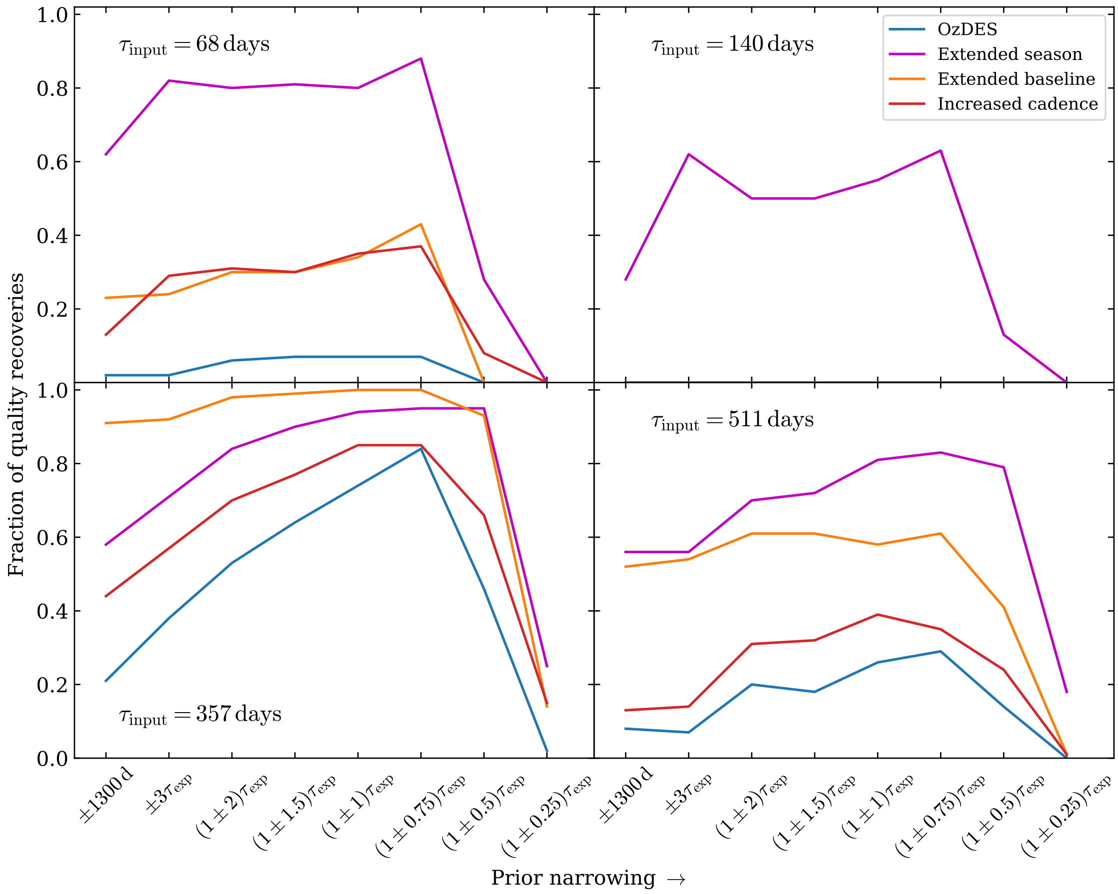

Figure 2.8: The fraction of quality recoveries for sources with various input lags, which are labelled on each panel, for simulations run with various priors. The results are shown for four different window functions. For τ_{input}=140d, the curves for three of the window functions (OzDES, extended baseline, and increased cadence) are not visible as they have zero fraction of quality recoveries with all lag priors.

- $(1 \pm 1.5)\tau_{\mathrm{exp}}$, lower bound of 0, upper bound of 1300 days.
- $(1 \pm 1)\tau_{\mathrm{exp}}$, lower bound of 0, upper bound of 1300 days.
- $(1 \pm 0.75)\tau_{\mathrm{exp}}$, lower bound of 0, upper bound of 1300 days.
- $(1 \pm 0.5)\tau_{\mathrm{exp}}$, lower bound of 0, upper bound of 1300 days.
- $(1 \pm 0.25)\tau_{\mathrm{exp}}$, lower bound of 0, upper bound of 1300 days.

Figure 2.8 shows the fraction of quality recoveries with the above priors, for four sources with various input lags. The sources chosen here have lags similar to the sources used for the simulations in Figure 2.5. Although a prior of $(1 \pm 0.75)\tau_{\mathrm{exp}}$ maximises the recovered fraction in most cases, this is very narrow and would result in confirmation bias in RM studies. Overall, when a window function is applied that efficiently recovers a particular lag, it is recovered well and the recovery is mostly unaffected by the prior. This becomes more complex when a lag can be recovered with a certain window function, but less effectively with other window functions. In this case, the recovered fraction can vary greatly depending on the prior.

2.3.3 Redshift-Luminosity parameter space

We now consider the extended parameter space of observations required for cosmological studies. We generate a simulated grid of AGN (similar to Shen et al. 2015; King et al. 2015; Li et al. 2019), with $16 < m_r(\mathrm{AB}) < 23$ over the redshift interval $0 < z < 5$. The redshift-luminosity range slightly exceeds the range covered by the OzDES and SDSS-RM samples but is inline with what is expected from future generation surveys (e.g., Kollmeier et al. 2017; Brandt et al. 2018; Swann et al. 2019; The MSE Science Team et al. 2019). There are also redshift regions where more than one emission line is visible. These regions are particularly valuable as multiple lags can be recovered independently for one source, allowing the ionisation stratification of the BLR to be studied. Future surveys conducted with the Maunakea Spectroscopic Explorer (MSE, The MSE Science Team et al. 2019) will have access to both the optical and near-infrared bands (J and H). This will allow observation of the Hβ and Mg II lines at higher redshifts due to the extended wavelength coverage, and increase the range over which two or more emission lines are visible simultaneously for a source. We conduct separate simulations for each emission line, over the redshift range of the grid for which the emission line will be visible with future optical and near-IR surveys. We simulate a pair of light curves for each of 100 AGN per bin, with the expected lag for the relevant emission line.

We apply a representative window function of the upcoming LSST and TiDES RM survey to each AGN across the grid. The 5-year baseline planned for 4MOST/TiDES survey (Swann et al. 2019) will provide 14 ± 4 days spectroscopic sampling, combined with the VRO/LSST RM program (Brandt et al. 2018) which proposes to deliver a photometric cadence of $\sim$2 days for each of the four deep-drilling fields. LSST will be conducted using the Rubin Observatory at Cerro Pachón (-30.2°), and TiDES by the VISTA telescope at the Paranal Observatory (-24.6°). Figure 2.9 shows that the

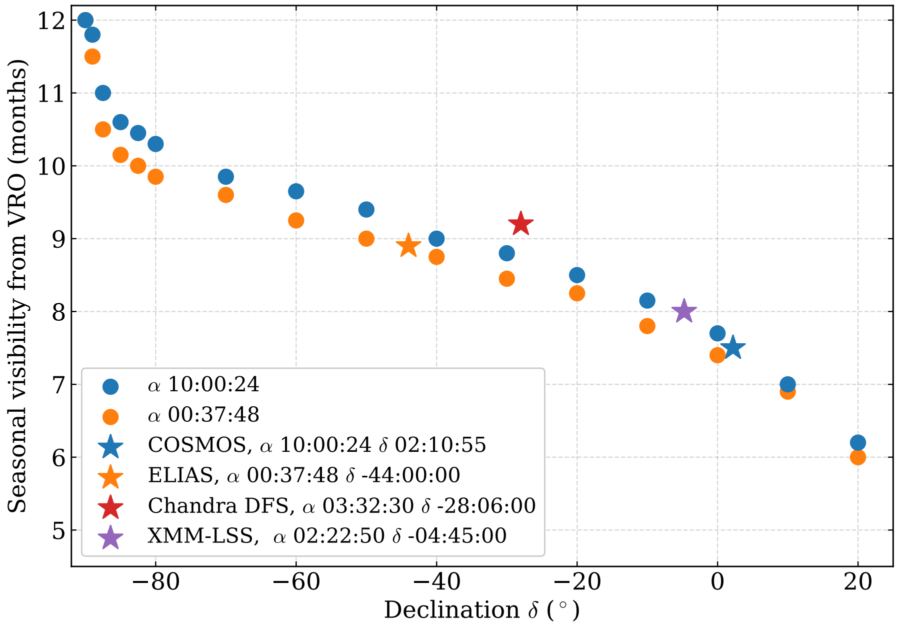

Figure 2.9: The maximum seasonal visibility at or above an airmass of 2.0 for the four proposed deep-drilling fields for LSST, from the Vera Rubin Observatory at Cerro Pachón (-30.2°). The fields are required to be visible for at least half an hour between astronomical (-18°) twilights. For reference, the visibility is also shown for hypothetical fields with various declinations, for two right ascensions. At a declination of -90°, fields would be observed at an airmass of 2.0 year-round from this site.

Chandra DFS and ELIAS fields, with the most southerly declination, are visible for the longest maximum season of ∼9 months. The equatorial COSMOS and XMM-LSS fields are visible for a maximum of 7.5 and 8 months, respectively. Using the shortest season, we adopt for our baseline survey the window function with a 5-year baseline, 7-month season length, photometric cadence of 2 days and spectroscopic cadence of 14 ± 4 days.

As previously noted, we define a quality lag recovery to be ≥ 4 times the statistical uncertainty of the lag measurement provided by ICCF, and within 10% and 100 days of the input lag. The fraction of quality lag recoveries, for this representative LSST/TiDES window function, is shown in Figure 2.10, as a function of apparent magnitude and redshift, bounding the probable observable survey parameter space.

We see a banded structure in this *visibility map* with high recovery fractions achieved only for sources with observed lags that are out of phase with the seasonal gaps in the window function. Our grid has a resolution of 0.25 in m_r(AB) and 0.05 in

z, which is significantly higher than previous simulations. This was necessary to resolve the high-frequency structure. The highest fraction of quality recoveries are for lags in the region with expected lags between 14 and 180 days, *i.e.,* when the lag occurs within a single campaign season. This lower limit is set by the spectroscopic cadence of 14 day, and the upper bound is the length of the season, which is ~210 days. Beyond this timescale, it becomes challenging to reliably recover lags of longer duration until we approach lags on order of one year, at which point the photometric and spectroscopic observations come back into phase. The pattern is repeated for longer observed-frame lag times at 2 and 3 years, although these bands are fainter due to the limited baseline.

We have shown in Figure 2.5 that extending the season length (closing the seasonal gaps in the window function) generates the greatest improvement in lag recovery rate, followed by extending the survey baseline (§2.3.2). We repeated the simulations with three season lengths (5, 7 and 9 months) and two baselines (5 and 10 years). In Figure 2.11 and Figure 2.12, the panels show the results of these simulations with the various window functions, for Hβ and C IV lags. We do not perform simulations for Mg II lags separately as there are few measurements constraining this relation (Trakhtenbrot & Netzer 2012), with a large scatter in recent results (Homayouni et al. 2020). Although there are few sources with lags measured with both Hβ and Mg II (e.g. Clavel et al. 1991; Metzroth et al. 2006; Homayouni et al. 2020), the lags are found to be similar. Therefore we extend the range of the Hβ simulations to also cover the range of visibility of Mg II with future near-IR facilities.

By extending the baseline to 10 years, the survey becomes much more sensitive to lags around 1 and 2 years. However, the seasonal gaps are still limiting a significant region of this parameter space. We see that the gap in quality recoveries around ~180 days effectively disappears once we extend the season to 9 months. Finally, when both the baseline and season are extended, we see quality lag recoveries for almost all AGN across the parameter space, with the fraction decreasing only for lags longer than 2-3 years. For these longest lags, the lag recovery could benefit from revising/reducing the lag prior (§2.3.2) or extending the baseline further.

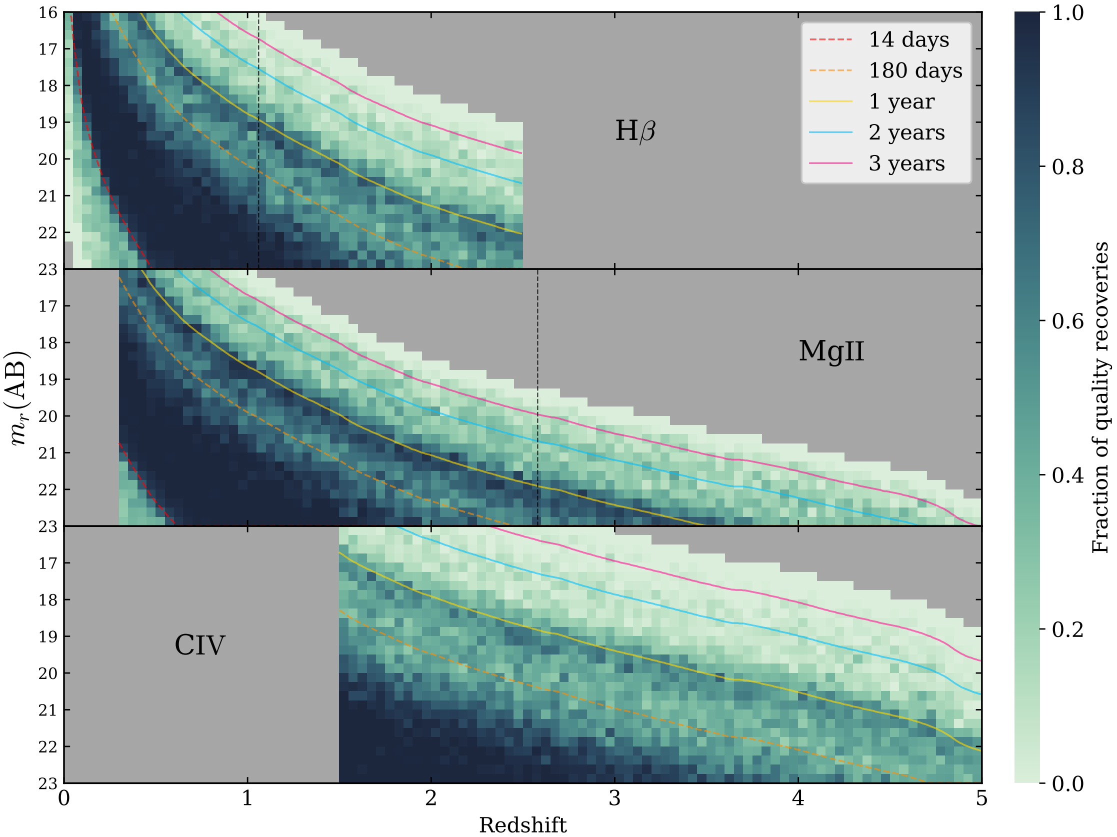

Figure 2.10: The fraction of quality recoveries across the AGN redshift-luminosity space, with light curves sampled with a representative LSST and TiDES survey window function (5-year baseline, 7-month seasons, 2d photometric and 14d spectroscopic cadence). The time-lag contours indicated by the coloured lines show constant expected observed-frame lag through this parameter space, calculated using published $R-L$ relations for each emission line (Bentz et al. 2013; Trakhtenbrot & Netzer 2012; Hoormann et al. 2019). The upper limit on the prior is 1500 days, sources with input lags above this have been masked. For reference, the black vertical lines indicate the redshift at which the respective emission lines are visible at a wavelength of 1 micron (10000 Å); representing the transition between visible light and infrared for spectroscopic capabilities. The sensitivity of spectrographs drop off significantly and systematic errors increase near the edges of the wavelength region. Note that this effect is not considered in these simulations.

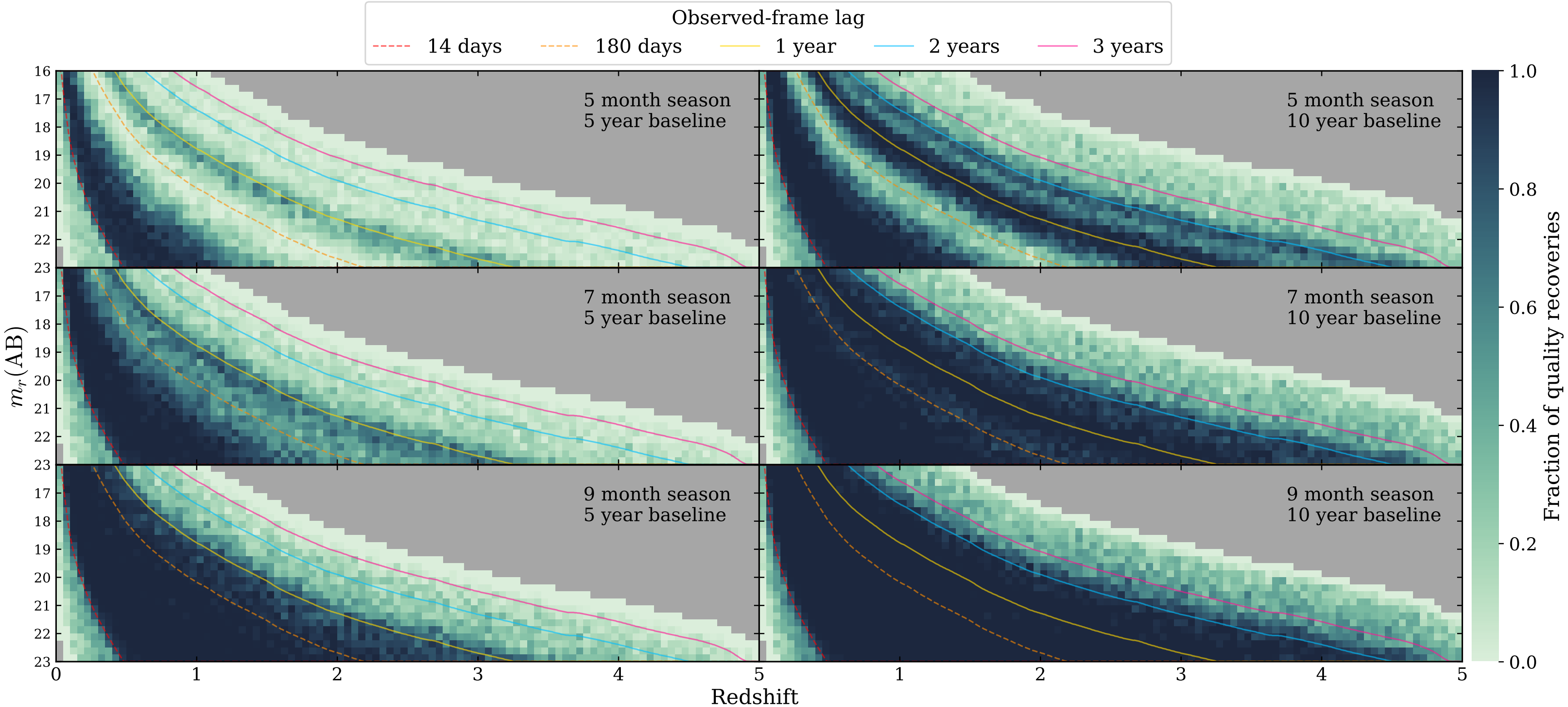

Figure 2.11: The fraction of quality recoveries across the AGN redshift-luminosity space for Hβ lags, with light curves sampled by the LSST/TiDES window function labelled on the respective panel. The time-lag contours indicated by the coloured lines show constant expected observed-frame lag through this parameter space, calculated using the Bentz et al. (2013) $R - L$ relation. Sources with input lags above the respective prior limits have been masked.

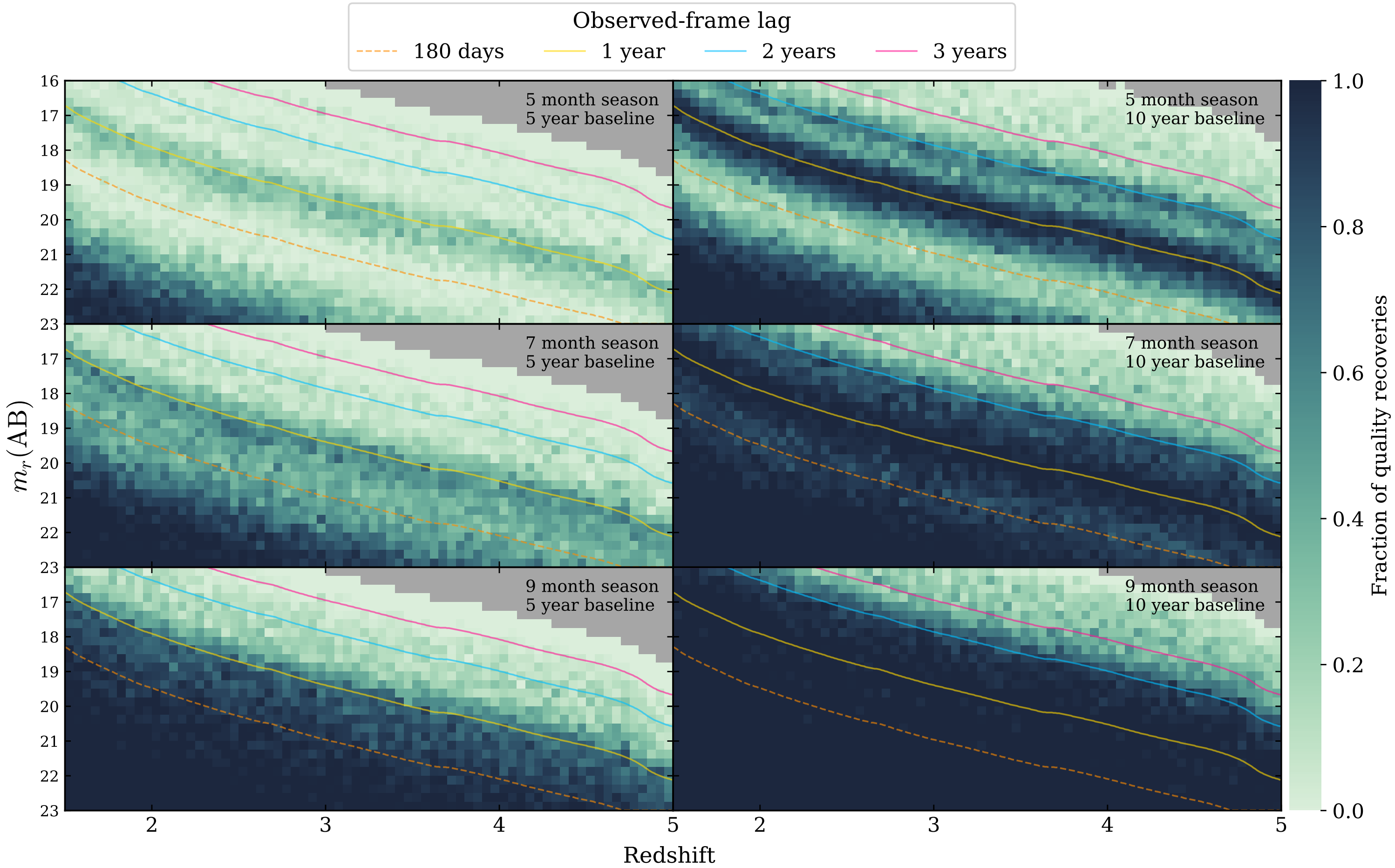

Figure 2.12: The same as Figure 2.11 shown for C IV lags. The time-lag contours indicated by the coloured lines show constant expected observed-frame lag through this parameter space, calculated using the Hoormann et al. (2019) $R - L$ relation. Sources with input lags above the respective prior limits have been masked.

Table 2.2: The percentage of quality recoveries for a mock target sample from the visibility maps of each window function, done for each emission line (see Figures 2.11 and 2.12).

	Hβ		C IV	
WF	5 years	10 years	5 years	10 years
5 months	18.6	63.3	18.9	53.0
7 months	38.5	82.7	61.0	95.2
9 months	54.5	87.7	92.7	99.8

Survey efficacy and the $R-L$ relation

We defined a mock target sample using the redshifts and apparent r-band magnitudes of the OzDES RM sample (see Figure 2.1). Each mock target was randomly selected from the respective redshift-luminosity bin on the simulation grid. We calculated the percentage of sources with a quality lag recovery. Table 2.2 shows the mean percentage for each window function simulation.

The visibility maps created from our simulations show banding structure in AGN luminosity-redshift space for lag recovery efficacy. This identifies regions of this parameter space where reverberation mapping is more likely to be successful, and we use this to inform survey planning. This would require understanding the biases introduced by the specific window function, as certain lags, and therefore certain luminosity-redshift bins, will be over-represented when constraining new $R-L$ relations. We defined a 'visible' mock sample comprised of sources in the mock sample selected from a redshift-luminosity bin with an overall fraction of quality recoveries ≥ 0.5. The $R-L$ relation was constrained using the full mock sample, and again using only the 'visible' mock sample, using the Bivariate Correlated Errors and Intrinsic Scatter (BCES) code (Akritas & Bershady 1996; Nemmen et al. 2012). This result is shown in Figure 2.13 for each window function of the C IV simulations, with the respective $R-L$ relation fit parameters provided in Table 2.3. The scatter in the recovered lags from the mock samples is reduced significantly as the season length and baseline are extended. The dynamic range in luminosity of the 'visible' mock sample is limited when the season length and baseline are short. As a result of statistical leverage, the slope of the recovered $R-L$ relation is shallower. Although the scatter in the recovered lags is greater for the full mock sample, the slope recovered for the $R-L$ relation is consistent within the fitting error.

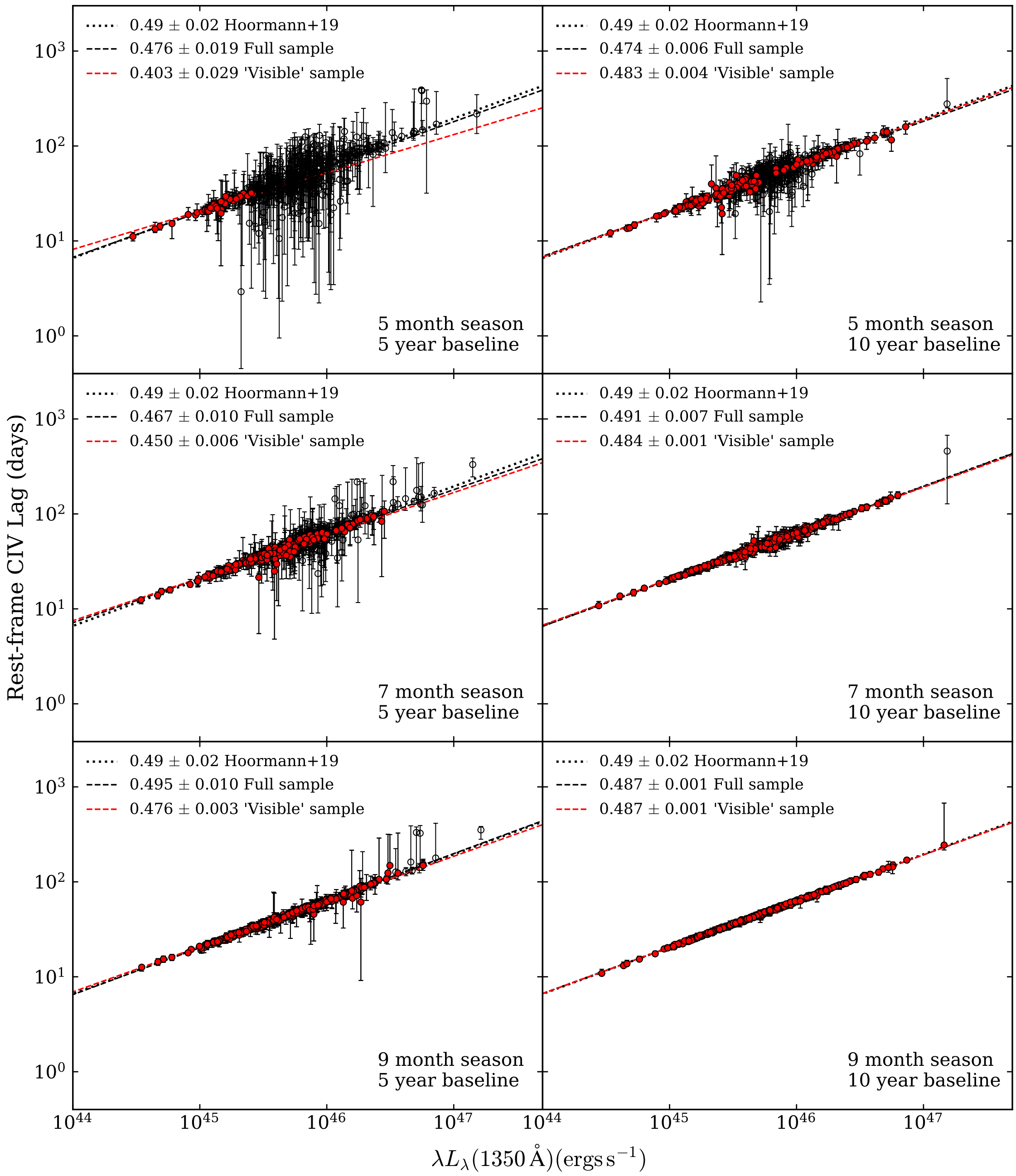

Figure 2.13: The recovered lags and respective uncertainties for the full mock target sample (black), and 'visible' subsample (red), from each window function simulation. The C IV $R-L$ relations constrained using the full mock sample and using only the 'visible' subsample are shown, along with the input $R-L$ relation from Hoormann et al. (2019). The slopes for each relation are provided in the legend on each panel.

Table 2.3: The best fit slope and intercept parameters of the $R - L$ relation fits in Figure 2.13.

	Full sample		'Visible' sample	
WF (season, baseline)	α	β	α	β
5 months, 5 years	0.476 ± 0.019	0.828 ± 0.032	0.403 ± 0.029	0.911 ± 0.034
5 months, 10 years	0.474 ± 0.006	0.838 ± 0.009	0.483 ± 0.004	0.828 ± 0.007
7 months, 5 years	0.467 ± 0.01	0.854 ± 0.016	0.45 ± 0.006	0.875 ± 0.009
7 months, 10 years	0.491 ± 0.007	0.817 ± 0.012	0.484 ± 0.001	0.841 ± 0.006
9 months, 5 years	0.495 ± 0.01	0.812 ± 0.017	0.476 ± 0.003	0.841 ± 0.006
9 months, 10 years	0.487 ± 0.001	0.823 ± 0.002	0.487 ± 0.001	0.823 ± 0.002

2.4 Discussion

It is evident that the window function has a significant effect on the reverberation mapping lag recovery over a range of AGN intrinsic and observed properties.

- *Cadence:* Improvement in the precision of lag recovery gained by increasing the observational cadence is an expected result, as previous studies have also shown (White & Peterson 1994; Shen et al. 2015; King et al. 2015). This is particularly pronounced for sources with shorter lag times (for which low observational cadence is not readily compensated through simply extending the survey baseline). However, for sources with longer observational lags, the baseline is critical even if only modestly sampled. This naturally suggests a multi-tiered observational strategy when resources are restricted (typically the case for spectroscopy), similar to that used by SDSS-RM (Shen et al. 2015).

- *Baseline:* The effect of the baseline on the ability to recover long lags had been predicted (Shen et al. 2015; King et al. 2015), although current surveys are only now reaching sufficient baselines to confirm such assumptions (Shen et al. 2019b; Hoormann et al. 2019).

- *Season length:* While the limits imposed by seasonal gaps had been recognised previously (Zu et al. 2011; King et al. 2015), their impact had not been fully appreciated until recent industrial-scale surveys delivered their early results, which required implementing alias removal techniques (Grier et al. 2019; Homayouni et al. 2020).

This has motivated our work to investigate the interplay of each of these observational window function components in more detail. A large portion of sources observed by current industrial-scale RM surveys have expected observed-frame lags in the sub-year range, as seen in Figure 2.1, leaving them vulnerable to the impact of seasonal gaps. This is a cause of concern for current and future surveys, which have or are expected to have significant seasonal gaps, as it limits the number of lags that can be reliably recovered.

2.4.1 LSST/TiDES

From the population simulations conducted with the LSST/TiDES window function, we were able to predict the efficacy of this RM survey. The TiDES sample comprises 700 AGN at $r < 21$ and $z < 2.5$ (Swann et al. 2019). Focusing on this region of the parameter space, we see that the season length imposes critical limitations on the areas where the survey would be able to successfully recover quality lags. We demonstrated the vast improvement apparent with altered window functions where the baseline or seasons were extended. As LSST is planned to operate for 10 years, it is feasible to extend the TiDES program to cover the same baseline. However, the field visibility cannot not be changed, therefore the efficacy in certain redshift-luminosity ranges will be restricted for the equatorial fields. Significant seasonal gaps may not cause as much of an issue for sources with long relaxation times. However, this would require long survey baselines, of at least 6 years; beyond what is currently planned.

As shown in Figure 2.9, the south celestial pole, and hence circumpolar fields, are visible year-round from the Rubin Observatory, but at a zenith angle of 60° (airmass of 2.0). From Paranal Observatory, the south celestial pole lies at a zenith angle of 65° (airmass of 2.4). Unless we build facilities further north or south, or at the poles, the high airmass makes it difficult to achieve the signal-to-noise required. In addition, the atmospheric dispersion correction (ADC) is difficult at these high air masses, and many spectrographs do not have an ADC that can reach 60°. For example, 4MOST corrects only up to 55° zenith angle (de Jong et al. 2019). The absence of legacy data for circumpolar fields presents a further challenge. Our

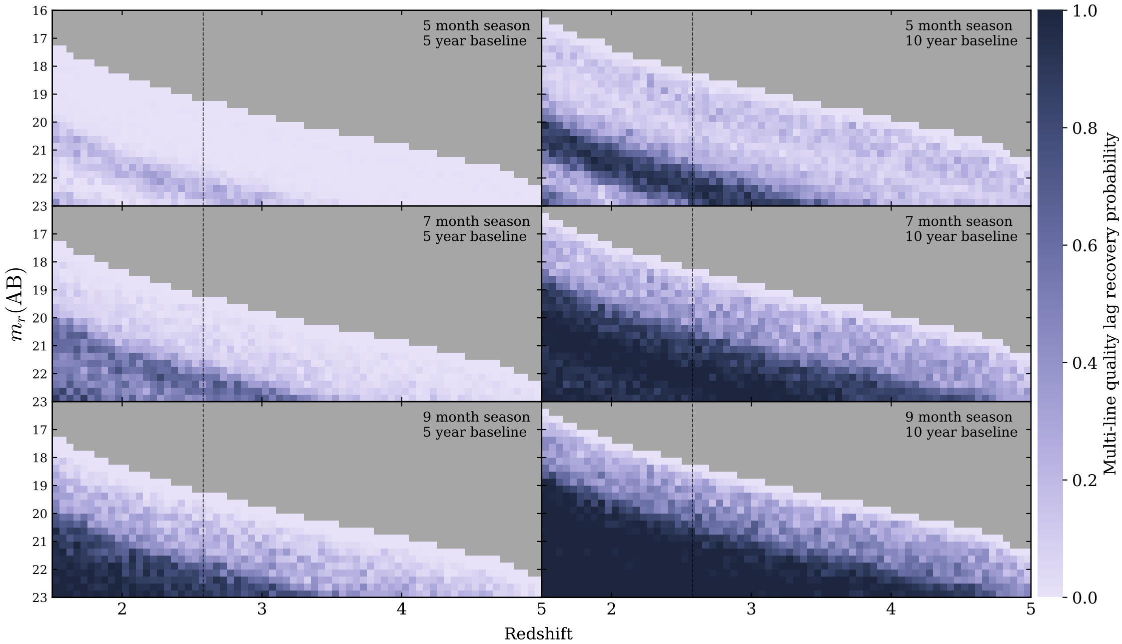

Figure 2.14: Probability of quality lag recoveries made with both emission lines, for each window function. This was generated by multiplying the visibility maps shown in Figures 2.11 and 2.12. The vertical black lines indicate the maximum redshift range over which either Hβ or Mg II can be seen at visible wavelengths ($0 < z \lesssim 2.65$). With infrared capabilities, Hβ can be observed up to z ~2.5, and Mg II to $z = 5$ (as shown in Figure 2.10); therefore all three lines can be seen from $1.5 < z < 2.5$.

simulations show that 9-month seasons bridge the seasonal gap sufficiently (e.g., Table 2.2: 99.8% quality recoveries for CIV mock sample with 10 year baseline and 9 month season), meaning no source is critically dependent on closing the remaining gap of three months.

- *Recovering the $R - L$ relation:* Optimising surveys ultimately depends on the science goals. For RM studies this would be not only to recover as many lags as possible for a sample, but also to ensure measurements are made across a range of luminosity, to anchor both ends of the $R - L$ relationship, for each line. The lower luminosity ends of the relations for Mg II and C IV still lack measurements, as the expected observed-frame lags are short. The window functions of recent surveys have not been optimised to recover these short lags. As shown in Figure 2.13, the baseline length is important for this, particularly when seasonal gaps are present.

- *Multi-line measurements:* Other science goals include recovering lags for multiple emission lines, to study the ionisation stratification of the BLR (Dietrich et al. 1993; Peterson & Horne 2004). Considering the banding structure we see in the visibility maps (Figures 2.10-2.12) when there are significant seasonal gaps, we need to see if there are regions of the parameter space that have high likelihood of lag recovery while two (or more) lines are visible. As Hβ and Mg II have similar expected lags, the bands of high efficacy overlap for redshift regions where both lines can be seen. However for Mg II and C IV, although both lines can be seen over a wider range in redshift (Figure 2.10), there is less overlap between the bands of high efficacy on the visibility maps. The visibility map showing the probability of quality lag recoveries with both lines is shown in Figure 2.14, for each window function. For Mg II and C IV, the number of redshift-luminosity bins with a high probability of providing multi-line measurements greatly increases with near-IR coverage.

2.4.2 Comparing to data

We compare the results of these simulations to recent lag recoveries from the pioneering 'industrial-scale' OzDES and SDSS-RM surveys (Grier et al. 2017; Hoormann et al. 2019; Grier et al. 2019; Homayouni et al. 2020; Yu et al. 2021). In Figure 2.15, the sources with published high-quality lags from OzDES and SDSS-RM are overlaid on the visibility maps for the respective emission lines. We define a 'visible' sample, as previously done for the mock sample, comprising sources which lay on redshift-luminosity bins with a fraction of quality recoveries ≥ 0.5. The $R - L$ relations recovered using the full and 'visible' published samples are shown in Figure 2.16. A significantly shallower slope for the Mg II $R - L$ relation was found by Homayouni et al. (2020), which they suggest could be attributed to the larger intrinsic scatter in the recovered lags. The 'visible' samples do not have less scatter, although the number of data points is limited. We note that all the published lags were recovered using `JAVELIN` (Zu et al. 2011), which could cause some discrepancy with our predictions, which were performed using ICCF. There are many Mg II and C IV lags that lie in the seasonal gaps. These sources have been observed to vary smoothly on multi-year timescales, allowing the lag to be recovered with little to

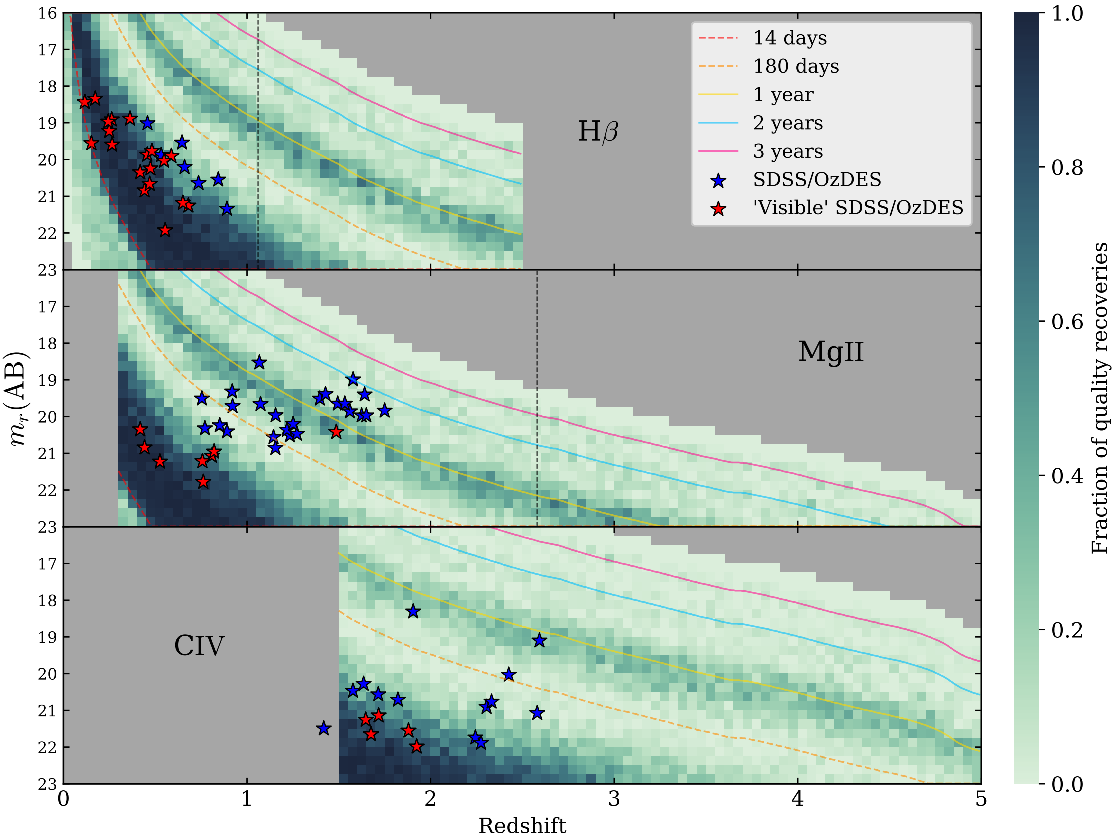

Figure 2.15: Sources with published high quality lag measurements from the OzDES and SDSS-RM surveys (Grier et al. 2017; Hoormann et al. 2019; Grier et al. 2019; Homayouni et al. 2020; Yu et al. 2021) overlaid on the respective visibility map for each emission line. The 'visible' subsample, lying on bins with a fraction of quality recoveries ≥0.5, is in red.

no overlap between the continuum and emission-line light curves. Our use of the DRW light curve model may not appropriately represent this variability over longer timescales. Although the seasonal gap lag recoveries are judged to be reliable, we should expect to see a similar number of recoveries that do lie on regions of high 'visibility', which is not the case for the current sample of Mg II and C IV lags. It is possible that this issue will be alleviated with future results from the longer baseline data from these surveys, which should also help to confirm seasonal gap lags. If the issue remains, it confirms the need for future surveys to ensure the seasonal gaps are reduced as much as possible, to see if this is the cause for the lack of high quality lag measurements from multi-object RM surveys in the regions we predict to be 'visible'.

We acknowledge our simulations are idealised, and the following effects should be

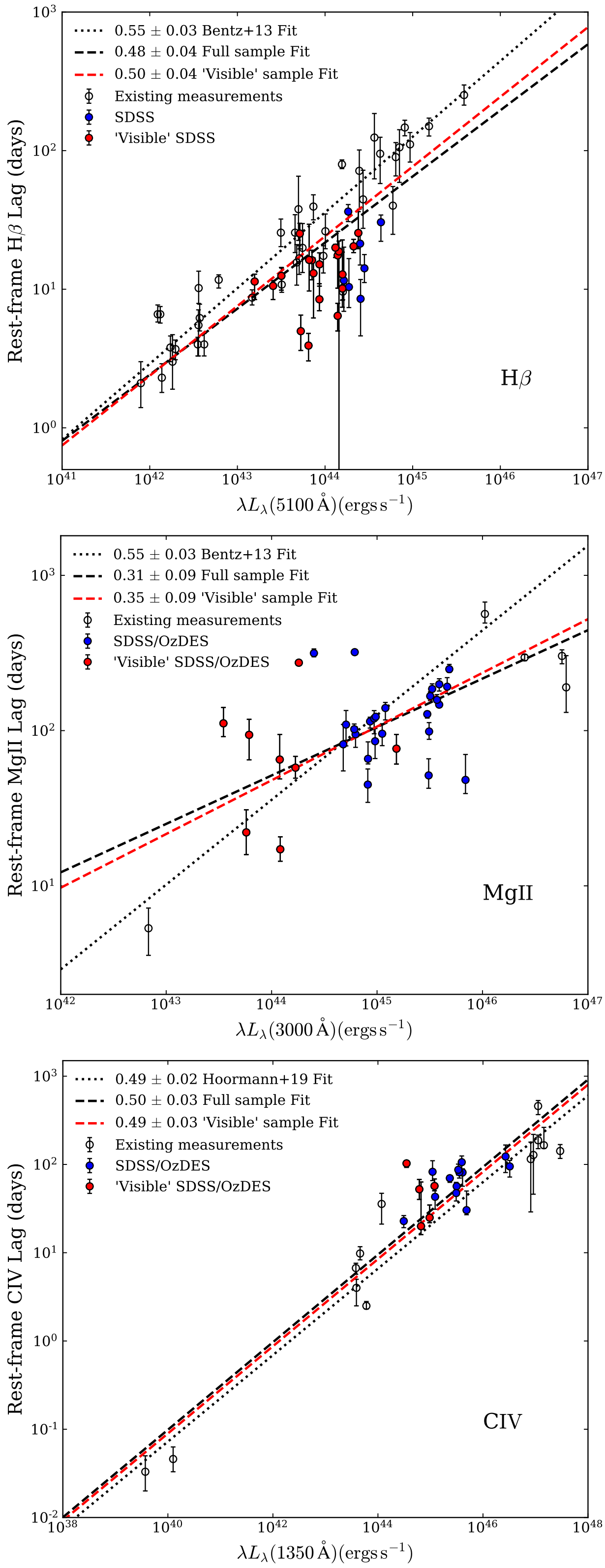

Figure 2.16: The $R - L$ relations constrained using the published high quality lag measurements for each emission line (same as in Figure 2.15), and using only the 'visible' subsample. The existing measurements are also used when constraining the relations. These include measurements from Bentz et al. (2013) (and references therein) for Hβ; Metzroth et al. (2006); Lira et al. (2018); Czerny et al. (2019); Zajaček et al. (2020, 2021) for Mg II; and Peterson et al. (2005) (and references therein); Kaspi et al. (2007); Trevese et al. (2014); Lira et al. (2018) for C IV.

appreciated. The broad-line region emission response has been observed to demonstrate non-reverberating behaviour, such as the BLR 'holiday' (Goad et al. 2016; Dehghanian et al. 2019a). The light curve model we used does not include these deviations, as they are still poorly understood. Recently Stone et al. (2022b) have found that the DRW damping timescale, τ_D, constrained with 20-year light curves, continues to increase as the baseline of the light curves increases. They also observe smooth, long-term variations in some sources, leading them to suggest that the current DRW model may be insufficient for these sources. The significant seasonal gaps in the window function of the data may also preclude proper convergence of the DRW model parameters. A large sample of emission-line light curves is required to better model reverberation in AGN light curves in future work.

2.5 Summary

We present results of comprehensive simulations which demonstrate the impact of each component of the global observational window function on reverberation mapping lag recovery. From individual sources to a population of AGN, we illustrate the detrimental impact of seasonal gaps. Reverberation mapping surveys should prioritise observing fields with longer seasonal visibility, not only to improve lag recovery for more sources, but also to mitigate signal aliasing. We note that seasonal gaps may not affect lag recovery as much for sources with long variability timescales, but long baseline monitoring is required in such cases.

There are complex interactions between the window function, emission-line lag and the relaxation time of the variability, which are further complicated by the redshift time dilation effects. As industrial-scale RM surveys target large AGN samples over wide redshift and luminosity distributions, it will be difficult to find a 'one-size-fits-all' solution to survey design. Careful optimisation of target lists of sources to be monitored will likely deliver significant survey success rates. Future surveys should consider a multi-tiered observing strategy to ensure that the window function is optimised for a more diverse range of sources. Extending the wavelength range of spectrographs to the near-IR will be a critical requirement for joint emission-line lag analyses.

Acknowledgements

We thank the anonymous referee for their comments that improved the paper. UM and AP are supported by the Australian Government Research Training Program (RTP) Scholarship. PM and ZY are supported in part by the United States National Science Foundation under Grant No. 161553 to PM. PM is grateful for support from the Radcliffe Institute for Advanced Study at Harvard University. PM also acknowledges support from the United States Department of Energy, Office of High Energy Physics under Award Number DE-SC-0011726. TMD and JC are supported by an Australian Research Council Laureate Fellowship (project number FL180100168).

We acknowledge parts of this research were carried out on the traditional lands of the Ngunnawal and Ngambri peoples. We pay our respects to their elders past and present.

This analysis used `NumPy` (Harris et al. 2020), `Astropy` (Astropy Collaboration et al. 2013, 2018), `SciPy` (Virtanen et al. 2020), and `thorsky` (`https://github.com/jrthorstensen/thorsky`). Plots were made using `matplotlib` (Hunter 2007) and `seaborn` (Waskom 2021). This work has made use of the SAO/NASA Astrophysics Data System Bibliographic Services.

3

OzDES Reverberation Mapping Program: Hβ lags from the 6-year survey

This chapter is published in the Monthly Notices of the Royal Astronomical Society as: **Malik, U.**, Sharp, R.; Penton, A.; Yu, Z.; Martini, P.; Lidman, C.; Tucker, B. E.; Davis, T. M.; Lewis, G. F.; Aguena, M.; Allam, S.; Alves, O.; Andrade-Oliveira, F.; Asorey, J.; Bacon, D.; Bertin, E.; Bocquet, S.; Brooks, D.; Burke, D. L.; Carnero Rosell, A.; Carollo, D.; Carrasco Kind, M.; Carretero, J.; Costanzi, M.; da Costa, L. N.; Pereira, M. E. S.; De Vicente, J.; Desai, S.; Diehl, H. T.; Doel, P.; Everett, S.; Ferrero, I.; Frieman, J.; García-Bellido, J.; Gerdes, D. W.; Gruen, D.; Gruendl, R. A.; Gschwend, J.; Hinton, S. R.; Hollowood, D. L.; Honscheid, K.; James, D. J.; Kuehn, K.; Marshall, J. L.; Mena-Fernández, J.; Menanteau, F.; Miquel, R.; Ogando, R. L. C.; Palmese, A.; Paz-Chinchón, F.; Pieres, A.; Plazas Malagón, A. A.; Raveri, M.; Rodriguez-Monroy, M.; Romer, A. K.; Sanchez, E.; Scarpine, V.;

Sevilla-Noarbe, I.; Smith, M.; Soares-Santos, M.; Suchyta, E.; Swanson, M. E. C.; Tarle, G.; Taylor, G.; Tucker, D. L.; Weaverdyck, N.; Wilkinson, R. D.; *OzDES Reverberation Mapping Program: Hβ lags from the 6-year survey*, 2023, MNRAS, 520, 2009.

Abstract

Reverberation mapping measurements have been used to constrain the relationship between the size of the broad-line region and luminosity of active galactic nuclei (AGN). This $R-L$ relation is used to estimate single-epoch virial black hole masses, and has been proposed for use to standardise AGN to determine cosmological distances. We present reverberation measurements made with Hβ from the six-year Australian Dark Energy Survey (OzDES) Reverberation Mapping Program. We successfully recover reverberation lags for eight AGN at $0.12 < z < 0.71$, probing higher redshifts than the bulk of Hβ measurements made to date. Our fit to the $R-L$ relation has a slope of $\alpha = 0.41 \pm 0.03$ and an intrinsic scatter of $\sigma = 0.23 \pm 0.02$ dex. The results from our multi-object spectroscopic survey are consistent with previous measurements made by dedicated source-by-source campaigns, and with the observed dependence on accretion rate. Future surveys, including LSST, TiDES and SDSS-V, which will be revisiting some of our observed fields, will be able to build on the results of our first-generation multi-object reverberation mapping survey.

3.1 Introduction

Reverberation Mapping (RM) has been established as the leading technique for direct determination of black hole masses (M_{BH}) in active galactic nuclei (AGN) outside of the local Universe. Reverberation measurements anchor the scaling relations used to estimate single-epoch virial BH masses (Vestergaard 2002; Vestergaard & Peterson 2006). Over the past decade, RM programs conducted by the Australian Dark Energy Survey (OzDES) and Sloan Digital Sky Survey (SDSS) have leveraged high-multiplexed spectroscopy to perform RM on an 'industrial' scale, aiming to increase the number of measurements available by an order of magnitude (King et al.

2015; Shen et al. 2015). These programs have resulted in over one hundred new lag measurements, while also identifying and addressing the complexities of performing RM on such large scales.

As reverberation mapping resolves the innermost regions of AGN in the time-domain, rather than spatially, it allows the study of these regions out to high red-shifts. RM utilises the difference in the light travel time between the variation of the continuum emission from the accretion disk around the central supermassive black hole (SMBH) and the reprocessed emission from the photoionised broad-line region (BLR) (Blandford & McKee 1982; Peterson 1993). The time-delay, τ, can be measured using multi-epoch photometry and spectroscopy to probe the continuum and BLR response respectively in order to infer the radius of the BLR ($R_{\rm BLR} = c\tau$). Together with the BLR velocity dispersion, ΔV^2, inferred from the width of the emission line, this can be used to estimate the mass of the SMBH using the virial product:

$$M_{\rm BH} = f \frac{R_{\rm BLR}\Delta V^2}{G} \tag{3.1}$$

The geometry, orientation, and kinematics of the BLR are encapsulated by the dimensionless scale factor f, which is calibrated using sources with independent measurements from RM and the $M_{\rm BH} - \sigma_*$ relation (Ferrarese & Merritt 2000; Gebhardt et al. 2000a; Onken et al. 2004; Woo et al. 2015).

Due to the intensity of observational resources required, early programs targeted a small number of local AGN with campaign durations of less than one year. To achieve the fidelity required for RM, they observed bright, highly varying AGN. As a result, the targeted samples are typically biased towards AGN in the local Universe ($z < 0.3$). Lag measurements were made for 63 AGN with the Hβ line (e.g., Peterson et al. 1998; Kaspi et al. 2000; Peterson & Horne 2004; Bentz et al. 2009). These measurements were used to constrain the relationship between the AGN luminosity and the radius of the BLR ($R - L$ relation), which exhibited relatively low intrinsic scatter, with a slope consistent with that expected by photoionisation physics (Bentz et al. 2009, 2013). This relation calibrates secondary mass-scaling relations used to estimate single-epoch virial BH masses for samples of thousands of AGN (e.g. SDSS DR7 quasar catalogue, Shen et al. 2011). The $R-L$ relation has also been proposed as a way to standardise AGN for use as luminosity distance indicators for cosmology (Watson et al. 2011; Martínez-Aldama et al. 2019; Khadka et al. 2022).

These BH mass estimates have a significant $\sim$0.5 dex uncertainty, due to our limited understanding of BLR geometry and kinematics and the small sample of reverberation measurements, among other factors (Shen 2013). The former issue is addressed by conducting observationally intensive velocity-resolved RM (e.g. Bentz et al. 2010; Grier et al. 2013a; Pancoast et al. 2014b; Du et al. 2018; U et al. 2022), and using dynamical modelling methods (e.g. CARAMEL, Pancoast et al. 2014a); as well as spectroastrometry of the BLR in local AGN (e.g. GRAVITY, Gravity Collaboration et al. 2018). Other programs are targeting a more diverse range of sources. The super-Eddington accreting massive black holes (SEAMBH) program has observed over 40 luminous AGN (Du et al. 2014; Wang et al. 2014a; Du et al. 2015, 2016, 2018; Hu et al. 2021). The updated $R-L$ relation using these Hβ measurements has increased intrinsic scatter, and an observed dependence on accretion rate. However, these programs are still only targeting AGN at $z < 0.4$.

The SDSS-RM Project and our OzDES-RM Program have pioneered RM on an 'industrial-scale', observing hundreds of AGN probing a wide range of AGN luminosities and redshifts. These programs have added over 100 new lag measurements, and have enabled the Mg II and C IV $R-L$ relations to be constrained with statistically significant samples (Grier et al. 2017; Hoormann et al. 2019; Grier et al. 2019; Homayouni et al. 2020; Yu et al. 2021, 2023, Penton et al. in prep). The first generation of multi-object RM surveys have however highlighted problems with monitoring hundreds of targets. This includes challenges both with data quality (signal-to-noise, limited temporal coverage; Malik et al. 2022) as well as with reverberation lag recovery techniques and biases such as aliasing (Li et al. 2019; Penton et al. 2022).

OzDES focused mainly on high redshift AGN; however, about 10% of the sample contains Hβ emission within the spectroscopic window. This will allow comparison of our OzDES measurements with the large sample of existing Hβ measurements, in order to examine the consistency of multi-object RM with earlier dedicated source-by-source observations. We present the Hβ lag results from our 6-year survey.

Section 3.2 details the observations obtained by OzDES and the data calibration procedures. In Section 3.3 we describe the techniques we used for lag recovery and the selection criteria we apply to define our final sample. In Section 3.4 we present our successful lag measurements and black hole masses, as well as an updated $R-L$ relationship, and discuss these results in Section 3.5. We summarize our results and then present an outlook for the future work in Section 3.6. Throughout this work we adopt a flat ΛCDM cosmology, with $\Omega_\Lambda = 0.7$, $\Omega_M = 0.3$, and $H_0 = 70$ $\mathrm{km\,s^{-1}\,Mpc^{-1}}$.

3.2 Data

The Australian Dark Energy Survey (OzDES) provided follow-up spectroscopic observations of the 10 supernova fields observed by the Dark Energy Survey (DES). The DES supernova fields are located in the ELAIS, XMM-Large Scale Structure, Chandra deep-field South, and SDSS Stripe 82 regions (Kessler et al. 2015; Morganson et al. 2018). These fields were observed in the *griz* filters with the Dark Energy Camera (DECam) on the 4-metre Blanco telescope at Cerro Tololo Inter-American Observatory (CTIO) (Flaugher et al. 2015). From 2013 to early 2018, the fields were observed with ∼6 day cadence over a 5-6 month season (August to January), with additional science verification data taken in late 2012 to early 2013, and additional data taken on a monthly cadence in late 2018. OzDES conducted follow-up multi-object spectroscopic observations with the 2dF multi-object fibre positioning system and the AAOmega spectrograph (3700-8800 Å, Sharp et al. 2006) on the 3.9-metre Anglo-Australian Telescope (AAT) (Yuan et al. 2015; Childress et al. 2017; Lidman et al. 2020). The OzDES observations were made over the same 5-6 month season with approximately monthly cadence from 2013 to 2019.

3.2.1 Target sample

After completing the final data reduction for our survey, the OzDES RM Program sample comprises 735 AGN (reduced from an initial sample of 771 due to a change in the location of the DECam inter-chip gaps between survey definition and campaign observations), with redshifts ranging up to $z \sim 4$, and with apparent magnitudes

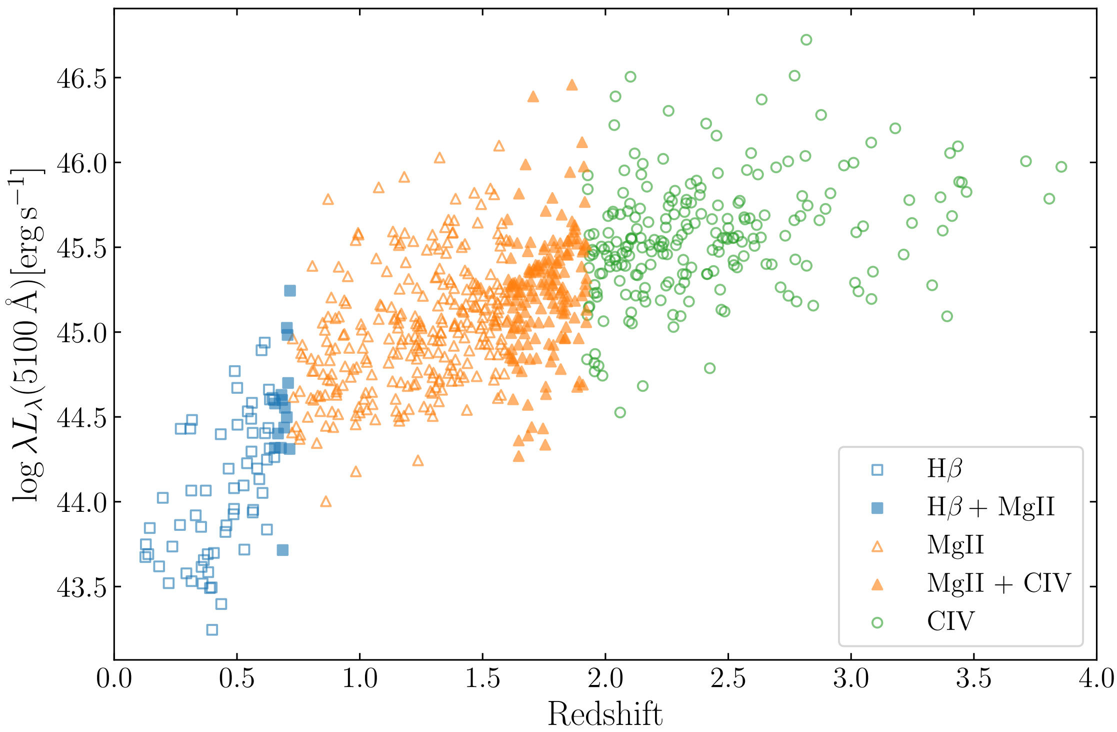

Figure 3.1: Distribution of redshifts and monochromatic luminosities at 5100 Å for the 735 AGN in the OzDES RM sample. The Hβ sample extends to $z = 0.75$, with 15 sources overlapping with our Mg II sample.

$17.2 < r_{\rm AB} < 22.3$ mag. The redshift and luminosity distribution of these AGN is shown in Figure 3.1.

Of these 735 AGN, the Hβ line and nearby continuum falls within the AAOmega spectral range for 78 sources. The expected observer-frame lags for the Hβ sample (governed by luminosity and time-dilation) range from ∼20 days to just over 200 days. In previous analyses, our emission-line flux measurements were made using spectra that were co-added by observing run (Hoormann et al. 2019) (typically 4-7 days during dark time each month). However, some fields were observed over multiple nights within a single observing run. To maximise the cadence of our sampling we treated the spectra obtained on different nights as separate epochs for our emission-line light curves. This is particularly valuable for rapidly reverberating sources. The redshift and luminosity range of our Hβ sample, and Hβ measurements from the literature are shown in Figure 3.2.

We do not measure the continuum luminosity directly from the spectra due to fibre aperture effects from variable atmospheric seeing and fibre placement uncertainties.

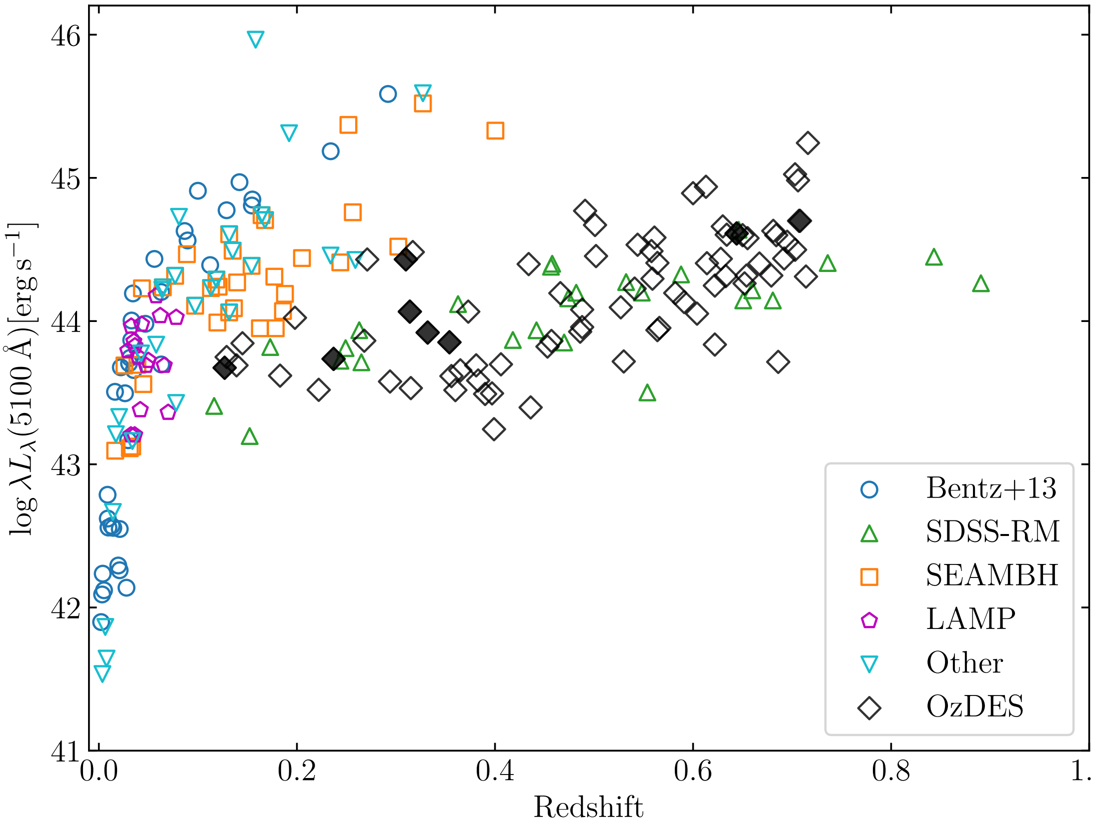

Figure 3.2: The redshift and luminosity distribution for the OzDES Hβ sample (open diamonds), final sample (filled diamonds, see §3.4), and existing measurements from Bentz et al. (2013, and references therein); SDSS-RM (Grier et al. 2017, quality 4 and 5); SEAMBH (Du et al. 2014; Wang et al. 2014a; Du et al. 2015, 2016, 2018; Hu et al. 2021); Lick AGN Monitoring Project (LAMP, U et al. 2022); and other measurements from Bentz et al. (2009); Barth et al. (2013); Bentz et al. (2014); Pei et al. (2014); Lu et al. (2016); Bentz et al. (2016a,b); Fausnaugh et al. (2017); Zhang et al. (2019); Rakshit et al. (2019); Li et al. (2021), of which measurements published before 2019 are compiled by Martínez-Aldama et al. (2019).

From the average r-band magnitude and redshift of the AGN, we estimated the monochromatic continuum flux at 5100 Å using the DECam r-band filter transmission curve and the SDSS quasar template (Vanden Berk et al. 2001). The template is scaled to the magnitude of the source, assuming $L_{\rm bol} = 9\,\lambda L_\lambda\,(5100\,\text{Å})$ (Kaspi et al. 2000).

3.2.2 Flux calibration and measurements

The DES photometry is calibrated consistently through to Y6 using the DES data reduction pipeline (Morganson et al. 2018; Burke et al. 2018). We perform a spectrophotometric flux calibration and line flux measurement following Hoormann et al.

(2019). The local continuum windows for continuum subtraction are 4760 to 4790 Å and 5100 to 5130 Å. The calibration uncertainties of the line flux were measured using the F-star warping function method as detailed in Yu et al. (2021).

3.3 Lag recovery and reliability

3.3.1 Time series analysis

To measure the reverberation lags for our sample we use the interpolated cross-correlation function (ICCF; Gaskell & Peterson 1987) and JAVELIN (Zu et al. 2011, 2013) methodologies. The JAVELIN method models the AGN continuum variability using a damped random walk (DRW; Kelly et al. 2009; Kozłowski et al. 2010; MacLeod et al. 2010). It assumes the emission-line light curve is a scaled, smoothed and shifted version of the continuum light curve, that can be described by the convolution of the continuum with a top-hat transfer function. Using Markov Chain Monte Carlo (MCMC), it constrains the characteristic variability amplitude and damping timescale of the continuum light curve. Applying this DRW fit as a prior, it simultaneously fits both the continuum and emission-line light curves, to derive the posterior distributions of the transfer function parameters: lag, top-hat width and scale factor, as well as an updated DRW amplitude and timescale. We allow these parameters to vary freely, while setting a lag prior of [-$3\tau_{\rm exp}, 3\tau_{\rm exp}$], where $\tau_{\rm exp}$ is the expected Hβ lag for the source using the Bentz et al. (2013) $R-L$ relation.

We use the PyCCF code to perform the ICCF method (Sun et al. 2018). This linearly interpolates the continuum and emission-line light curves over a user defined grid spacing, and cross-correlates the interpolated light curves as a function of time-lag. The centroid of the cross-correlation function (CCF) is computed as the median of the CCF values $> 0.8r_{\rm max}$ counted out from the peak of the CCF, $r_{\rm max}$. A cross-correlation centroid distribution (CCCD) is obtained from 10,000 Monte Carlo realisations of the flux randomisation and random subset sampling (FR/RSS) process (Peterson et al. 1998), which accounts for the flux measurement uncertainties and potentially spurious correlations between light curve points. Following Hoormann et al. (2019), we set the interpolation grid spacing to 3 days, and the $r_{\rm max}$

threshold to 0.5. We use the same lag prior as for JAVELIN, from [-$3\tau_{\rm exp}, 3\tau_{\rm exp}$].

The recovered lag, τ, with lower and upper uncertainties, σ_τ, are taken to be median and 16th and 84th percentiles of the lag probability distribution functions (PDF) from JAVELIN and PyCCF.

3.3.2 Null hypothesis test

Our survey window function for the (expected) short Hβ lags is less than ideal and the signal-to-noise of the spectroscopy is only modest. We wish to test the null hypothesis that our lag recovery is not simply a product of the interaction of the window function with underlying red-noise correlation in the photometric light curves (an underlying assumption of any RM technique). Therefore, we do not report extensive light curve simulations of the Hβ sample (as per U et al. 2022), as this would simply reuse the same window function properties with the added uncertainty of the appropriateness of the variability model for our sources. Instead we randomised the spectroscopic light curves (with flux values shuffled while retaining the dates of observation), and cross correlated this with the original photometric light curve. We find the $r_{\rm max}$ value of the cross correlation coefficient r at the peak of the CCF, and compare it to that found from the CCF of the original light curves. After 1000 iterations, the p-value was calculated as the fraction of $r_{\rm max}$ values which exceeded the original $r_{\rm max}$.

By randomising the emission-line light curves we generate uncorrelated light curves that do not posses a reverberation signature. We chose to randomise the observed spectroscopic light curve, rather than using simulated light curve realisations, as done by U et al. (2022). Simulated light curve realisations have the same variability timescale and underlying lag as the source, and therefore may result in significant spurious correlations at random lag values.

Figure 3.3 shows the results of this test applied to each of the Hβ sources. We see that below a $r_{\rm max}$ of 0.6, there are always a significant number of uncorrelated signals which exceed this $r_{\rm max}$, resulting in high p-values. Therefore we can not trust a result which has a $r_{\rm max}$ below 0.6.

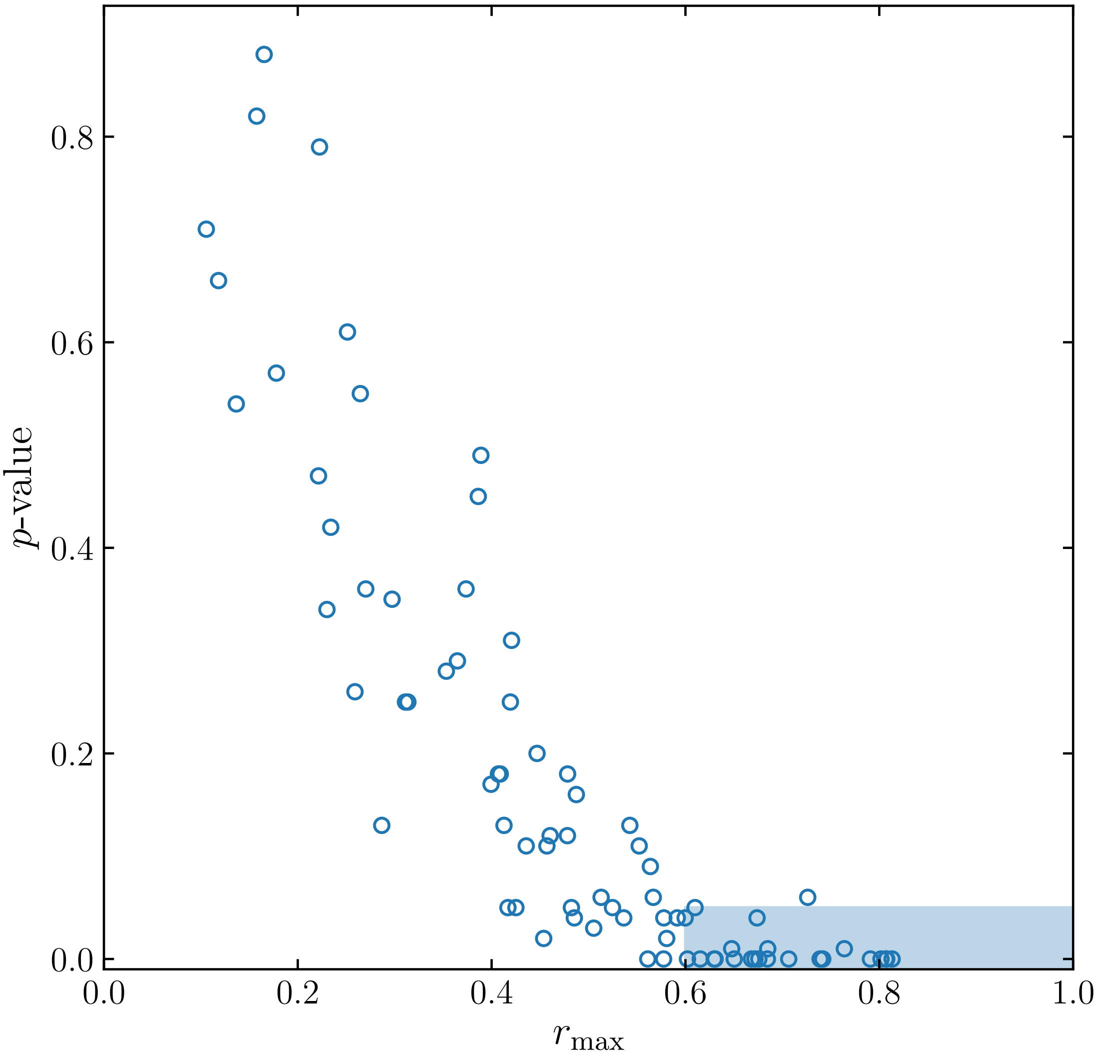

Figure 3.3: p-value vs. $r_{\max}$ for our 78 AGN. The $r_{\max}$ is of the original pair of light curves. The shaded region indicates our selection criteria requiring a p-value < 0.05 and $r_{\max} > 0.6$.

3.3.3 Selection criteria

Based on the results of simulations from Li et al. (2019), Yu et al. (2020b) and Penton et al. (2022), we adopt the lag and uncertainties from JAVELIN as the final lag. We define a successful lag recovery as meeting the following criteria:

- The upper and lower lag uncertainties $\sigma_{\tau,\mathrm{JAV}}$ are less than $|\tau_{\mathrm{JAV}}|$, or 30 days, whichever is greater
- τ_{PyCCF} lies within the $2\sigma_{\tau,\mathrm{JAV}}$ uncertainties
- p-value < 0.05 and $r_{\max} > 0.6$

As the expected lags of our sources range from $\sim$20 to 200d, we use a relative rather than absolute cut on the lag uncertainties. We require the lags recovered from JAVELIN and PyCCF to agree in an attempt to exclude cases where PDF's are flat or have significant aliasing peaks. Our p-test and $r_{\rm max}$ criteria ensure there is significant correlation between the light curves that is unlikely to be spurious.

3.4 Results

We successfully measure lags for five Hβ sources with the criteria listed in §3.3.3. The recovered lags are given in Table 3.1. We present the light curves, and the lag distributions for each of the five sources in Figures 3.4 and 3.5. The re-scaled and phase-shifted light curves for each of the sources display visually discernible reverberation. For each source, there is overlap between the phase-shifted light curves. In most cases, the lag PDF's from PyCCF and JAVELIN agree, although there is significant scatter in the PyCCF CCCD's for some sources. However, even for these cases, the JAVELIN lag is well defined, which is consistent with the finding that JAVELIN is better able to recover short lags than PyCCF (Li et al. 2019).

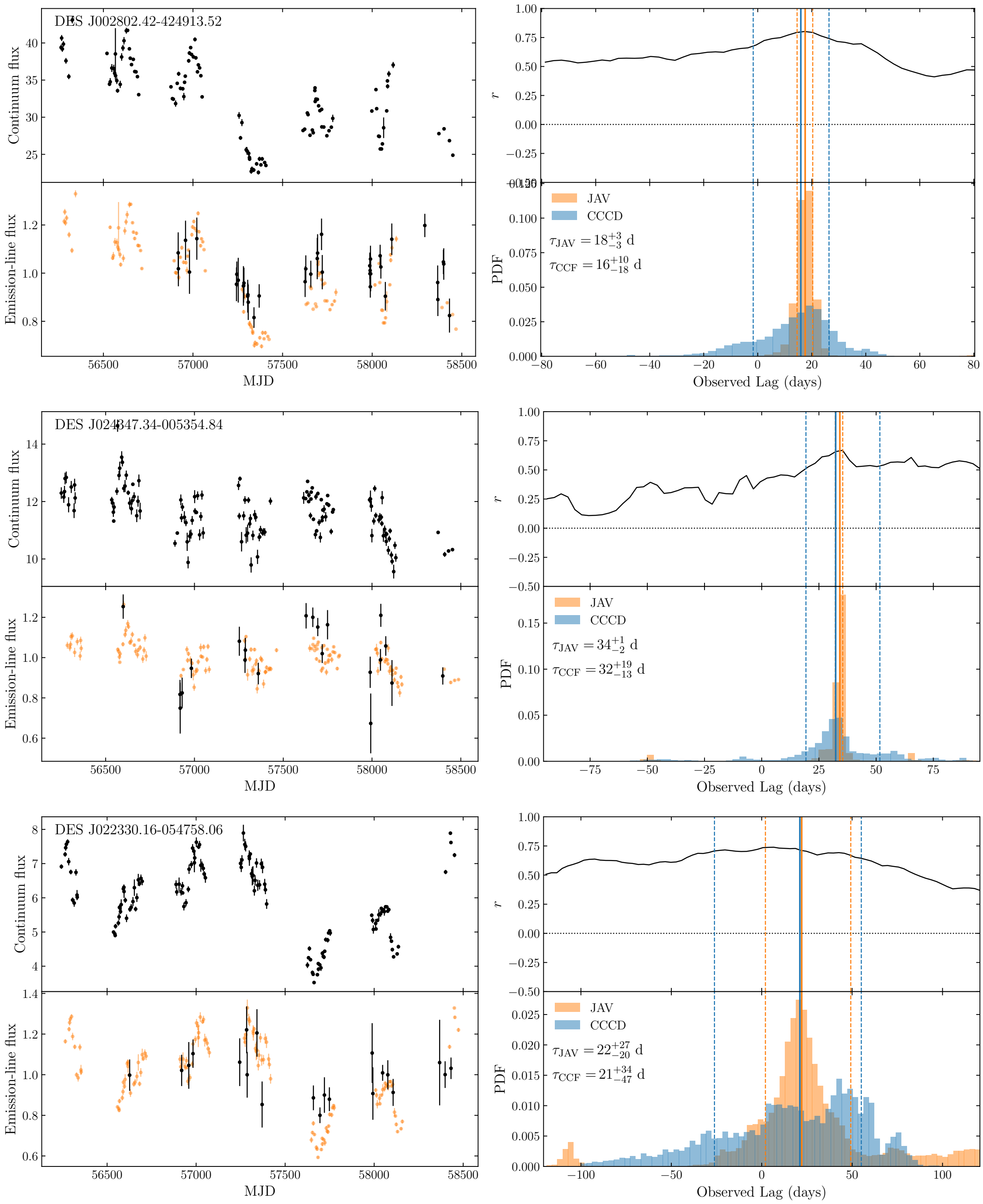

Figure 3.4: For each source, the upper-left panel shows the DECam g-band continuum light curve, and lower-left panel the Hβ emission-line light curve, with the continuum light curve phase-shifted by the `JAVELIN` lag. The fluxes have been re-scaled. The upper-right panel shows the cross-correlation function computed using `PyCCF`. The lower-right panel shows the cross-correlation centroid distribution (CCCD) from `PyCCF` in blue, and the lag posterior from `JAVELIN` in orange, with the vertical solid and dashed lines indicating the recovered lag and upper and lower uncertainties from each method.

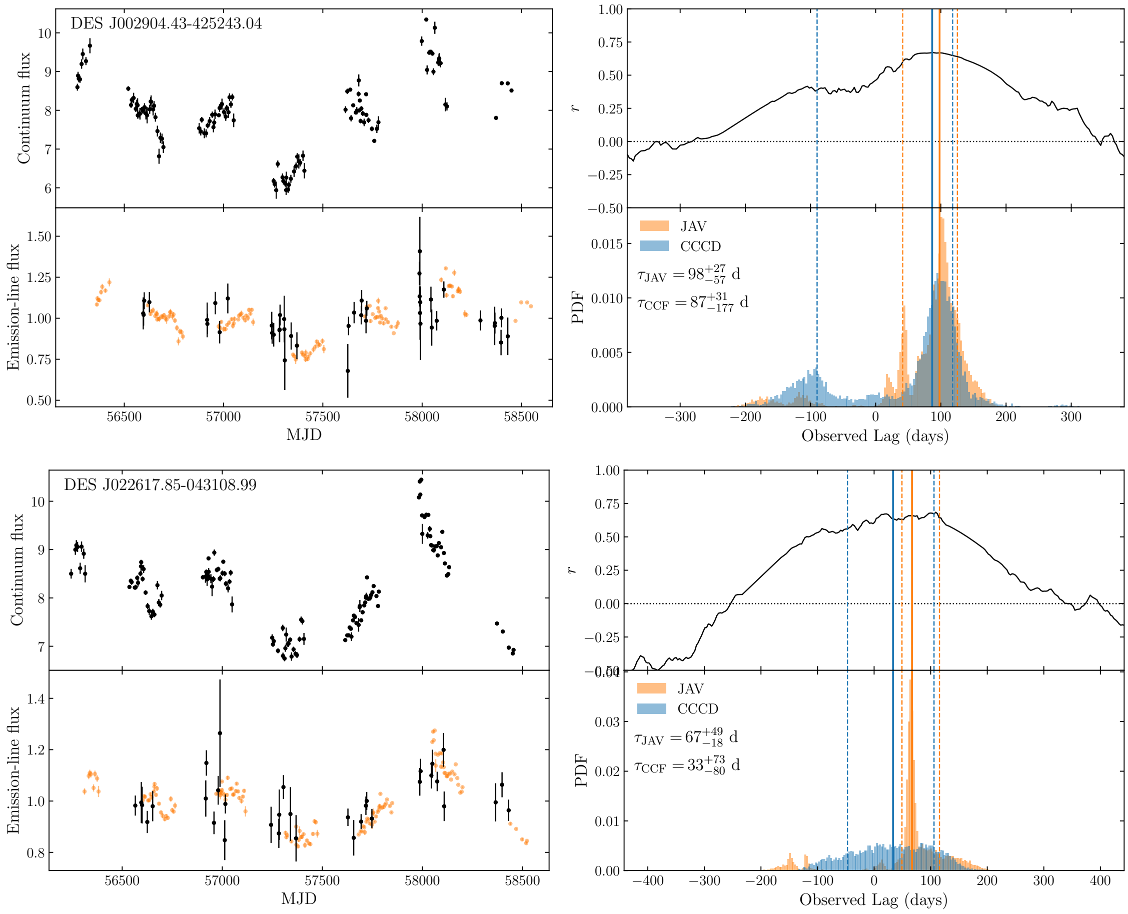

Figure 3.5: Same as for Figure 3.4.

Table 3.1: Results for our final sample of eight AGN. Columns left to right: DES name (J2000), redshift, observer-frame `JAVELIN` lag, observer-frame `PyCCF` lag, p-value, monochromatic luminosity at 5100Å, line dispersion measured from mean spectrum, virial black hole mass, and dimensionless accretion rate.

Source	z	τ_{JAV} (days)	τ_{PyCCF} (days)	p-value	$\log(\lambda L_{5100})$ ($\mathrm{erg\,s^{-1}}$)	σ_{mean} ($\mathrm{km\,s^{-1}}$)	M_{BH} $(\times 10^7 M)$	$\dot{M}$
DES J002802.42-424913.52	0.127	18^{+3}_{-3}	16^{+10}_{-18}	0.000	43.67	1393 ± 3	$2.64^{+0.85}_{-0.87}$	1.43
DES J024347.34-005354.84	0.237	34^{+1}_{-2}	32^{+19}_{-13}	0.000	43.74	1658 ± 6	$6.62^{+1.87}_{-1.89}$	0.28
DES J022330.16-054758.06	0.354	22^{+27}_{-20}	21^{+34}_{-47}	0.002	43.85	1846 ± 11	$4.86^{+6.12}_{-4.62}$	0.79
DES J002904.43-425243.04	0.644	98^{+27}_{-57}	87^{+31}_{-177}	0.002	44.61	1851 ± 4	$17.8^{+7.0}_{-11.4}$	0.80
DES J022617.85-043108.99	0.707	67^{+49}_{-18}	33^{+73}_{-80}	0.006	44.70	1691 ± 8	$9.78^{+7.60}_{-3.76}$	3.63
DES J034028.46-292902.41	0.310	51^{+9}_{-6}	54^{+24}_{-22}	0.002	44.43	1732 ± 5	$10.3^{+3.3}_{-3.1}$	1.30
DES J022249.67-051453.01	0.314	25^{+7}_{-5}	29^{+45}_{-55}	0.005	44.07	1883 ± 5	$5.99^{+2.28}_{-2.00}$	1.08
DES 003954.13-440509.97	0.332	48^{+12}_{-7}	56^{+17}_{-37}	0.001	43.92	1856 ± 11	$10.9^{+4.1}_{-3.4}$	0.20

3.4.1 Additional sources

After visually inspecting the lag recoveries from our full Hβ sample, we identified eight sources with lag PDF's of comparable quality to the sample that passed our selection criteria, but with `JAVELIN` aliasing peaks. This signal is produced as an artefact of the survey window function; predominantly the seasonal gaps. These aliasing peaks do not coincide with a peak in the `PyCCF` CCCD or CCF, and always occur at negative lags coincident with the seasonal gaps in the observational campaign (~ -150 to -250 days). We show the light curves and lag PDF's of these sources in Figures 3.6, 3.7 and 3.8. For most sources, there is good agreement in the light curves phase-shifted by the positive recovered lag. For three of the eight sources (Figure 3.6), there is overlap between the photometric and spectroscopic observations, while the light curves for the other five (Figure 3.7 and Figure 3.8) shift such that the spectroscopic observations fall wholly within gaps in the photometric observations. For comparison, we phase-shifted the continuum light curve by the lag at which the negative `JAVELIN` peak occurs. We show the light curves phase-shifted by both the positive lag and the negative lag in Figure 3.9 and Figure 3.10. In some cases, the light curves show smooth multi-year variations, for which the negatively phase-shifted light curves do seem to reasonably interpolate between the seasonal gaps; however, there is no coincident peak in the `PyCCF` CCCD.

If we omit the negative peaks in the `JAVELIN` PDF's, five of the eight sources pass our selection criteria, and therefore illustrate comparable quality to the sample recovered originally. Given there is no physical motivation for a negative reverberation lag, and the negative aliasing peaks seem to be an artefact of the `JAVELIN` method alone, we choose to include the three sources that demonstrate overlap between their light curves when shifted by the positive lag in our final sample. We provide the lags for these three sources in Table 3.1. At this stage we choose not to include the other two sources, DES J024533.65-000744.91 and DES J004009.06-431255.29, which have positive lags that cause the phase-shifted light curves to land completely within the seasonal gaps. The three sources that do not pass all our selection criteria only fail the r_{max} criterion, although we note that their r_{max} are above 0.5. The phase-shifted light curves for these three sources also fall within the seasonal gaps. High cadence

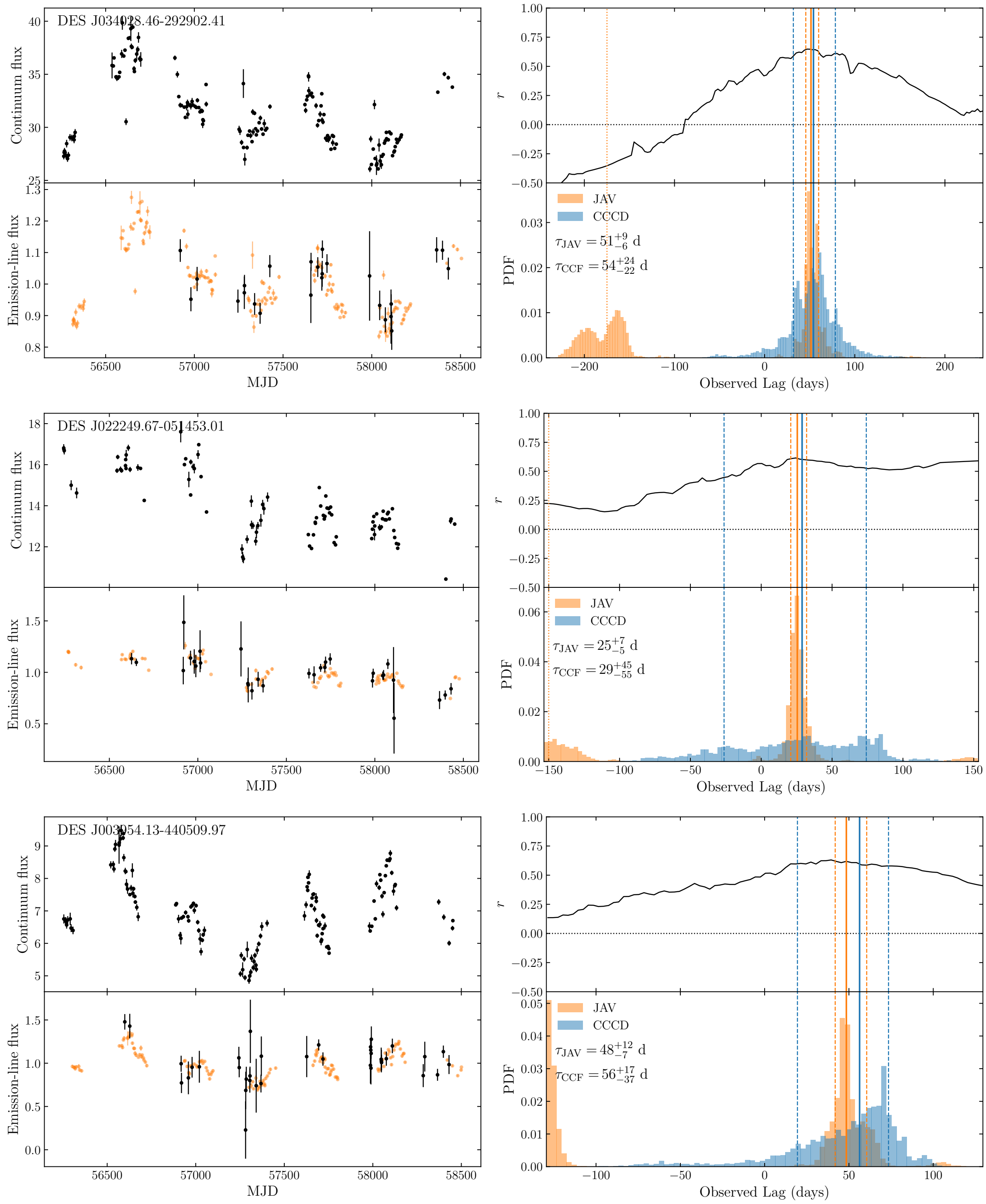

Figure 3.6: Same as for Figure 3.4, for sources with `JAVELIN` aliasing signals. The orange vertical dotted lines indicate the negative aliasing peak in the `JAVELIN` PDF, for which we show the phase shifted light curves in Figure 3.9. These three sources are included in the final sample.

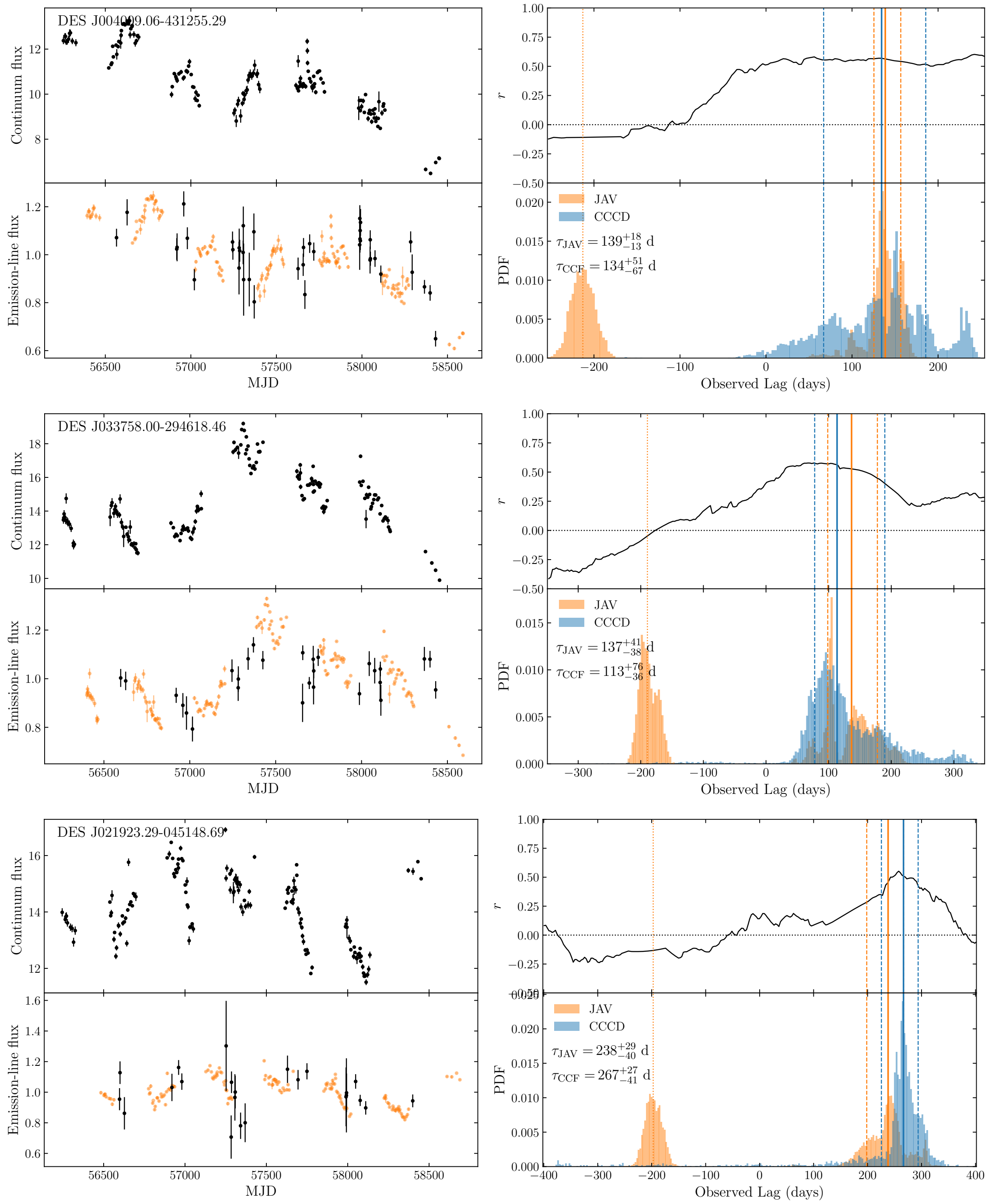

Figure 3.7: Same as for Figure 3.6. These sources are not included in the final sample.

monitoring to resolve shorter term variations, and observing over longer seasons will be required to reliably recover these lags.

Figure 3.2 shows the redshift and luminosity distribution of our final recovered sample of eight AGN, compared with existing measurements. Our sample probes higher redshifts, and spans 1 dex in luminosity.

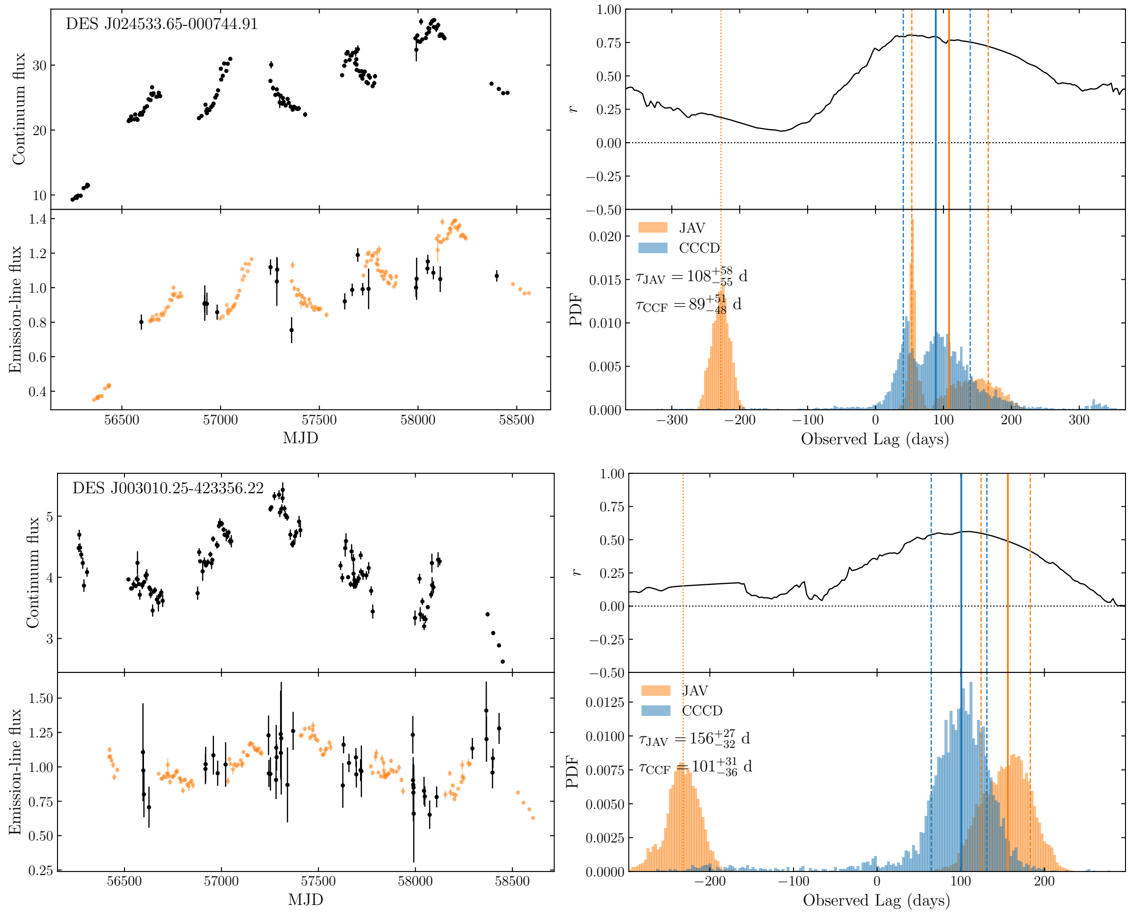

Figure 3.8: Same as for Figure 3.6. These sources are not included in the final sample.

3.4.2 Black hole masses and the $R - L$ relation

We measured the Hβ line-width using the line dispersion of the mean spectra. Although Hβ line-width measurements are commonly made using the root mean squared (rms) spectra, the signal-to-noise of our spectra are insufficient to support this approach. We measure $M_{\rm BH}$ for our final sample of eight AGN using Equation 4.1 and a virial factor $f = 4.47$ (Woo et al. 2015), and give these in Table 3.1, along with the line dispersion measurements.

We constrain the $R-L$ relation as shown in Figure 3.11. Our best fit to the existing data and our final sample is

$$\log(R_{\rm BLR}/{\rm lt-day}) = K + \alpha \log(\lambda L_\lambda)/10^{44}[{\rm erg\,s^{-1}}] \tag{3.2}$$

with slope $\alpha = 0.41 \pm 0.03$, $K = 1.33 \pm 0.02$, and an intrinsic scatter of $\sigma = 0.23 \pm 0.02$ dex.

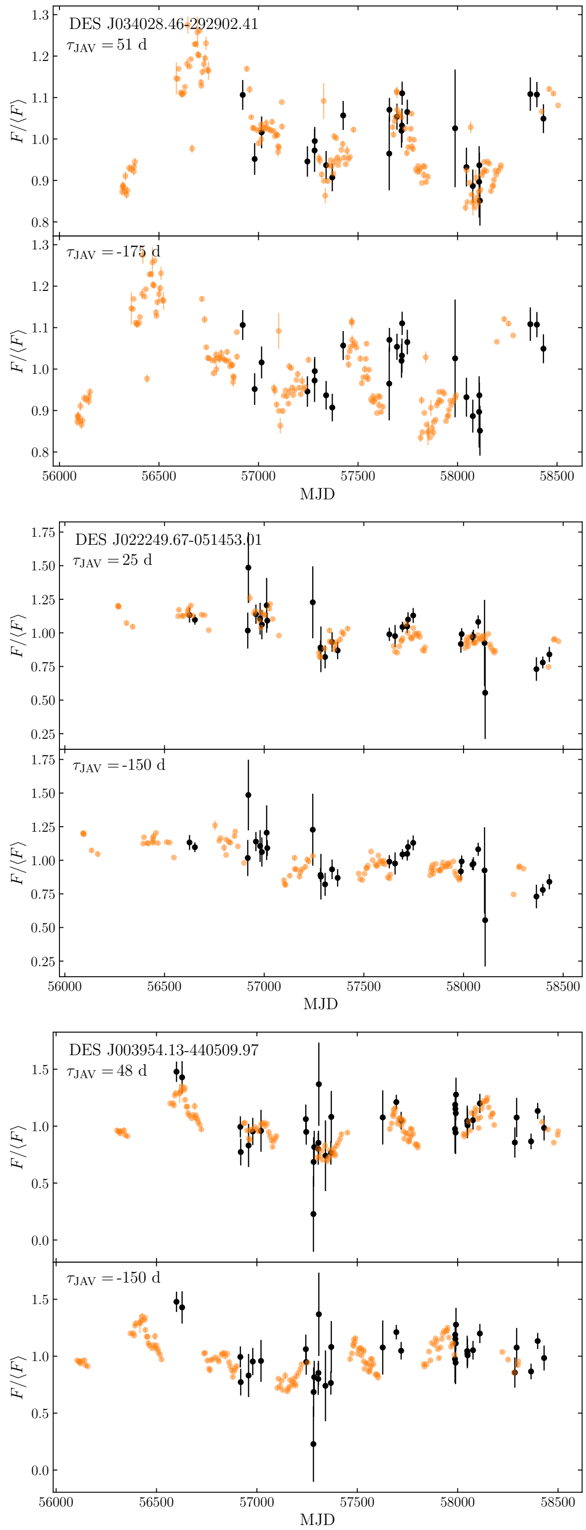

Figure 3.9: The emission-line light curve (black) and phase-shifted continuum light curve (orange) for the additional three sources we include in our final sample. The top and bottom panels show the continuum shifted by the positive and negative lag, respectively. For each source there is overlap between the light curves phase-shifted by the positive lag, while the negative lag shifts the continuum light curves wholly within the seasonal gaps of the emission-line light curve.

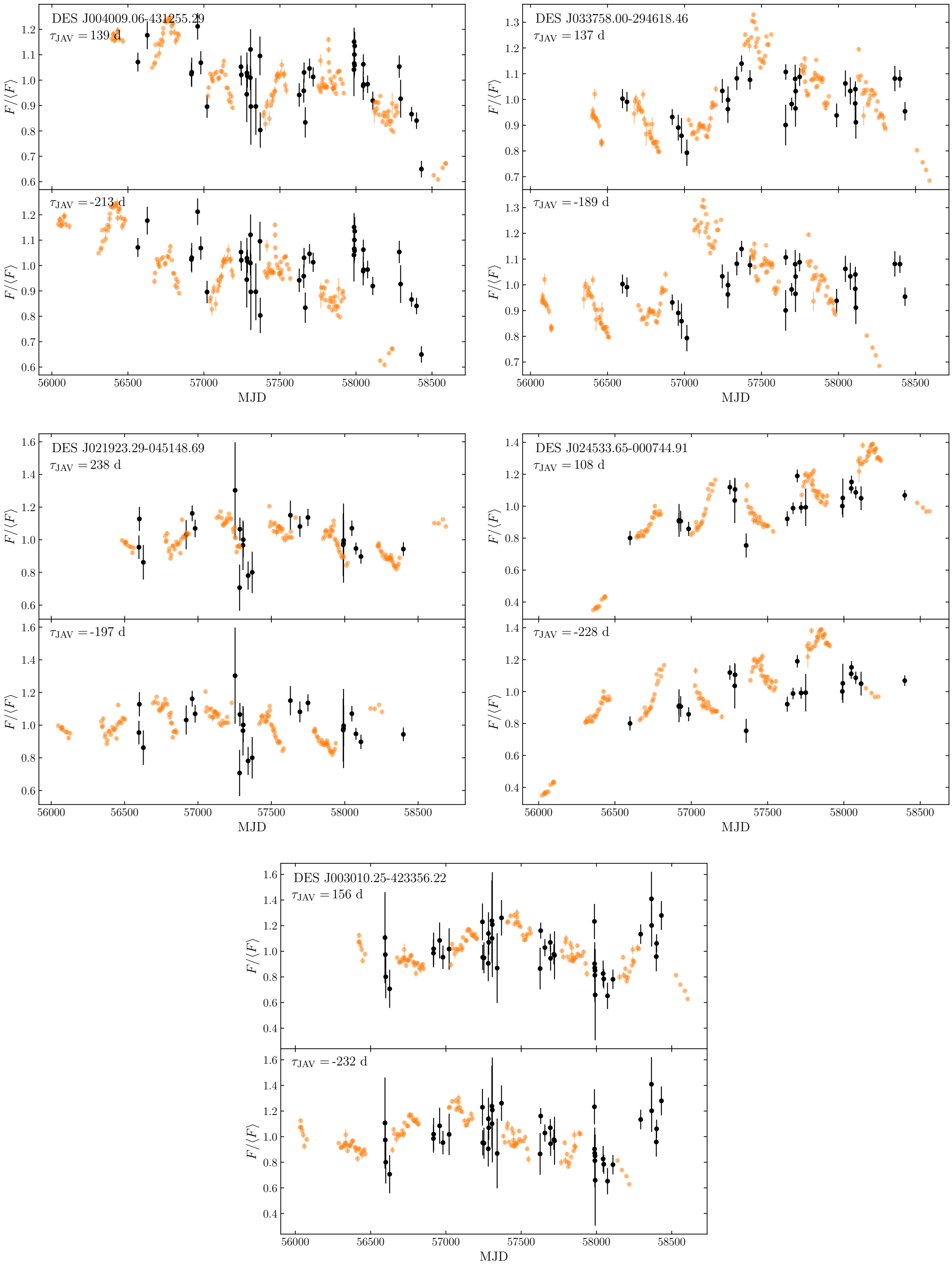

Figure 3.10: The emission-line light curve (black) and phase-shifted continuum light curve (orange) for the five sources in Figure 3.7 and Figure 3.8, which we do not include in our final sample. The top and bottom panels show the continuum shifted by the positive and negative lag, respectively. For each source, in both cases there is no overlap between the photometric and spectroscopic observations.

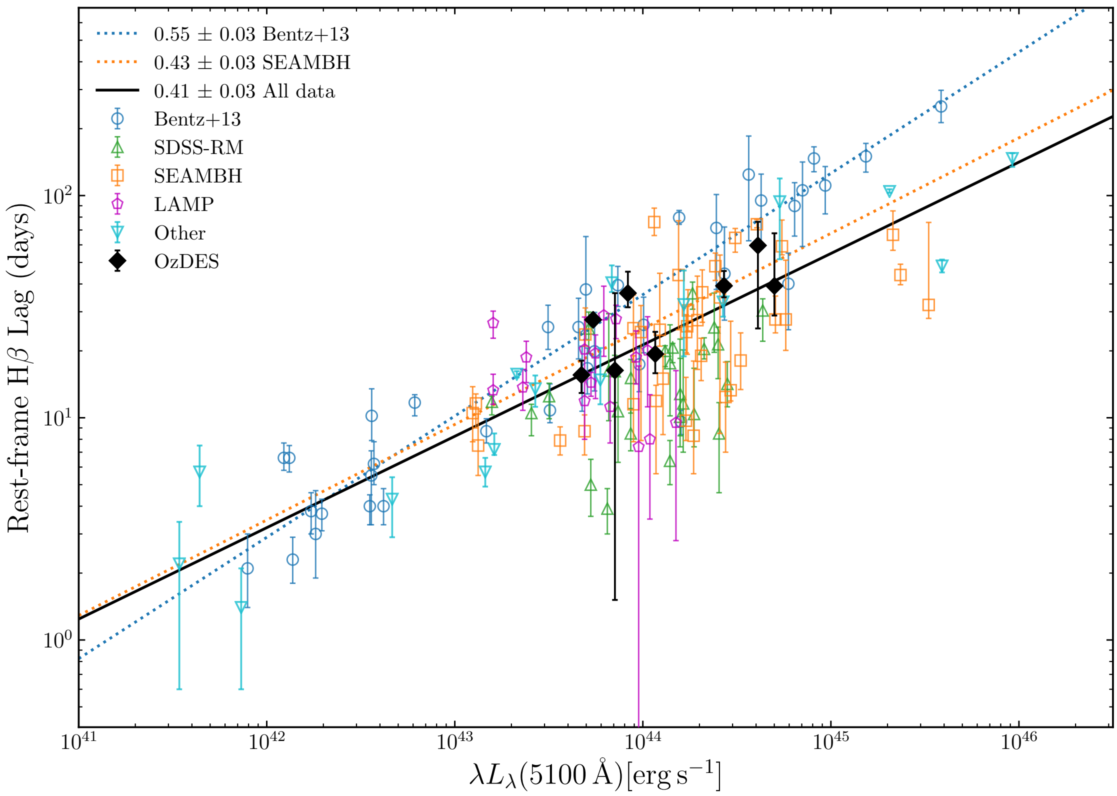

Figure 3.11: Radius-Luminosity relation for Hβ using our final sample of eight new AGN together with existing measurements from Bentz et al. (2013, and references therein); SDSS-RM (Grier et al. 2017, quality 4 and 5); SEAMBH (Du et al. 2014; Wang et al. 2014a; Du et al. 2015, 2016, 2018; Hu et al. 2021); Lick AGN Monitoring Project (LAMP, U et al. 2022); and other measurements from Bentz et al. (2009); Barth et al. (2013); Bentz et al. (2014); Pei et al. (2014); Lu et al. (2016); Bentz et al. (2016a,b); Fausnaugh et al. (2017); Zhang et al. (2019); Rakshit et al. (2019); Li et al. (2021), of which measurements published before 2019 are compiled by Martínez-Aldama et al. (2019). The slope of the relation is given in the legend, along with the slopes constrained previously by Bentz et al. (2013) and Du et al. (2018). All sources in the OzDES sample have low accretion rates, apart from our highest luminosity measurement (right-most black point), which has a moderately high accretion rate (Table 3.1).

The SEAMBH program targeted highly accreting AGN at $z < 0.4$ (Du et al. 2014; Wang et al. 2014a; Du et al. 2015, 2016, 2018; Hu et al. 2021). SEAMBH found that highly accreting AGN have systematically shorter reverberation lags. They proposed that accretion rate explains the observed deviation from the steeper $R-L$ relation from the Bentz et al. (2013) compilation of earlier results. Following Du et al. (2018), we measure the dimensionless accretion rate of our sample using the estimator derived from the standard thin accretion disk model (Shakura & Sunyaev

1973):

$$\dot{M} = 20.1 \left(\frac{l_{44}}{\cos{(i)}}\right)^{3/2} m_7^{-2}, \tag{3.3}$$

where $l_{44} = L_{5100}/10^{44}\ \mathrm{erg\,s^{-1}}$, $m_7 = M_{\rm BH}/10^7$ M, and the inclination angle of the disk to the line of sight is taken to be $\cos(i) = 0.75$. All but one of our sources have low accretion rates, which is consistent with the observed agreement between our results and the Bentz et al. (2013) relation, which was constrained using mainly low-accretion sources. One of our sources is on the lower boundary of what SEAMBH define to be highly accreting, and is consistent with both the low-accretion and high-accretion samples.

3.5 Discussion

The primary goal of the OzDES RM Program was to make RM measurements at high redshifts, with the Mg II and C IV lines. Our monthly cadence was sufficient for this, due to the intrinsically longer reverberation lags for these high ionisation lines, and the increased time dilation for such sources that are typically at higher redshifts than our Hβ sample. Simulations showed the OzDES observational cadence was likely insufficient to provide a full sample of Hβ RM measurements (King et al. 2015; Malik et al. 2022). Since our survey is not as sensitive to these shorter lags, some of our selection criteria are not as strict as other analyses. Some of the uncertainties on the lags we have recovered are considerably larger than previous works, as we lack the temporal resolution to recover lags precisely.

Our new measurements are more consistent with the Bentz et al. (2013) slope than the SDSS-RM Hβ sample (Grier et al. 2017), although our sample has a similar redshift-luminosity distribution to SDSS-RM. As discussed by Grier et al. (2017), the SDSS-RM lags may underestimate $M_{\rm BH}$ due to selection effects from having only a single campaign season of observation which limits the lag search window to 100d. Our OzDES analysis is based on a 7 years of photometry and 6 years of spectroscopy but with lower observational cadence. However, simulations by Fonseca Alvarez et al. (2020) suggest this deviation is not due to observational biases. They attribute the deviation of their sample to changes in the UV/optical spectral energy distribution (SED), although this was not measured directly. The only significant difference between the OzDES and SDSS-RM samples and lag analyses is the baseline and cadence of the light curve data.

Simulations presented by Malik et al. (2022) modelled survey window functions for OzDES and upcoming surveys, and investigated lag recovery efficacy with degraded or increased sampling. They find that with low sampling the scatter in the recovered $R-L$ relation is increased, however there is no systematic offset from the input slope (see Figure 13 in Malik et al. 2022). For sources with shorter expected lags and with a less-than-ideal cadence, they did not systematically recover longer lags. In the case that these idealised simulations are not representative of the data, it is possible that with our cadence we may not be as sensitive to shorter lags if they were present. Upcoming surveys, including the Time-Domain Extragalactic Survey (TiDES; Swann et al. 2019) and SDSS-V Black Hole Mapper (Kollmeier et al. 2017), which will be spectroscopically following up the Legacy Survey of Space and Time (LSST) deep-drilling fields, will be revisiting most of the OzDES fields with shorter spectroscopic cadence. These programs can investigate any potential discrepancies with our results due to the longer cadence of OzDES.

3.6 Summary

We successfully recover reverberation lags with Hβ for eight AGN from the six-year observations from DES and OzDES. These results from our multi-object survey are consistent with previous Hβ analyses done with source-by-source observations, including the early results compiled in Bentz et al. (2013). Our observations seem inconsistent with the large scatter observed in the SDSS-RM Hβ sample (Grier et al. 2017), although the only significant difference between our analyses is the baseline and cadence of the survey data. Our sample includes only one moderately high accretion rate source, and the location of our final sample on the $R-L$ relation is consistent with earlier measurements with similar source accretion rates. This work compliments the higher redshift results for the rest of the OzDES RM sample of 735 AGN, made with the Mg II (Yu et al. 2021, 2023) and C IV lines (Hoormann et al. 2019; Penton et al. 2022, Penton et al. in prep), which will be used to recalibrate black hole mass-scaling relations for those emission lines.

The Hβ sample is highly sensitive to the observational window function. Additional campaign seasons seem to help, but higher cadence and observing over longer seasons is necessary to reliably recover these lags. Future surveys, including TiDES (Swann et al. 2019) and SDSS-V BHM (Kollmeier et al. 2017), which will be following up LSST, will observe some of the same fields as OzDES. These surveys can follow up with a more suitable window function (Malik et al. 2022). In order to anchor the ends of the Hβ $R-L$ relation, future programs will need to target lower luminosity sources at $10^{41} < \lambda L_\lambda\,(5100\,\text{Å}) < 10^{43}$ $\text{ergs}\,\text{s}^{-1}$, and higher luminosity sources at $\lambda L_\lambda\,(5100\,\text{Å}) > 10^{45}$ $\text{ergs}\,\text{s}^{-1}$. The challenge is to have a survey area large enough to observe local sources at low luminosity, and the rare local high luminosity sources. This is especially difficult for multi-object RM surveys, but by extending spectral coverage into the red-optical and infra-red range, such surveys can access the greater volume for such sources at higher redshifts with Hβ.

Acknowledgements

We thank the anonymous referee for their comments that improved the paper. UM and AP are supported by the Australian Government Research Training Program (RTP) Scholarship. PM and ZY were supported in part by the United States National Science Foundation under Grant No. 161553 to PM. PM is grateful for support from the Radcliffe Institute for Advanced Study at Harvard University. PM also acknowledges support from the United States Department of Energy, Office of High Energy Physics under Award Number DE-SC-0011726. TMD is supported by an Australian Research Council Laureate Fellowship (project number FL180100168).

We acknowledge parts of this research were carried out on the traditional lands of the Ngunnawal and Ngambri peoples. This work makes use of data acquired at the Anglo-Australian Telescope, under program A/2013B/012. We acknowledge the Gamilaraay people as the traditional owners of the land on which the AAT stands. We pay our respects to their elders past and present.

This analysis used NumPy (Harris et al. 2020), Astropy (Astropy Collaboration et al. 2013, 2018), and SciPy (Virtanen et al. 2020). Plots were made using Matplotlib (Hunter 2007). This work has made use of the SAO/NASA Astrophysics Data System Bibliographic Services.

This paper has gone through internal review by the DES collaboration. Funding for the DES Projects has been provided by the U.S. Department of Energy, the U.S. National Science Foundation, the Ministry of Science and Education of Spain, the Science and Technology Facilities Council of the United Kingdom, the Higher Education Funding Council for England, the National Center for Supercomputing Applications at the University of Illinois at Urbana-Champaign, the Kavli Institute of Cosmological Physics at the University of Chicago, the Center for Cosmology and Astro-Particle Physics at the Ohio State University, the Mitchell Institute for Fundamental Physics and Astronomy at Texas A&M University, Financiadora de Estudos e Projetos, Fundação Carlos Chagas Filho de Amparo à Pesquisa do Estado do Rio de Janeiro, Conselho Nacional de Desenvolvimento Científico e Tecnológico and the Ministério da Ciência, Tecnologia e Inovação, the Deutsche Forschungsgemeinschaft and the Collaborating Institutions in the Dark Energy Survey.

The Collaborating Institutions are Argonne National Laboratory, the University of California at Santa Cruz, the University of Cambridge, Centro de Investigaciones Energéticas, Medioambientales y Tecnológicas-Madrid, the University of Chicago, University College London, the DES-Brazil Consortium, the University of Edinburgh, the Eidgenössische Technische Hochschule (ETH) Zürich, Fermi National Accelerator Laboratory, the University of Illinois at Urbana-Champaign, the Institut de Ciències de l'Espai (IEEC/CSIC), the Institut de Física d'Altes Energies, Lawrence Berkeley National Laboratory, the Ludwig-Maximilians Universität München and the associated Excellence Cluster Universe, the University of Michigan, NSF's NOIRLab, the University of Nottingham, The Ohio State University, the University of Pennsylvania, the University of Portsmouth, SLAC National Accelerator Laboratory, Stanford University, the University of Sussex, Texas A&M University, and the OzDES Membership Consortium.

Based in part on observations at Cerro Tololo Inter-American Observatory at NSF's NOIRLab (NOIRLab Prop. ID 2012B-0001; PI: J. Frieman), which is managed by the Association of Universities for Research in Astronomy (AURA) under a cooperative agreement with the National Science Foundation.

The DES data management system is supported by the National Science Foundation under Grant Numbers AST-1138766 and AST-1536171. The DES participants from Spanish institutions are partially supported by MICINN under grants ESP2017-89838, PGC2018-094773, PGC2018-102021, SEV-2016-0588, SEV-2016-0597, and MDM-2015-0509, some of which include ERDF funds from the European Union. IFAE is partially funded by the CERCA program of the Generalitat de Catalunya. Research leading to these results has received funding from the European Research Council under the European Union's Seventh Framework Program (FP7/2007-2013) including ERC grant agreements 240672, 291329, and 306478. We acknowledge support from the Brazilian Instituto Nacional de Ciência e Tecnologia (INCT) do e-Universo (CNPq grant 465376/2014-2).

This manuscript has been authored by Fermi Research Alliance, LLC under Contract No. DE-AC02-07CH11359 with the U.S. Department of Energy, Office of Science, Office of High Energy Physics.

4

OzDES Reverberation Mapping Program: Stacking analysis with Hβ, Mg II and C IV

This chapter has been submitted to the Monthly Notices of the Royal Astronomical Society as: **Malik, U.**; Sharp, R.; Penton, A.; Yu, Z.; Martini, P.; Tucker, B. E.; Davis, T. M.; Lewis, G. F.; Lidman, C.; Aguena M.; Alves, O.; Annis, J.; Asorey, J; Bacon, D.; Brooks, D.; Carnero Rosell, A.; Carretero, J.; Cheng, T.-Y.; da Costa, L. N.; Pereira, M. E. S.; De Vicente, J.; Doel, P.; Ferrero, I.; Frieman, J.; Giannini, G.; Gruen, D.; Gruendl, R. A.; Hinton, S. R.; Hollowood, D. L.; James, D. J.; Kuehn, K.; Marshall, J. L.; Mena-Fernández, J.; Menanteau, F.; Miquel, R.; Ogando, R. L. C.; Palmese, A.; Pieres, A.; Plazas Malagón, A. A.; Reil, K.; Romer, A. K.; Sanchez, E.; Schubnell, M.; Smith, M.; Suchyta, E.; Swanson, M. E. C.; Tarle, G.; To, C.; Weaverdyck, N.; Wiseman, P.; *OzDES Reverberation Mapping Program: Stacking analysis with Hβ, Mg* II *and C* IV, in July 2023.

Abstract

Reverberation mapping is the leading technique used to measure direct black hole masses outside of the local Universe. Additionally, reverberation measurements calibrate secondary mass-scaling relations used to estimate single-epoch virial black hole masses. The Australian Dark Energy Survey (OzDES) conducted one of the first multi-object reverberation mapping surveys, monitoring 735 AGN up to $z \sim 4$, over 6 years. The limited temporal coverage of the OzDES data has hindered recovery of individual measurements for some classes of sources, particularly those with shorter reverberation lags or lags that fall within campaign season gaps. To alleviate this limitation, we perform a stacking analysis of the cross-correlation functions of sources with similar intrinsic properties to recover average composite reverberation lags. This analysis leads to the recovery of average lags in each redshift-luminosity bin across our sample. We present the average lags recovered for the Hβ, Mg II and C IV samples, as well as multi-line measurements for redshift bins where two lines are accessible. The stacking analysis is consistent with the Radius-Luminosity relations for each line. Our results for the Hβ sample demonstrate that stacking has the potential to improve upon constraints on the $R-L$ relation, which have been derived only from individual source measurements until now.

4.1 Introduction

Reverberation mapping is a powerful technique that can resolve the cores of active galactic nuclei (AGN) in the time domain. The accretion disk around the central supermassive black hole (SMBH) produces intrinsically variable emission at UV-optical wavelengths. The surrounding broad-line region (BLR) is ionised by this continuum emission, which drives a reverberation response in the emission-line flux from the BLR on time-scales of weeks to months (Blandford & McKee 1982; Peterson 1993). Multi-epoch photometric and spectroscopic observations can be used to trace the variability of the continuum and the emission-line response, respectively.

The size difference between the accretion disk (light-days to weeks) and the BLR (light-weeks to months) introduces a delay in the response of the BLR to the variation in the ionising flux. The delay, *i.e.* reverberation lag, τ, can be recovered by cross-correlating the two light curves, in order to measure the radius of the BLR ($R_{\mathrm{BLR}} = c\tau$). The velocity dispersion of the BLR (ΔV) can be estimated from the width of the broadened emission lines. The mass of the central black hole (M_{BH}) can then be measured using the virial theorem:

$$M_{\mathrm{BH}} = f \frac{R_{\mathrm{BLR}} \Delta V^2}{G}, \tag{4.1}$$

where f is the virial coefficient; a dimensionless scale factor that accounts for the geometry, orientation, and kinematics of the BLR (Woo et al. 2015).

Reverberation mapping (RM) is presently the only method that can be used to directly measure SMBH masses beyond the local Universe, as other techniques are reliant on resolving the gravitational sphere-of-influence of the black hole, which remains challenging even with high angular resolution instruments (e.g., Gebhardt et al. 2000a, 2011; Kuo et al. 2011; Event Horizon Telescope Collaboration et al. 2019). However, RM is by nature observationally intensive. It requires repeated observation over the relevant variability time-scales of AGN in order to ensure the light-curve variability and reverberation lag are resolved (Horne et al. 2004). Early surveys monitored AGN on a source-by-source basis, making observations over several months to years. Lag measurements were made for dozens of sources, using the Hβ line (e.g., Peterson et al. 1998; Kaspi et al. 2000; Peterson & Horne 2004; Bentz et al. 2009). From these measurements, a tight correlation was found between the AGN luminosity and the radius of the BLR ($R - L$ relation; e.g., Bentz et al. 2009, 2013). Lags recovered using higher ionisation emission lines (e.g., C IV) were found to be shorter than lags recovered using lower ionisation emission lines (e.g., Hβ), demonstrating the ionisation stratification of the BLR (Gaskell & Sparke 1986; Dietrich et al. 1993). The $R - L$ relation is importantly used to calibrate secondary mass-scaling relations to estimate single-epoch virial BH masses (e.g., Shen et al. 2011), and has also been proposed as a way to standardise AGN for use as a cosmological distance indicators (Watson et al. 2011; Martínez-Aldama et al. 2019).

Through the advent of wide-field photometric surveys such as the Dark Energy

Survey, (DES, Dark Energy Survey Collaboration et al. 2016), multi-epoch photometric data for large samples of AGN has become readily available. Concurrent observations can be made with multi-object spectrographs, however the demand for these instruments is high and therefore limits the number of epochs which can be feasibly acquired. The Australian Dark Energy Survey (OzDES) and Sloan Digital Sky Survey Reverberation Mapping (SDSS-RM) Project have conducted the first multi-object RM surveys, observing hundreds of AGN probing a wide range of AGN luminosities and redshifts (King et al. 2015; Shen et al. 2015). These programs have delivered over one hundred new lag measurements (Grier et al. 2017; Hoormann et al. 2019; Grier et al. 2019; Homayouni et al. 2020; Yu et al. 2021, 2023; Malik et al. 2023, Penton et al. in prep). This allowed the Mg II and C IV $R-L$ relations to be constrained for the first time using statistically significant samples, however there is significant scatter in the measurements. This is mostly due to challenges with data quality (low signal-to-noise, limited sampling; see Malik et al. 2022) and lag recovery reliability (Li et al. 2019; Penton et al. 2022). These factors have limited the lag recovery efficacy of each survey to about 10-25%.

Stacking can be used to combine the cross-correlation signals of physically similar AGN to recover average lags for these objects. The technique was first applied by Fine et al. (2012, 2013) using only two spectroscopic epochs, which yielded a marginal result. After demonstrating the success of the technique with the Bentz et al. (2013) Hβ sample, Li et al. (2017) measured composite lags with Hα, Hβ, He II and Mg II using a subset of the SDSS-RM sample. Stacked averages are not swayed by the systematic errors from individual sources. Their consistency (or not) with the measurements made for individual sources is therefore important. Additionally, with the wide redshift range covered by our sample, the gaps in the observational window function can be filled in to some extent. Therefore, stacking leverages the data in a way that cannot be done with traditional individual measurements.

We present a stacked lag analysis of the entire OzDES sample, for the Hβ, Mg II and C IV lines. Section 4.2 details the observations obtained by OzDES and the data calibration procedures. In Section 4.3 we describe the technique used to recover stacked lags. In Section 4.4 we present our average lag measurements, and comparisons with individual measurements on the respective $R-L$ relationships for each emission line. We summarize our results and the discuss the outlook to the future in Section 4.5.

Throughout this work we adopt a flat ΛCDM cosmology, with $\Omega_\Lambda = 0.7$, $\Omega_M = 0.3$, and $H_0 = 70\ \mathrm{km\,s^{-1}\,Mpc^{-1}}$.

4.2 Data

Our photometric data were obtained as part of the Dark Energy Survey (DES) Supernova Program, which observed 10 deep fields covering 27 deg^2, comprising the ELAIS, XMM-LSS, Chandra deep-field South, and SDSS Stripe 82 fields (Kessler et al. 2015; Morganson et al. 2018). These fields were observed in the *griz* filters, with the Dark Energy Camera (DECam) on the 4m Blanco telescope at Cerro Tololo Inter-American Observatory (CTIO) (Flaugher et al. 2015). The fields were observed with ∼6 day cadence over a 5-6 month season (August to January) from 2013 to 2018, with additional science verification data taken in 2012. The OzDES project (Yuan et al. 2015; Childress et al. 2017; Lidman et al. 2020) conducted follow-up spectroscopic observations with the 2dF multi-object fibre positioning system and the AAOmega spectrograph (3700-8800 Å, Sharp et al. 2006) on the 3.9m Anglo-Australian Telescope (AAT), taken with approximately monthly cadence over the same seasons, from 2013 to 2019. After the conclusion of the Supernova Program, additional DECam observations were taken monthly in the 2018-19 season, taking the baseline of our photometric light curves to 7 years.

The OzDES Reverberation Mapping sample comprises 735 AGN, ranging from $0.1 < z < 4.0$, with apparent magnitudes $17.2 < r_{\mathrm{AB}} < 22.3$ (Tie et al. 2017). Of these 735 AGN, we removed 9 of the 78 AGN from the Hβ sample due to broad-absorption lines (BALs) or incorrect classification as a Type 1 AGN, 3 of the 453 AGN from the Mg II sample for the same reason (these sources overlapped with the Hβ sample), and 88 of the 378 AGN from the C IV sample due to BALs. These sources were included in the initial survey selection to improve the source density on the sky and

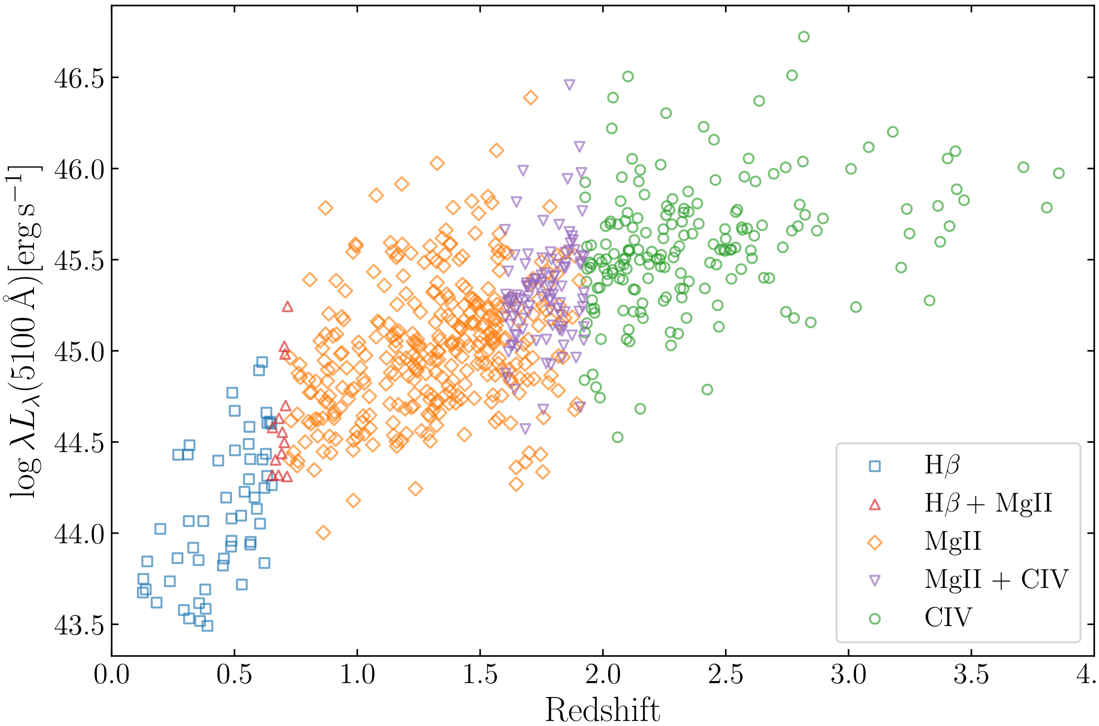

Figure 4.1: Distribution of redshifts and monochromatic luminosity at 5100 Å for the 690 AGN in the OzDES RM sample. The Hβ sample extends to $z = 0.75$, with 13 sources overlapping with our Mg II sample. The Mg II sample extends to $z = 1.92$, with 106 sources overlapping with our C IV sample.

study BAL variability, but have proven challenging for reverberation analysis. The final sample we use in this analysis comprises 69 Hβ sources, 450 Mg II sources, and 290 C IV sources (690 AGN in total). The redshift and luminosity distribution of these targets is shown in Figure 4.1.

As done for the individual lag measurements made by Yu et al. (2023) and Malik et al. (2023), for the Hβ and Mg II samples we measure the emission-line flux from spectra obtained on different nights as separate epochs in order to maximise the cadence of our sampling for our emission-line light curves. As we have lower signal-to-noise for the C IV sample, we co-add the spectra over each observing run (typically 4-7 nights during dark time each month), as done by Hoormann et al. (2019).

We do not measure the continuum luminosity directly from the spectra due to fibre aperture effects from variable atmospheric seeing and fibre placement uncertainties. From the average r-band magnitude and redshift of the AGN, we estimated the monochromatic continuum flux at rest frame 5100 Å, 3000 Å and 1350 Å using the

DECam r-band filter transmission curve and the SDSS quasar template (Vanden Berk et al. 2001). The template is scaled to the magnitude of the source, assuming $L_{\rm bol} = 9\,\lambda L_\lambda\,(5100\,\text{Å})$ (Kaspi et al. 2000). The source properties for the OzDES sample used in this work are provided in Appendix A and complete sample characteristics for the final OzDES RM sample will be provided in a future OzDES RM Program paper.

The DES photometry is calibrated using the DES data reduction pipeline (Morganson et al. 2018; Burke et al. 2018). We perform a spectrophotometric flux calibration following Hoormann et al. (2019). For the Hβ and C IV samples, we measure the line fluxes as done by Hoormann et al. (2019). For the continuum subtraction, the local continuum windows we use for Hβ are 4760 to 4790 Å and 5100 to 5130 Å, and for C IV are 1450 to 1460 Å and 1780 to 1790 Å. For the Mg II sample, the iron subtraction and line flux measurement is performed as detailed in Yu et al. (2023). The calibration uncertainties of the line flux for each line are measured using the F-star warping function method as detailed in Yu et al. (2021).

4.3 Lag recovery method

As reverberation lags should be dependent on the intrinsic AGN luminosity alone (at least to first order), we bin the sources by their continuum luminosity. Further details are provided for each emission-line subsample in §4.4.

For each source in a redshift-luminosity bin, we covert the observation dates to the rest frame of the source by dividing by $(1+z)$. We use the `PyCCF` code to perform the interpolated cross-correlation function method for each individual source (ICCF; Gaskell & Peterson 1987; Sun et al. 2018). The continuum and emission-line light curves of each source are linearly interpolated to a grid spacing of 3 days. The interpolated light curves are cross-correlated as a function of time-lag. We then average the cross-correlation functions (CCF) of each source in the bin to obtain the stacked CCF. We search for lags over a (rest-frame) lag range of $[-100, 300]$ days for Hβ and C IV, and $[-100, 500]$ days for Mg II as it has a longer expected lag for our sample.

We measure the average lag and its uncertainties by bootstrapping the sample in each bin. We perform the above procedure to calculate the stacked CCF's for each bootstrapped re-sample of the original binned sample. We repeat this 1000 times, and record the peak of each CCF ($r_{\rm max}$) to build the bootstrap distribution, from which we adopt the median and 16th and 84th percentiles of this distribution as the recovered average stacked lag, τ, and lower and upper uncertainties, σ_τ, for the bin.

Following Li et al. (2017), we shuffle the spectroscopic epochs and repeat the stacking for 100 Monte Carlo realisations, and compare the stacked CCF produced by these uncorrelated light curves to the original stacked CCF. This is similar to the null hypothesis test used by Malik et al. (2023) to check that the lag recovery is not simply a product of the interaction of the window function with underlying red-noise correlation in the photometric light curves, considering the relatively low sampling density and modest signal-to-noise of our light curves.

4.4 Results

We present the results of our stacking analysis for each emission line sample in the OzDES RM sample, and a multi-line analysis of the subsamples for which two emission-lines are present. With the basic assumption that the lag of a source is dependent on the intrinsic AGN luminosity alone, by using the stacking method we are assuming the lags of each source within a bin are similar (in the rest-frame) so that we recover a representative average lag for these AGN. Since the binned sources are at different redshifts, when the light curve data is converted to the rest-frame, different variability and reverberation time-scales are probed by each source through their unique rest-frame observational window function. By stacking we can partially circumvent the usual impact of the sparse sampling (particularly the 7-month seasonal gaps) in the light curves of any one source, as we are combining the CCF's for all sources in a bin. We compare the average lag measurements to the sample of existing individual lag measurements on the respective $R-L$ relations for each line.

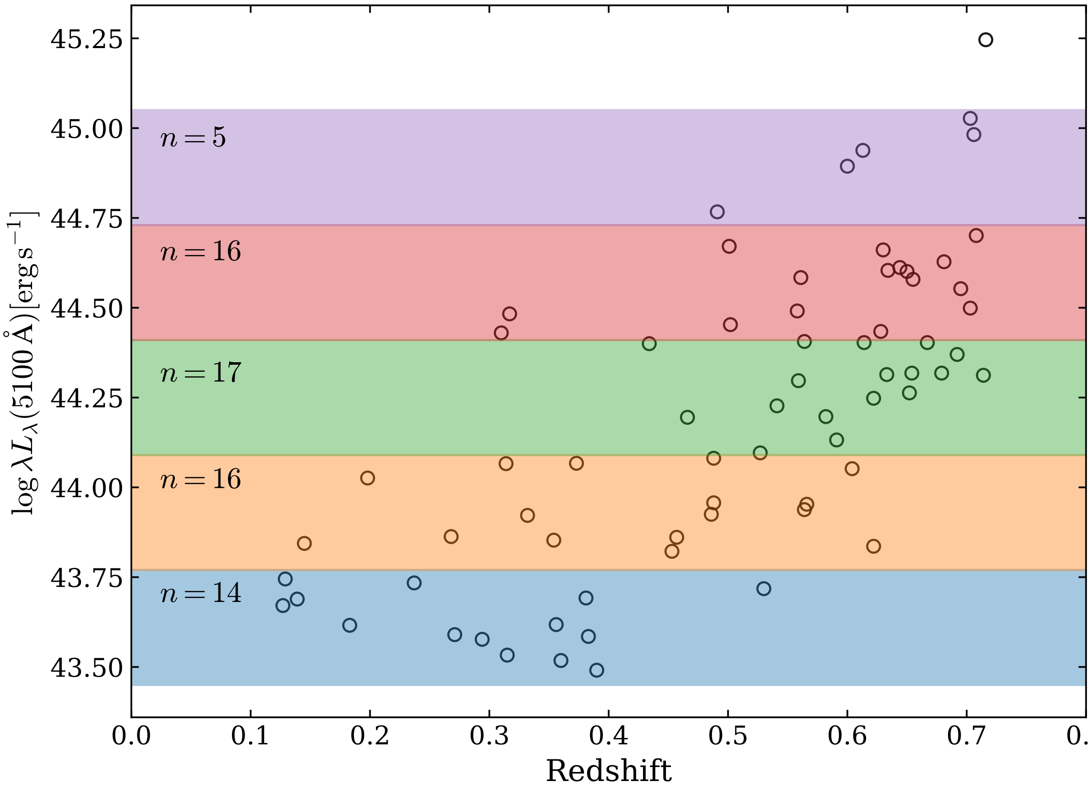

Figure 4.2: The luminosity bins for the Hβ sample, labelled with the number of binned sources. Within each bin, the standard deviation of the expected lags for the individual sources (measured using the source luminosity and the Bentz et al. (2013) $R - L$ relation for Hβ) is $\sim$10% of the expected mean lag for the binned sample (measured as the mean of the expected lags for the individual sources).

4.4.1 Hβ

We divide our sample into five luminosity bins of equal size, as shown in Figure 4.2. The size of the bins were chosen as to maximise the number of sources in each bin while avoiding introducing a broad underlying distribution in the expected lags. The highest luminosity source was excluded from the analysis for this reason. Although there are a relatively small number of sources stacked in each bin, particularly when compared to stacking done by Fine et al. (2012, 2013), the signal-to-noise of our stacked CCF's are sufficiently high as we have much more light curve data.

The stacked CCF's for each bin of the Hβ sample are shown in Figure 4.3, alongside the total number of overlapping light curve epochs as a function of time-lag for all sources stacked within the bin. As the observation dates of each source in a bin are converted to the rest-frame of the source, and there is a distribution of source redshifts within each bin, the total light curve sampling of the stacked sample begins

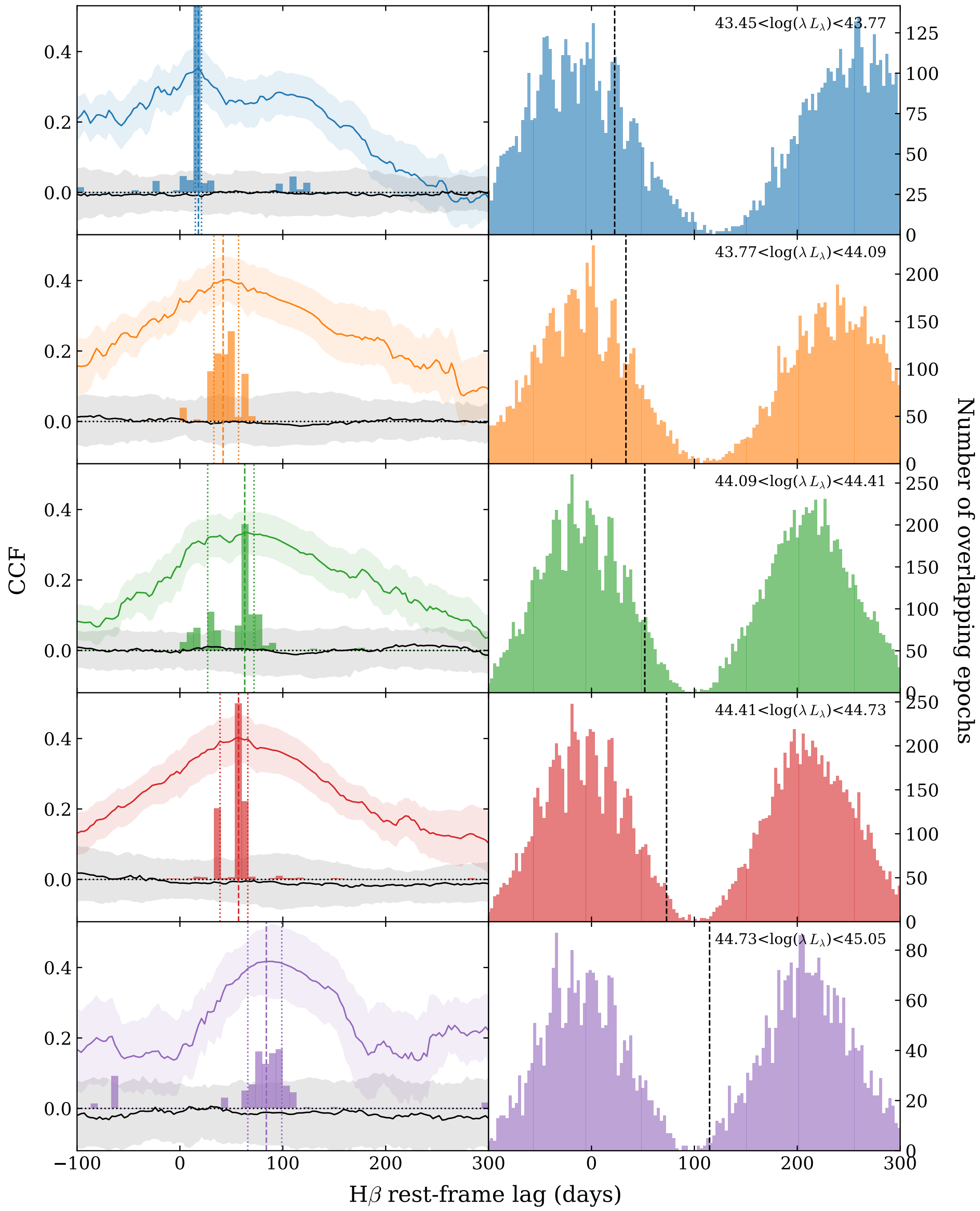

Figure 4.3: *Left column:* The coloured solid lines are the stacked cross correlation functions (CCF) for each of the five luminosity bins for the Hβ sample. The colours correspond to the respective bins in Figure 4.2. The 1σ scatter of the bootstrapped CCF's is shown by the coloured shaded region. The vertical dashed and dotted lines indicate the recovered average lag and its uncertainty, as measured from the bootstrap distribution (coloured histogram). The black solid line and grey shaded area show the mean and 1σ scatter of the CCF's generated using the randomised spectroscopic light curves following the procedure described in §4.3. *Right column:* The number of overlapping spectroscopic and photometric epochs as a function of time lag, in total for each source in the corresponding bin. The expected mean lag for the bin is indicated by the black dashed line.

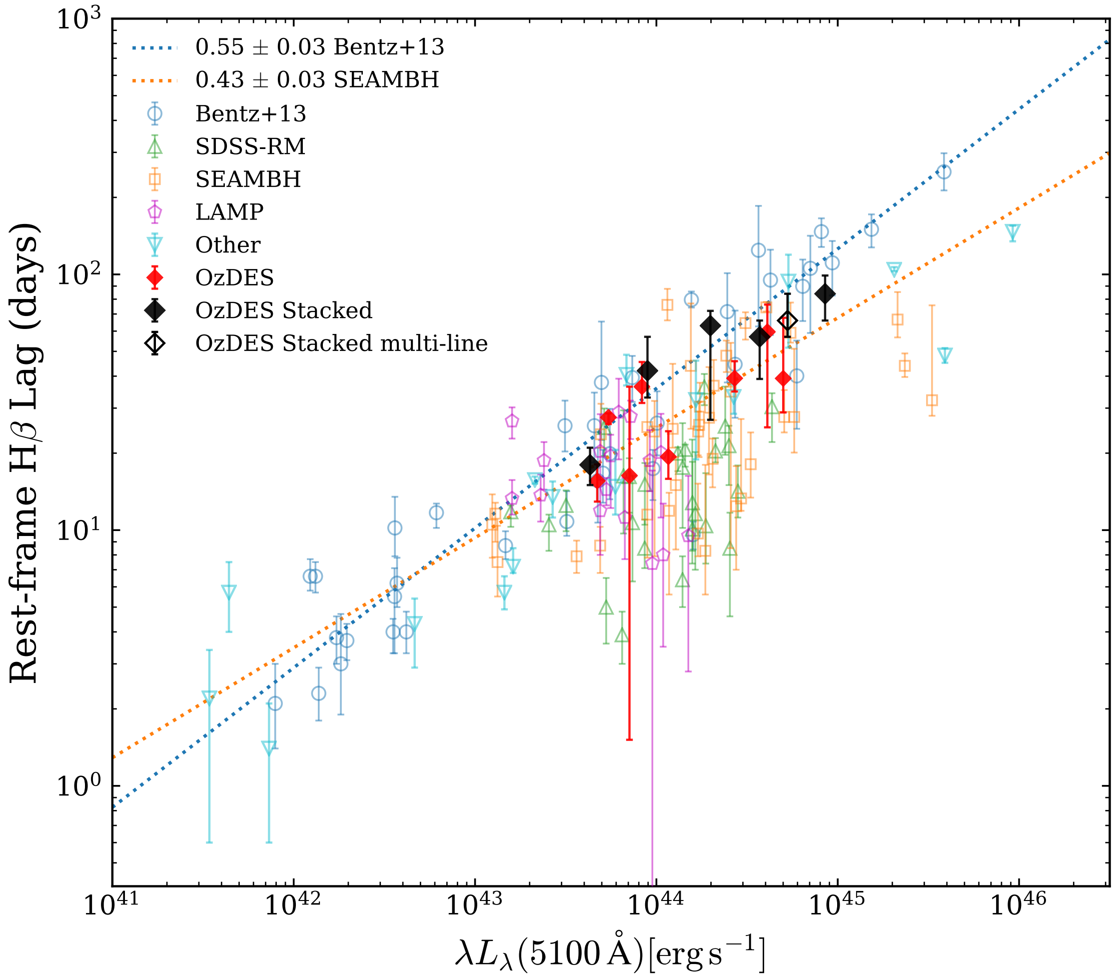

Figure 4.4: The Radius-Luminosity relation for Hβ (dotted lines), including the stacked average lag measurements made using the OzDES Hβ sample, and existing individual lag measurements from Bentz et al. (2013, and references therein); SDSS-RM (Grier et al. 2017, quality 4 and 5); SEAMBH (Du et al. 2014; Wang et al. 2014a; Du et al. 2015, 2016, 2018; Hu et al. 2021); Lick AGN Monitoring Project (LAMP, U et al. 2022); and other measurements from Bentz et al. (2009); Barth et al. (2013); Bentz et al. (2014); Pei et al. (2014); Lu et al. (2016); Bentz et al. (2016a,b); Fausnaugh et al. (2017); Zhang et al. (2019); Rakshit et al. (2019); Li et al. (2021), of which measurements published before 2019 are compiled by Martínez-Aldama et al. (2019). The multi-line average lag measurement is presented in §4.4.4.

to in-fill the rest frame observational gap imposed by the observed frame 7-month seasonal gap present in the individual observed light curves.

Comparing the stacked CCF, and its scatter measured from bootstrapping, to the stacked CCF's after light curve randomisation, we see significant correlation signal present. This implies that the signal is not dominated by the correlation of any individual source. In all cases there is one major peak present, however, the lowest luminosity bin (blue) has a flatter CCF. There is limited but non-zero data overlap around the expected mean lags for the two highest luminosity bins, as they coincide with the first seasonal gap in our light curves. However, we recover significant average lags in each of these bins. This demonstrates the ability of stacking to overcome the limitations imposed by sparse sampling, which impede lag recovery for individual sources.

We plot the recovered average lags from each luminosity bin on the $R-L$ relation, as shown in Figure 4.4. Our stacked measurements are consistent with the Bentz et al. (2013) slope, which agrees with the physically motivated slope of ∼0.5. The uncertainty in the average lags are consistent to the uncertainties in the eight lags recovered for individual sources (Malik et al. 2023), and are inconsistent with the distribution of the SDSS-RM measurements (Grier et al. 2017; Li et al. 2017), for which shorter lags are recovered. Given the similarities of our programs and sample selection, the reason for this discrepancy is unclear. Although the main difference between the surveys is the baseline and cadence of the data, simulations by Fonseca Alvarez et al. (2020) and Malik et al. (2022) find that this does not bias the lag recovery of SDSS-RM to shorter lags, or OzDES to longer lags. For our composite lags we bin across our entire Hβ sample, and do not reject any sources based on light curve signal-to-noise, or any other criteria.

As a test, we repeated the stacking after excluding all the objects with individual recovered lags (Malik et al. 2023). We show the results of this test in §4.6. Although the average lag uncertainties increase after the exclusion, the lags remain in close agreement with those from the original analysis.

4.4.2 Mg II

The three luminosity bins used for the Mg II sample are shown in Figure 4.5. The lowest and highest luminosity bins are slightly wider to include sources close to the edge of the bin. Ten sources were excluded from the analysis to optimise the bin densities and reduced smoothing of the stacked CCF's. Larger luminosity bins were required to achieve adequate signal-to-noise in the stacked CCF's for this sample.

We present the stacked CCF's in Figure 4.6. The strength of the correlation signals

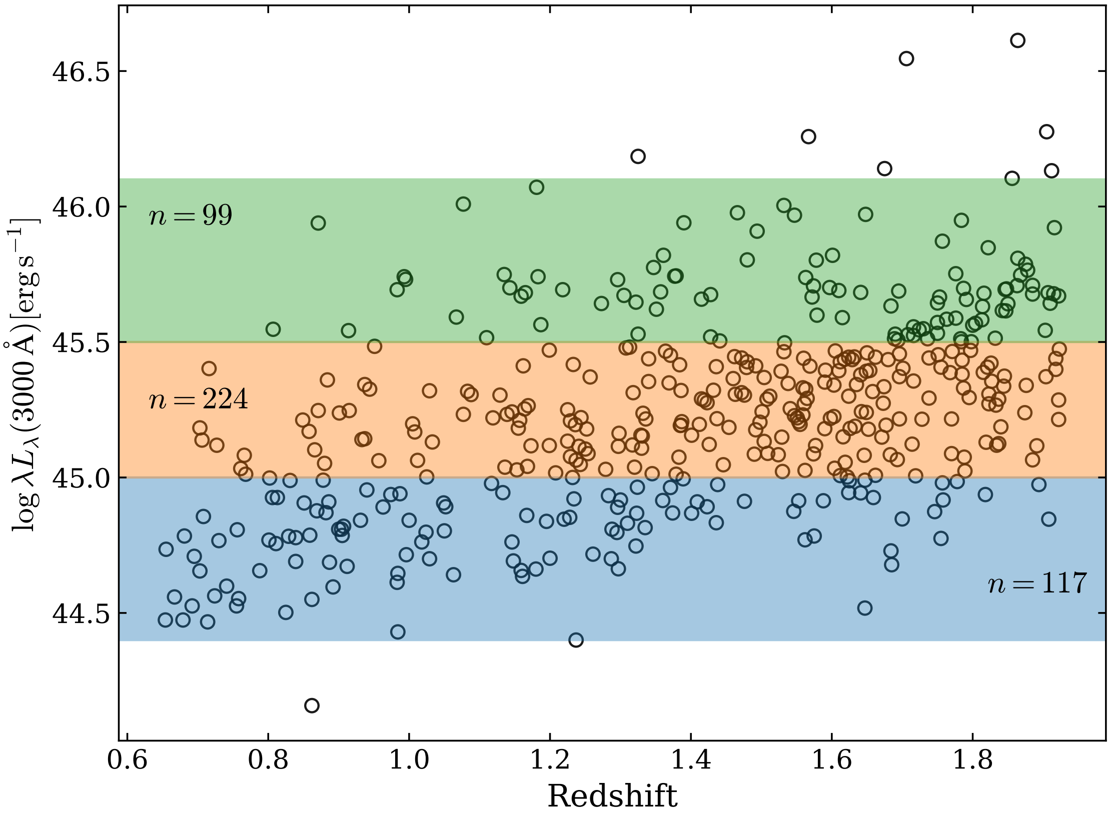

Figure 4.5: The luminosity bins for the Mg II sample, labelled with the number of binned sources. Within each bin, the standard deviation of the expected lags for the individual sources (measured using the source luminosity and the Trakhtenbrot & Netzer (2012) $R-L$ relation for Mg II) is ~20% of the expected mean lag for the binned sample.

in each bin are lower than for the Hβ sample, however, comparing to the randomised CCF's we can see there is significant signal present. The signal-to-noise of the Mg II light-curve input data is lower than for the Hβ sample, as the Mg II sample is fainter and requires subtraction of Fe II from the emission-line (Yu et al. 2021, 2023). However, we have 450 AGN in the Mg II sample, and are therefore stacking many more sources in each bin. Since sample size is not the limiting factor in this case, the lower signal-to-noise of the Mg II line light curves must be producing weaker stacked cross correlation signals. In the lowest luminosity bin, the signal is flat and no clear peak is present. For the other two bins a dominant peak is present, and the bootstrap distributions are adequately constrained to recover average lags.

We plot the recovered average lags from each luminosity bin on the Mg II $R-L$ relation in Figure 4.7, along with the 25 individual measurements made with this

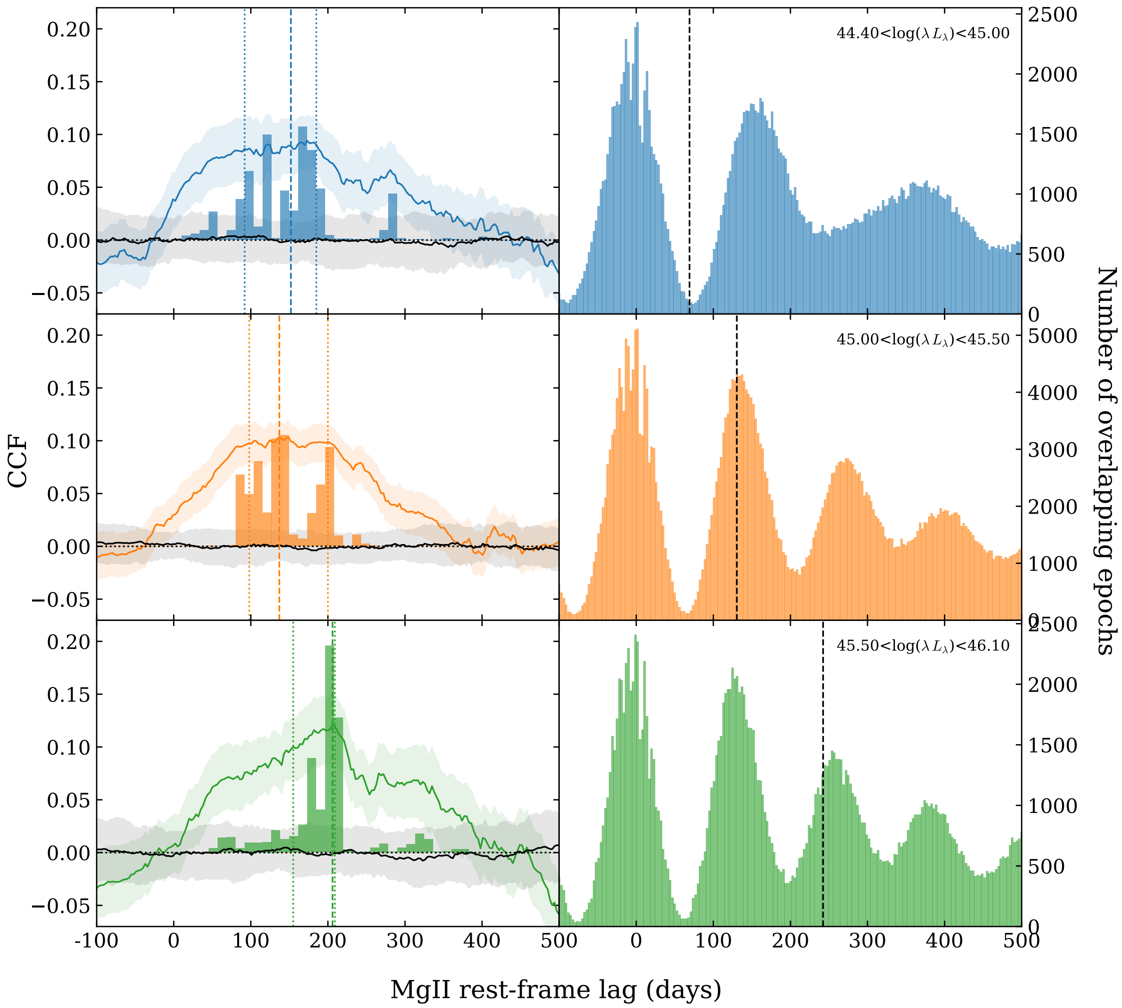

Figure 4.6: *Left column:* The coloured solid lines are the stacked cross correlation functions (CCF) for each of the three luminosity bins for the Mg II sample. The colours correspond to the respective bins in Figure 4.5. The 1σ scatter of the bootstrapped CCF's is shown by the coloured shaded region. The vertical dashed and dotted lines indicate the recovered average lag and its uncertainty, as measured from the bootstrap distribution (coloured histogram). The black solid line and grey shaded area show the mean and 1σ scatter of the CCF's generated using the randomised spectroscopic light curves following the procedure described in the text. *Right column:* The number of overlapping spectroscopic and photometric epochs as a function of time lag, in total for each source in the corresponding bin. The expected mean lag for the bin is indicated by the black dashed line.

sample by Yu et al. (2023). The average lags are in agreement with the recent results from Homayouni et al. (2020) and Yu et al. (2023). There is a progression to longer lags with higher luminosities with the intermediate and highest luminosity bins, however, the mean lag in the lowest bin is not well constrained. As shown in Figure 4.6, there is limited data coverage over the expected mean lags for the lowest luminosity bin (blue), which coincides with the first seasonal gap in our light

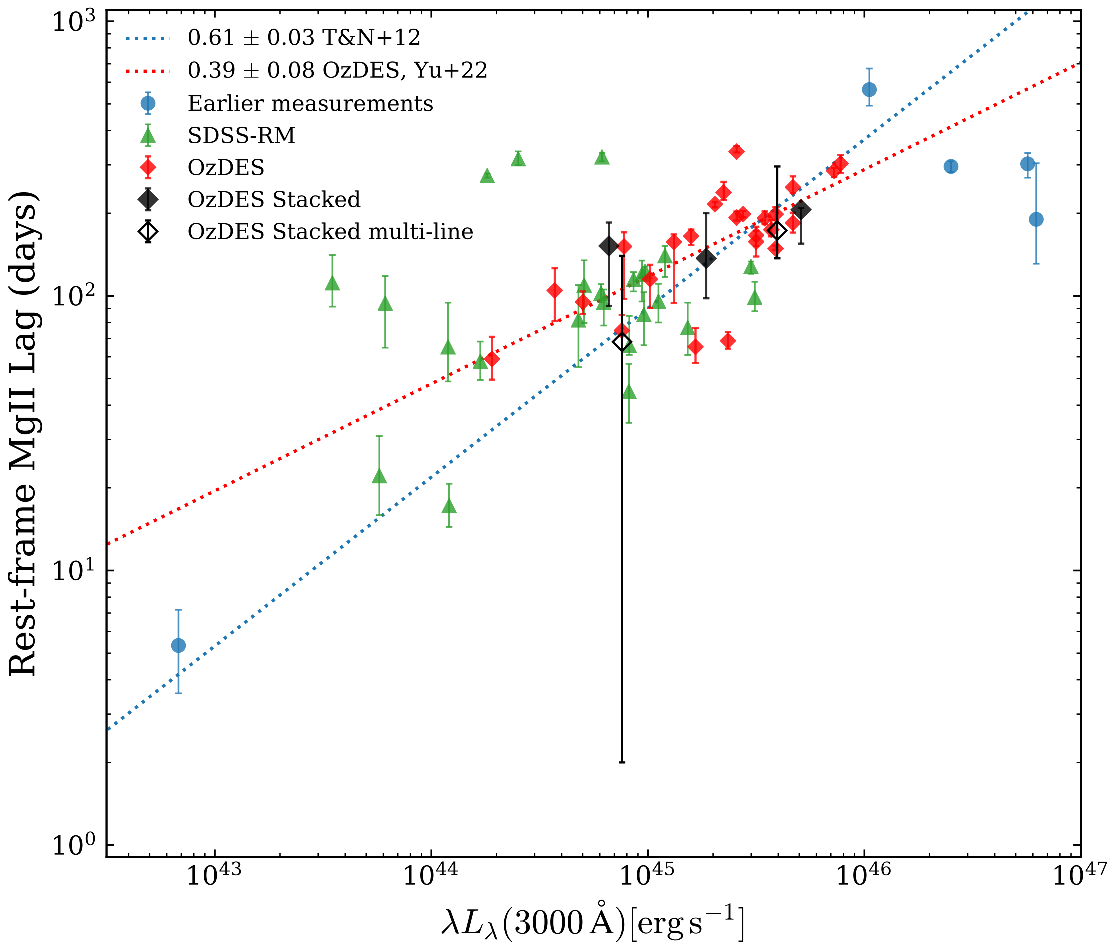

Figure 4.7: Radius-Luminosity relation for Mg II, with existing individual lag measurements from Metzroth et al. (2006); Lira et al. (2018); Czerny et al. (2019); Zajaček et al. (2020, 2021) and SDSS-RM (Homayouni et al. 2020, gold sample), along with the OzDES individual measurements (Yu et al. 2023), and our stacked average lag measurements. The multi-line average lag measurements are presented in §4.4.4.

curves. The time-dilation distribution over the binned sample is not sufficient to 'fill in' the short timescales, but it is able to sufficiently bridge the second seasonal gap. This could explain why the the recovered average lag for the lowest luminosity bin is not as consistent with the individual OzDES measurements, but they are consistent for two higher luminosity bins. The average lags for the lowest and intermediate luminosity bins are formally consistent with both the steeper $R-L$ relation measured by Trakhtenbrot & Netzer (2012), and the shallower relation recently constrained by Yu et al. (2023), however, the better constrained mean lag for the highest luminosity bin is only consistent with the shallower relation.

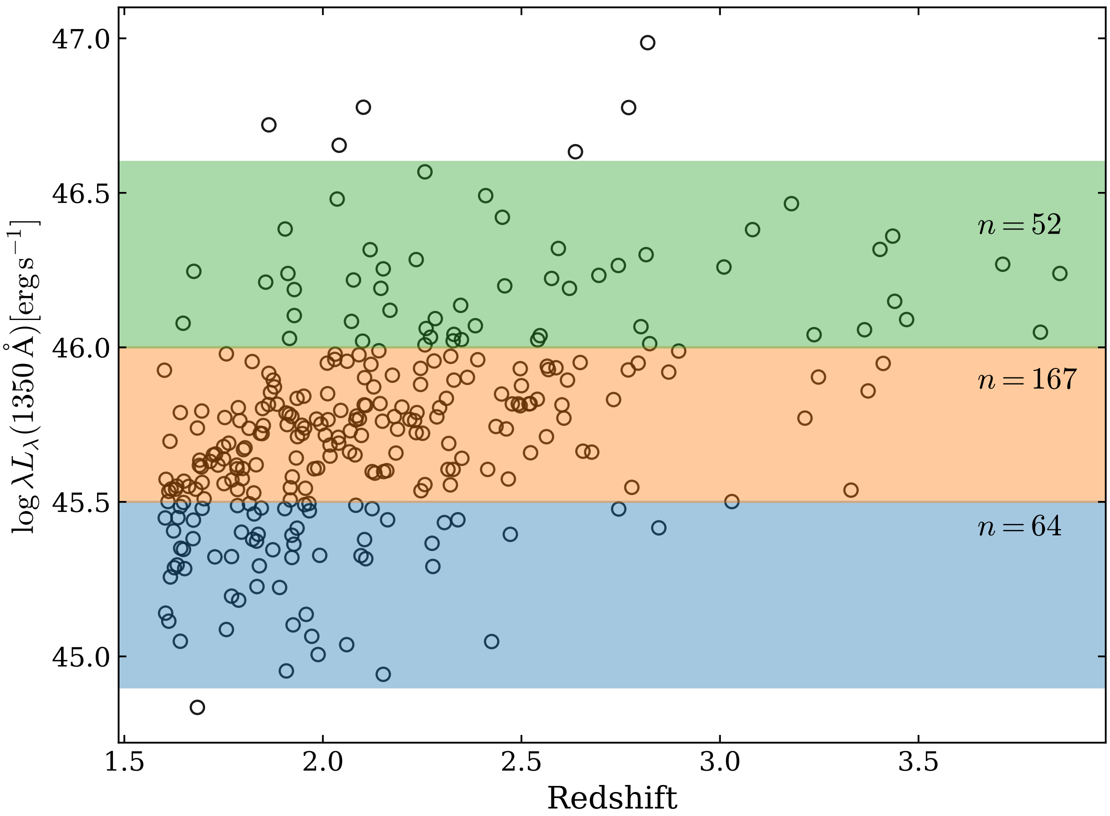

Figure 4.8: The luminosity bins for the C IV sample, labelled with the number of binned sources. Within each bin, the standard deviation of the expected lags for the individual sources (measured using the source luminosity and the Hoormann et al. (2019) $R - L$ relation for C IV) is $\sim$15% of the expected mean lag for the binned sample.

4.4.3 C IV

As for the previous samples, we present the luminosity bins for the C IV sample in Figure 4.8, and the stacked CCF results in Figure 4.9. As required for Mg II, larger luminosity bins were necessary to achieve sufficient signal-to-noise after stacking, and nine sources were excluded from the analysis to avoid overly wide bins in luminosity. The OzDES C IV sample has lower signal-to-noise than the Hβ and Mg II samples, as the AGN are faint. The bootstrap distributions are not well constrained for the lowest or highest luminosity bins. However, Li et al. (2017) found that the mean recovered lag remains stable when the light curve signal-to-noise is degraded, although the uncertainty increases proportionally with the decline. Therefore we continue to recover the average lags and compare with individual source measurements.

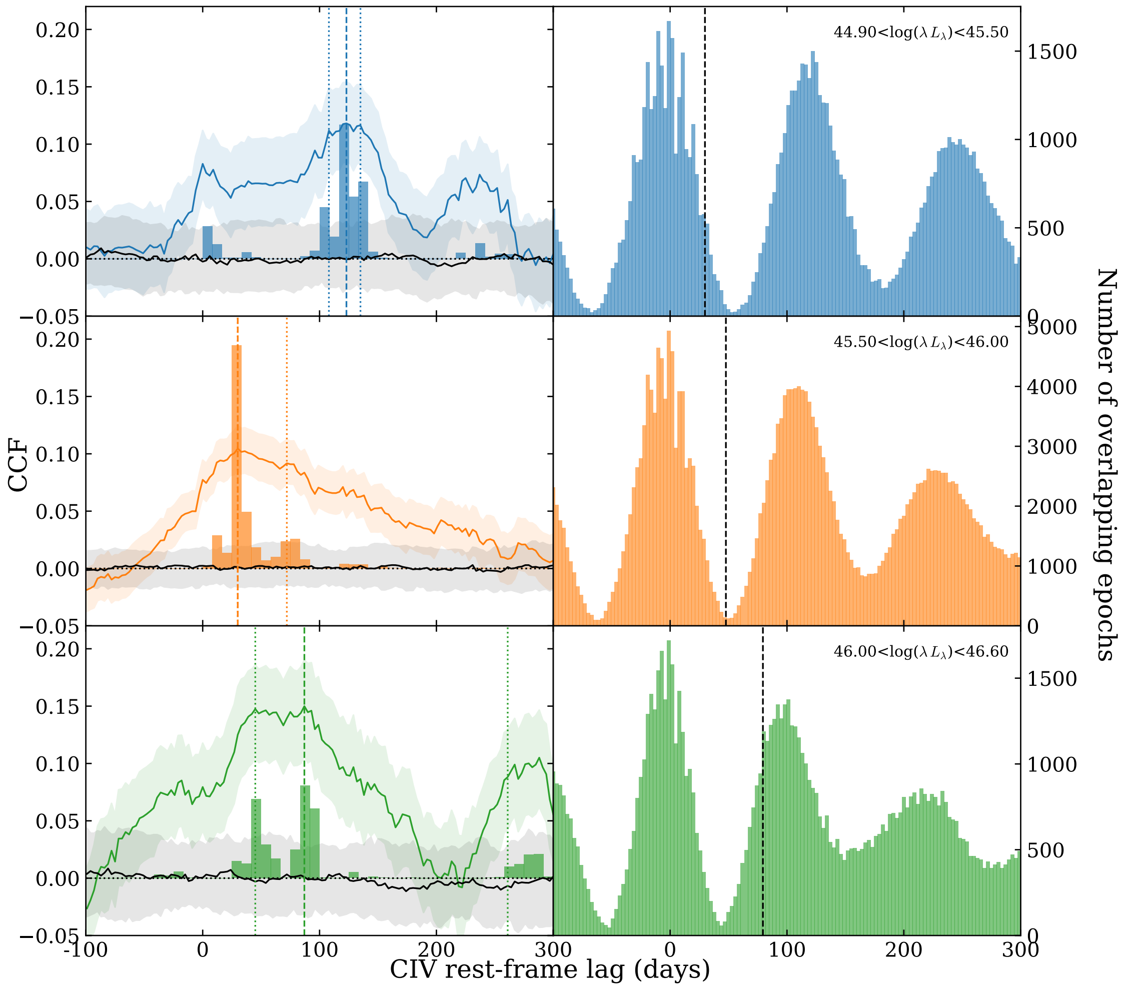

Figure 4.9: *Left column:* The coloured solid lines are the stacked cross correlation functions (CCF) for each of the three luminosity bins for the C IV sample. The colours correspond to the respective bins in Figure 4.8. The 1σ scatter of the bootstrapped CCF's is shown by the coloured shaded region. The vertical dashed and dotted lines indicate the recovered average lag and its uncertainty, as measured from the bootstrap distribution (coloured histogram). The black solid line and grey shaded area show the mean and 1σ scatter of the CCF's generated using the randomised spectroscopic light curves following the procedure described in the text. *Right column:* The number of overlapping spectroscopic and photometric epochs as a function of time lag, in total for each source in the corresponding bin. The expected mean lag for the bin is indicated by the black dashed line.

We plot the stacked average lags from the C IV sample alongside existing measurements from the literature in Figure 4.10. Although the uncertainties on the average lags from the intermediate and highest luminosity bins are large, they are in agreement with the $R-L$ relations constrained by Hoormann et al. (2019) and Grier et al. (2019). As discussed for the Mg II sample, the time dilation over the binned samples does not sufficiently bridge the first of the 7-month seasonal gaps in our

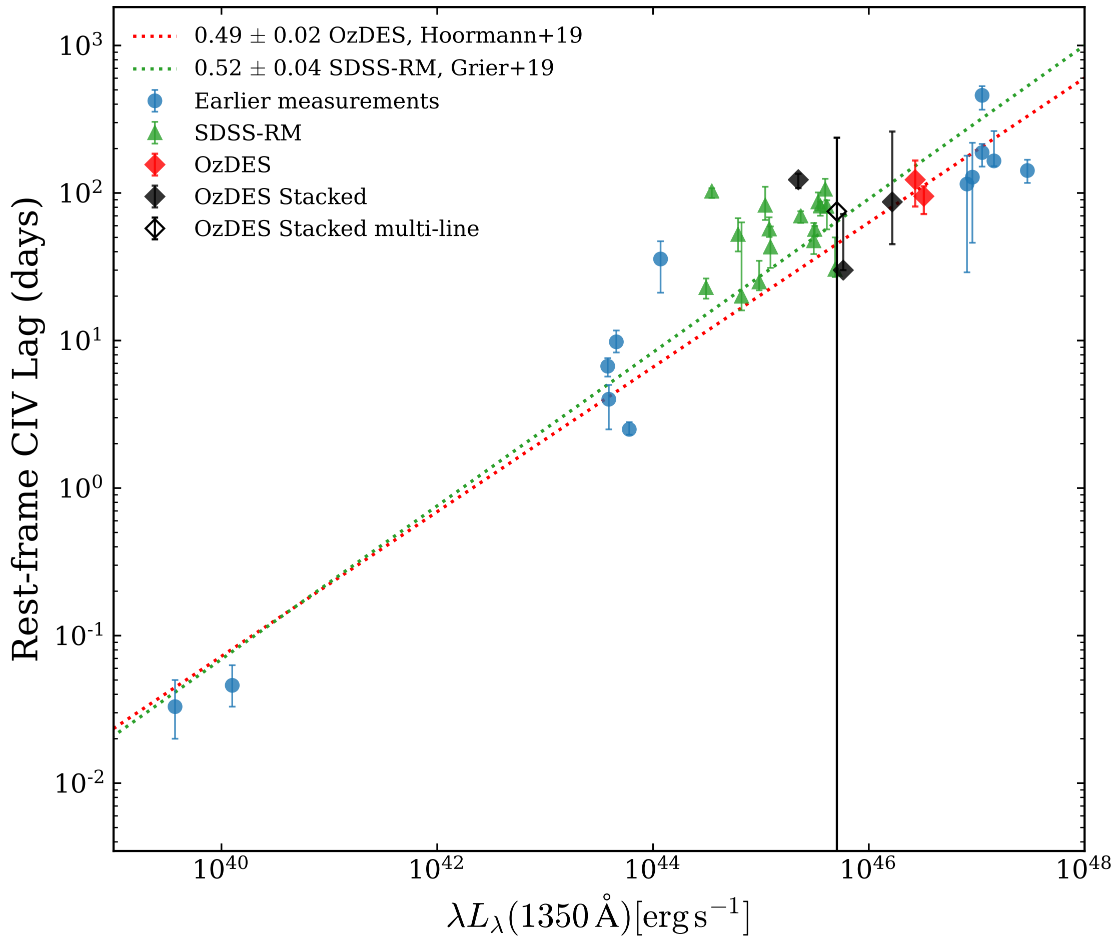

Figure 4.10: Radius-Luminosity relation for C IV, with our stacked average lags and existing individual lag measurements from Peterson et al. (2005, and references therein); Kaspi et al. (2007); Trevese et al. (2014); Lira et al. (2018), and SDSS-RM (Grier et al. 2019; Shen et al. 2019b, gold sample), Kaspi et al. (2021), along with the OzDES individual measurements (Hoormann et al. 2019). The multi-line average lag measurement is presented in §4.4.4.

light curves. With the shorter expected lags for C IV, the average lags for the lowest luminosity bin coincides with this gap. In addition to the lower signal-to-noise of the light curves, this may be contributing to the poorer quality of the stacked CCF's. It is unclear why the average lag recovered for the lowest luminosity bin is much longer than expected, and it is inconsistent with the progression to longer lags with high luminosities seen by the lags in the other two bins.

4.4.4 Multi-line measurements

Both the Hβ and Mg II lines are visible for 13 AGN, and Mg II and C IV for 106 AGN (see Figure 4.1). We attempt to recover average lags independently with each

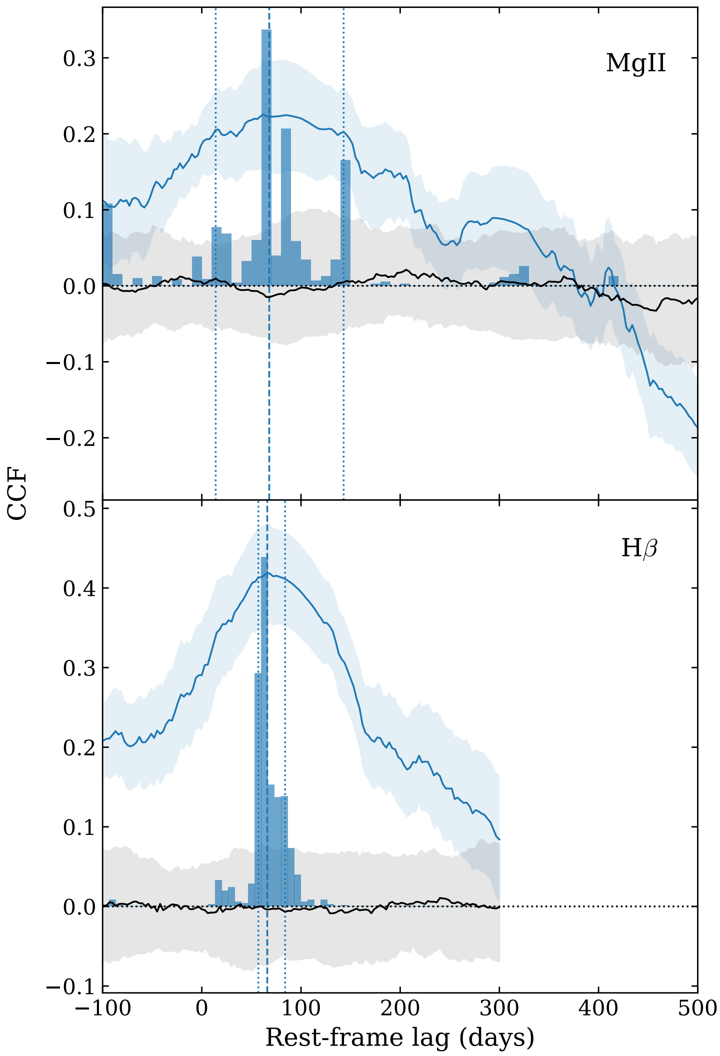

Figure 4.11: The stacked cross correlation functions (CCF) for the multi-line sample with both Hβ and Mg II, comprising 13 AGN.

line, in order to compare the lag ratios to investigate the ionisation stratification of the BLR.

We repeated the stacking procedure for the sample of 13 AGN with the Hβ and Mg II light curves. As there are few sources we do not bin them by luminosity. We present the stacked CCF's for each line in Figure 4.11. We measure an average lag of 66^{+18}_{-9} days for the Hβ sample, and an average lag of 68^{+75}_{-54} days for the Mg II sample. We formally recover a Mg II to Hβ lag ratio of 1.03, however the inherent uncertainty is significant due to the large uncertainty of the Mg II average lag. This result is broadly consistent with the expectation that these two BLRs are approximately cospatial. This ratio is consistent with previous multi-line measurements made by

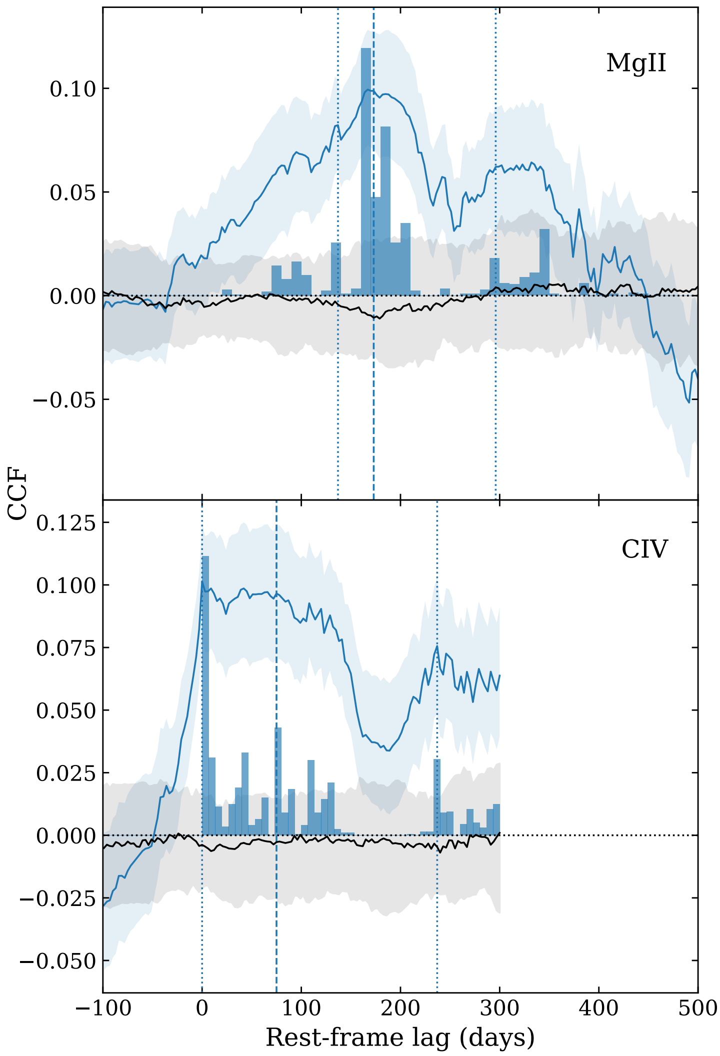

Figure 4.12: The stacked cross correlation functions (CCF) for the multi-line sample with both Mg II and C IV, comprising 106 AGN.

Homayouni et al. (2020), who found that Mg II is emitted from a similar or slightly larger region than Hβ in several individual sources, as well as Clavel et al. (1991) and Czerny et al. (2019).

We repeated this for the sample of 106 AGN with Mg II and C IV, and present the stacked CCF's in Figure 4.12. The signal-to-noise was insufficient to divide the sample into two luminosity bins. Although the lags are not well constrained (particularly for the C IV sample), we measure an average Mg II lag of 173^{+123}_{-36} days, and an average C IV lag of 75^{+162}_{-75} days. We formally recover a Mg II to C IV lag ratio of 2.31. The average lags are broadly consistent with the BLR stratification model, and the multi-line comparison made for a single source by Homayouni et al. (2020).

Table 4.1: The average lags for each luminosity bin or multi-line sample, for each emission-line sample from the OzDES RM Program. Luminosities are given in erg s^{-1}, and average lags are in the rest frame.

Hβ	
Binned sample	Average lag (days)
$43.45<\log(\lambda L_\lambda)<43.77$	18^{+3}_{-3}
$43.77<\log(\lambda L_\lambda)<44.09$	42^{+15}_{-9}
$44.09<\log(\lambda L_\lambda)<44.41$	63^{+9}_{-36}
$44.41<\log(\lambda L_\lambda)<44.73$	57^{+9}_{-18}
$44.73<\log(\lambda L_\lambda)<45.05$	84^{+15}_{-18}
multi-line Hβ + Mg II	66^{+18}_{-9}
Mg II	
Binned sample	Average lag (days)
$44.40<\log(\lambda L_\lambda)<45.00$	152^{+33}_{-60}
$45.00<\log(\lambda L_\lambda)<45.50$	137^{+63}_{-39}
$45.50<\log(\lambda L_\lambda)<46.10$	206^{+3}_{-51}
multi-line Mg II + Hβ	68^{+75}_{-54}
multi-line Mg II + C IV	173^{+123}_{-36}
C IV	
Binned sample	Average lag (days)
$44.90<\log(\lambda L_\lambda)<45.50$	123^{+12}_{-15}
$45.50<\log(\lambda L_\lambda)<46.00$	30^{+42}_{-0}
$46.00<\log(\lambda L_\lambda)<46.60$	87^{+174}_{-42}
multi-line C IV + Mg II	75^{+162}_{-75}

We include the average lags recovered from the multi-line samples on the respective $R-L$ plots presented in Figure 4.4, Figure 4.7 and Figure 4.10. We also provide all average lags recovered in this work from each multi-line and emission line sample in Table 4.1.

4.5 Summary

We use the stacking technique developed by Fine et al. (2012, 2013) to measure average lags in luminosity bins for the Hβ, Mg II and C IV samples from the OzDES Reverberation Mapping Program. By utilising the bulk of our sample to recover composite lags, we avoid the potential selection biases in the lag recovery for individual sources. We successfully recover significant cross-correlation signals for each emission-line sample:

- The average lags from each luminosity bin of the Hβ sample are consistent with the $R - L$ relation constrained by Bentz et al. (2013), and the size of the uncertainties on the average lags are on par with that of individual measurements, despite the relatively small number of sources stacked in each bin. This provides confidence in the individual measurements, and demonstrates the potential for stacked RM analyses to improve upon constraints which have thus far been made with individual source measurements alone.

- For Mg ii and C iv, the stacked cross-correlations are weaker, but still present above the correlation signal generated using randomised light curves. Further data or larger samples are required to recover significant average lags for these samples across each luminosity bin.

- From our multi-line analysis, we measure a Mg ii to Hβ lag ratio that is consistent with earlier findings that the size of each of these line-emitting regions is similar. Our average lags for the Mg ii and C iv multi-line sample are not well-constrained due to the limited sample size, however, the lag ratio we recover is largely consistent with the BLR ionisation stratification model.

Stacking can be applied beyond RM-specific surveys. It can be done with just a few spectroscopic epochs, using large AGN samples, provided the continuum behaviour is well sampled. With LSST forthcoming, high cadence photometry of the deep-drilling fields will yield quality continuum light curves for tens of thousands of AGN. The SDSS-V Black Hole Mapper (BHM) will be spectroscopically following these fields. In addition to their dedicated RM survey of $\sim 1,000$ AGN, SDSS-V BHM will monitor 25,000 AGN over multiple epochs, which will be combined with earlier SDSS spectra (Kollmeier et al. 2017). The Time Domain Extragalactic Survey (TiDES) will also be following up these fields to conduct an RM survey of ~ 700 AGN up to $z \sim 2.5$ (Swann et al. 2019). Stacking analyses of these future, large samples has promise to significantly extend the reverberation mapping results from these projects. Although the improved signal-to-noise and survey sampling of these future programs are expected to yield an increased number of higher quality individual lag measurements than the first generation of multi-object RM surveys, these datasets can benefit from the ability of stacking to alleviate the impact of the unavoidable seasonal gaps on lag recovery (Malik et al. 2022). Stacking also presents an opportunity to combine all large time-domain datasets to recover average lags that are potentially more robust than individual lags, which remain challenging to recover reliably, particularly at high redshift.

Acknowledgements

UM and AP are supported by the Australian Government Research Training Program (RTP) Scholarship. PM and ZY are supported in part by the United States National Science Foundation under Grant No. 161553 to PM. PM also acknowledges support from the United States Department of Energy, Office of High Energy Physics under Award Number DE-SC-0011726. TMD is supported by an Australian Research Council Laureate Fellowship (project number FL180100168).

We acknowledge parts of this research were carried out on the traditional lands of the Ngunnawal and Ngambri peoples. This work makes use of data acquired at the Anglo-Australian Telescope, under program A/2013B/012. We acknowledge the Gamilaraay people as the traditional owners of the land on which the AAT stands. We pay our respects to their elders past and present.

This analysis used `NumPy` (Harris et al. 2020), `Astropy` (Astropy Collaboration et al. 2013, 2018), and `SciPy` (Virtanen et al. 2020). Plots were made using `Matplotlib` (Hunter 2007). This work has made use of the SAO/NASA Astrophysics Data System Bibliographic Services.

This paper has gone through internal review by the DES collaboration. Funding for the DES Projects has been provided by the U.S. Department of Energy, the U.S. National Science Foundation, the Ministry of Science and Education of Spain, the Science and Technology Facilities Council of the United Kingdom, the Higher Education Funding Council for England, the National Center for Supercomputing Applications at the University of Illinois at Urbana-Champaign, the Kavli Institute of Cosmological Physics at the University of Chicago, the Center for Cosmology and Astro-Particle Physics at the Ohio State University, the Mitchell Institute for Fundamental Physics and Astronomy at Texas A&M University, Financiadora de Estudos e Projetos, Fundação Carlos Chagas Filho de Amparo à Pesquisa do Estado do Rio de Janeiro, Conselho Nacional de Desenvolvimento Científico e Tecnológico and the Ministério da Ciência, Tecnologia e Inovação, the Deutsche Forschungsgemeinschaft and the Collaborating Institutions in the Dark Energy Survey.

The Collaborating Institutions are Argonne National Laboratory, the University of California at Santa Cruz, the University of Cambridge, Centro de Investigaciones Energéticas, Medioambientales y Tecnológicas-Madrid, the University of Chicago, University College London, the DES-Brazil Consortium, the University of Edinburgh, the Eidgenössische Technische Hochschule (ETH) Zürich, Fermi National Accelerator Laboratory, the University of Illinois at Urbana-Champaign, the Institut de Ciències de l'Espai (IEEC/CSIC), the Institut de Física d'Altes Energies, Lawrence Berkeley National Laboratory, the Ludwig-Maximilians Universität München and the associated Excellence Cluster Universe, the University of Michigan, NSF's NOIRLab, the University of Nottingham, The Ohio State University, the University of Pennsylvania, the University of Portsmouth, SLAC National Accelerator Laboratory, Stanford University, the University of Sussex, Texas A&M University, and the OzDES Membership Consortium.

Based in part on observations at Cerro Tololo Inter-American Observatory at NSF's NOIRLab (NOIRLab Prop. ID 2012B-0001; PI: J. Frieman), which is managed by the Association of Universities for Research in Astronomy (AURA) under a cooperative agreement with the National Science Foundation.

The DES data management system is supported by the National Science Foundation under Grant Numbers AST-1138766 and AST-1536171. The DES participants from Spanish institutions are partially supported by MICINN under grants ESP2017-89838, PGC2018-094773, PGC2018-102021, SEV-2016-0588, SEV-2016-0597, and MDM-2015-0509, some of which include ERDF funds from the European Union. IFAE is partially funded by the CERCA program of the Generalitat de Catalunya. Research leading to these results has received funding from the European Research

Council under the European Union's Seventh Framework Program (FP7/2007-2013) including ERC grant agreements 240672, 291329, and 306478. We acknowledge support from the Brazilian Instituto Nacional de Ciência e Tecnologia (INCT) do e-Universo (CNPq grant 465376/2014-2).

This manuscript has been authored by Fermi Research Alliance, LLC under Contract No. DE-AC02-07CH11359 with the U.S. Department of Energy, Office of Science, Office of High Energy Physics.

4.6 Appendix

Hβ excluding objects with individual lags

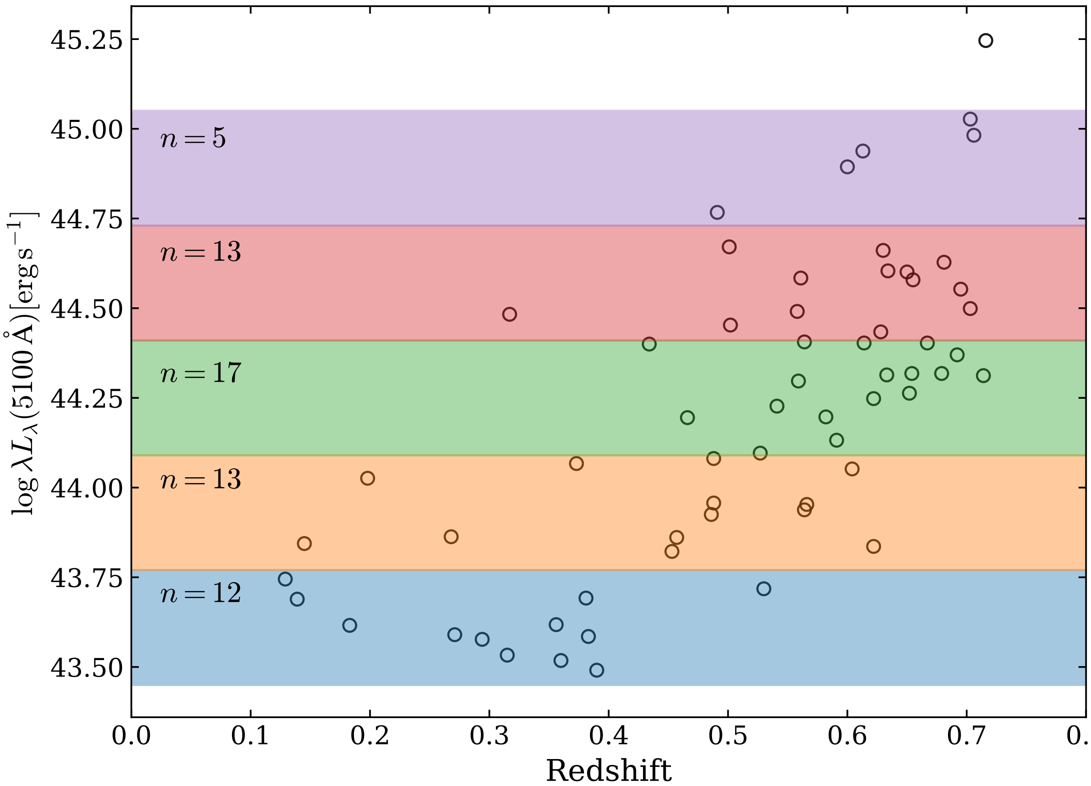

Figure 4.13: The same as Figure 4.2 after excluding sources with individual lag recoveries.

The luminosity bins for the Hβ sample excluding sources with individual lags are shown in Figure 4.13, and the stacked CCF's and average lags for this reduced sample are given in Figure 4.14 and Figure 4.15. Only the two lowest (blue and orange) and second highest (red) luminosity bins had objects excluded. The stacked CCF peaks remain intact for each of these bins, although the signal-to-noise degrades slightly, which is to expected as the size of the stacked sample decreased by ∼one sixth. The average lags are in close agreement to those recovered in the original analysis in §4.4.1. This test indicates that the results from stacking are not dominated by objects with high quality individual lags, although their addition does considerably improve the lag uncertainties for the final result.

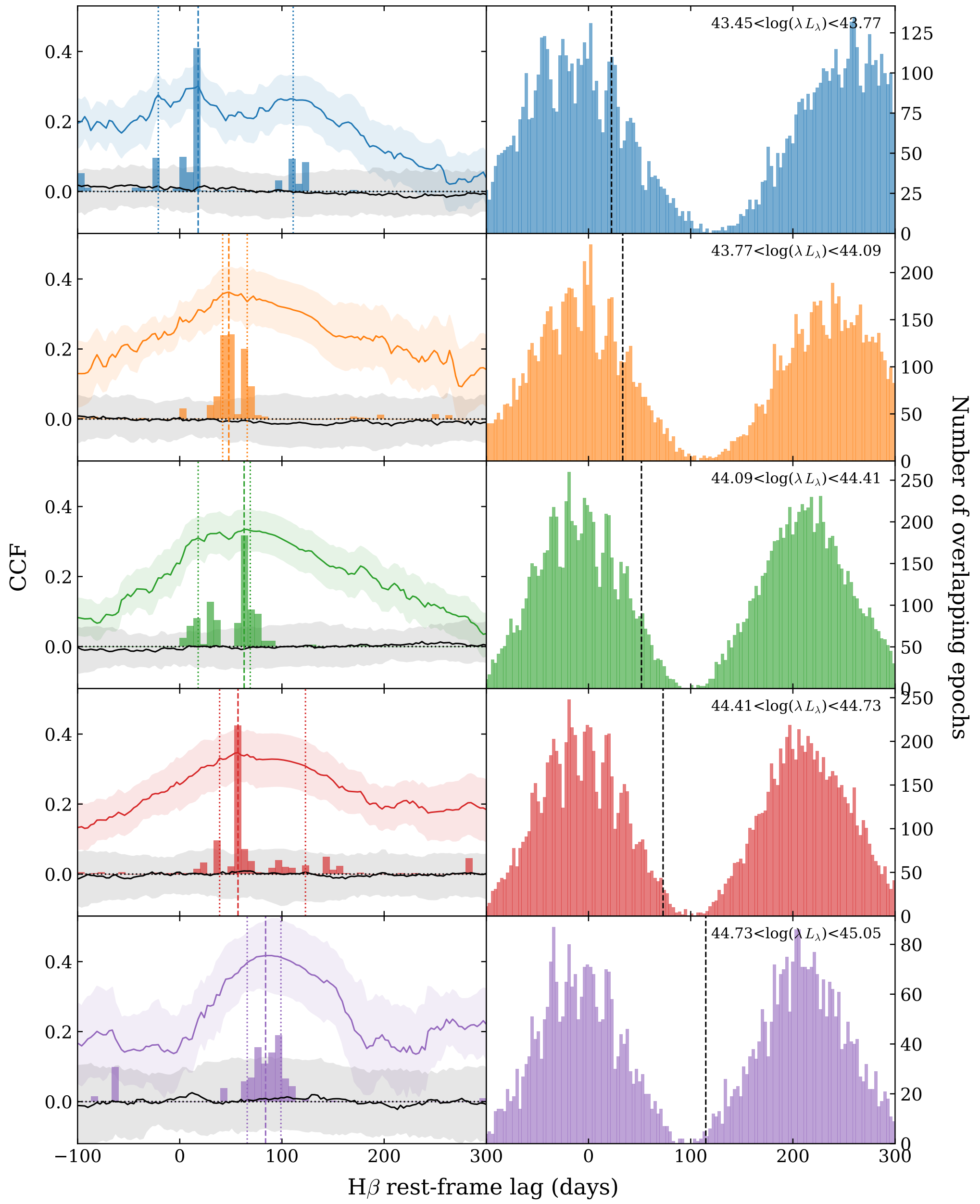

Figure 4.14: The same as Figure 4.3 after excluding sources with individual lag recoveries from the stacked sample.

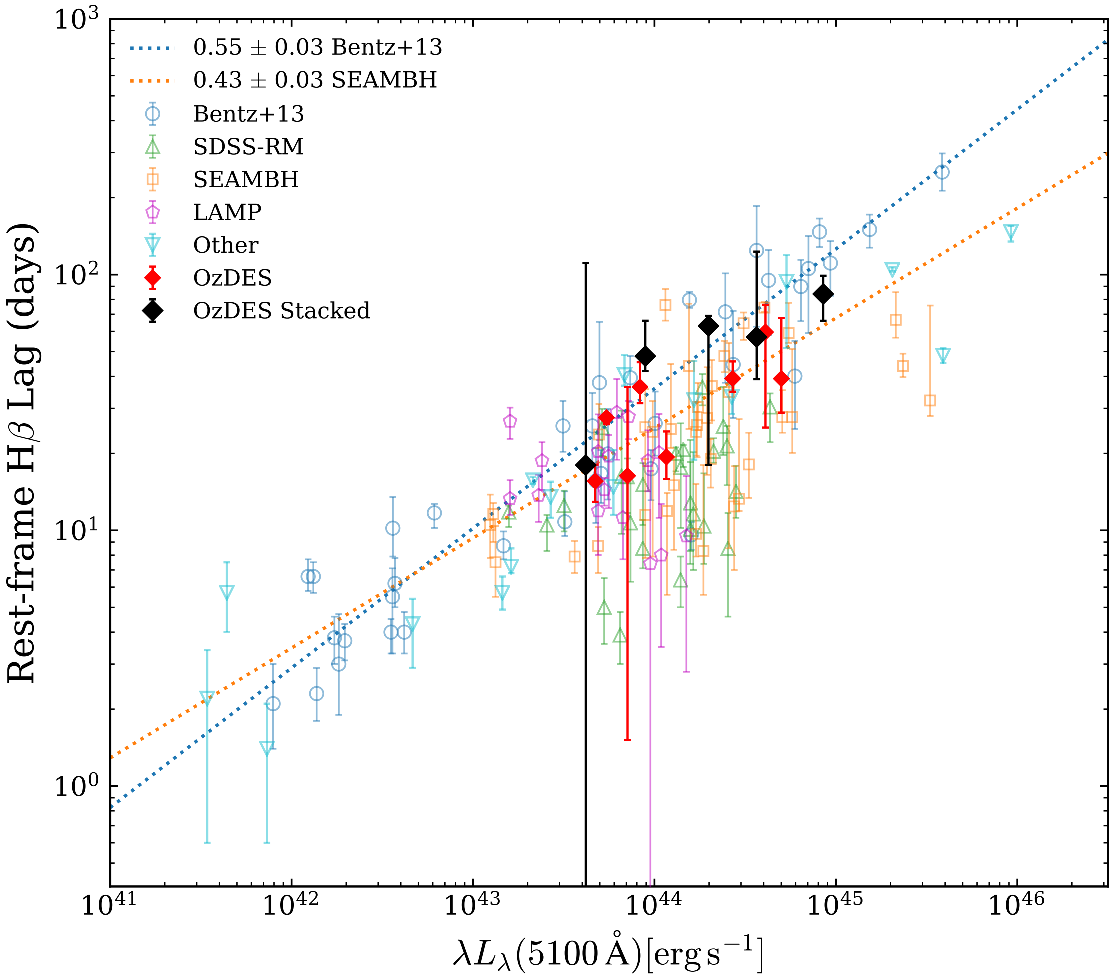

Figure 4.15: The Radius-Luminosity relation for Hβ (dotted lines), including the stacked average lag measurements made using the OzDES Hβ sample after excluding sources with individual lag recoveries, and existing individual lag measurements (same as in Figure 4.4).

5

Conclusion

Reverberation mapping is the only black hole mass measurement method that can be applied outside the local Universe, however, it is an observationally expensive endeavour. Although the earliest RM campaigns began in the 1980's, it is for this reason that RM measurements have remained limited in many respects, until recently. Over the last decade, the first multi-object RM surveys have been undertaken with the primary objective of probing a wider range of AGN properties and recovering more reliable RM measurements and BH masses. In this thesis, I have explored the complexities of scaling up the traditional reverberation mapping technique for application through MOS surveys. In Chapter 2, I conducted comprehensive simulations to probe the effect of each component of the observational window function on the overall efficacy of MOS-RM surveys. In Chapter 3, I recovered Hβ lags from one of the first MOS-RM surveys: the OzDES RM Program. In Chapter 4, I used a novel stacking method to recover average lags across the bulk of the OzDES RM AGN sample. Here I summarise these chapters and highlight the key takeaways from each project, and how it connects to the wider field of RM and AGN research. I then discuss the next frontiers of future research stemming from this work, and conclude with some final remarks on this thesis.

5.1 Observational window effects on multi-object reverberation mapping

In Chapter 2, I investigated the impact of survey design on the efficacy of MOS-RM surveys. Whereas early, traditional RM surveys had dedicated monitoring of select individual objects, scaling this method up to samples of hundreds of AGN is complicated, as each object has a unique reverberation lag, variability time-scales, and redshift-dependent time-dilation. Given all sources are sampled through the same observational window, it is challenging to monitor each satisfactorily to achieve robust lag recovery.

Although the first generation of MOS-RM surveys did use simulations to forecast their lag recovery efficacy, they only tested a limited range of design modifications; most of which conformed to existing survey restrictions (often dictated by other science programs). I conducted exhaustive simulations varying each component of the global observation window function for MOS-RM surveys: the cadence, seasonal length and baseline. I identified the seasonal length as the key factor limiting the efficacy of the contemporaneous OzDES RM and SDSS-RM surveys. These findings emphasise the importance of prioritising observing fields with longer seasonal visibility in MOS-RM surveys. This not only recovers lags for a greater number of sources but also helps to mitigate signal aliasing, thus improving lag reliability and reducing scatter in the $R-L$ relation. I found that sources with long variability timescales may be less affected by seasonal gaps, although extended baseline monitoring remains crucial in such cases.

In cases where the sampling window cannot be improved, careful optimisation of target source lists will likely yield higher survey efficacies. By using a multi-tiered observing strategy future surveys can allocate their limited observational resources more effectively, to optimise lag recovery for diverse classes of objects. Additionally, extending the wavelength range of spectrographs to the near-infrared is crucial for conducting joint emission-line lag analyses. This expansion in wavelength coverage will allow us to examine the consistency of virial BH masses obtained with multiple emission lines.

In this work I have highlighted the importance of extending the seasonal visibility of survey fields, optimising target selection, and extending wavelength coverage. The insights gained from this work will inform future MOS-RM survey designs and improve our ability to measure more, reliable reverberation lags in AGN.

5.2 OzDES Reverberation Mapping Program: Hβ lags from the 6-year survey

In Chapter 3, I recovered lags from the Hβ sample monitored by the OzDES RM Program, which conducted one of the first MOS-RM surveys. This 6-year survey was primarily designed to recover lags for higher-redshift sources accessible with the Mg II and C IV lines; a regime which lacked RM measurements. However, recovering lags from the Hβ sample was essential as most RM measurements had only been made using this line, which OzDES needed as a point of comparison. In light of the findings from the previous chapter, I was aware that it would be challenging to recover the shorter lags expected for the Hβ sample as the observational window was less than ideal.

I used two lag recovery methods to successfully recover lags for eight AGN from the OzDES RM Hβ sample. I found that these results were consistent with the sample of measurements made by earlier traditional RM surveys, which observed AGN with dedicated monitoring on a source-by-source basis (Grier et al. 2013a). The OzDES results were also consistent with the observed dependence of lags on source accretion rate. Interestingly, the OzDES results appear inconsistent with those from the SDSS-RM Hβ sample (Grier et al. 2017), which conducted a similar MOS-RM survey, likely due to the limited baseline of their Y1 data.

Given the modest signal-to-noise and sampling of the OzDES data, some of our recoveries are not as robust as the existing sample. I emphasise that additional observations at higher cadence and over a longer observing season are required to recover higher quality lags for these sources. Given the TiDES and SDSS-V BHM programs will be observing some of the same fields (Swann et al. 2019; Kollmeier et al. 2017), they can improve upon the results presented here. I also emphasise the importance for future surveys to extend the dynamic range in luminosity of Hβ measurements, which calibrate this important $R - L$ relation.

I successfully recovered lags and measured BH masses for eight AGN at $0.12 < z < 0.71$ from the OzDES Hβ sample, which are notably at higher redshifts than the bulk of existing measurements with this emission line. This work complements the lag recovery effort for the rest of the OzDES RM sample, with the Mg II and C IV emission lines (Hoormann et al. 2019; Yu et al. 2021; Penton et al. 2022; Yu et al. 2023). These results contribute to the ongoing efforts to refine BH mass-scaling relations. This work further highlights the impact of the observational window function and the need for improved survey designs.

5.3 OzDES Reverberation Mapping Program: Stacking analysis with Hβ, Mg II and C IV

In Chapter 4, I perform a stacking analysis to recover average lags across the bulk of the OzDES RM sample. This technique was developed by Fine et al. (2012, 2013) to maximise the information extracted from large AGN samples that lacked sufficient spectroscopic epochs to recover individual lags. As elucidated in the preceding chapters, the observational window of the OzDES RM Program has significantly impeded the effectiveness of lag recovery for individual lags, resulting in an overall survey efficacy of only $\sim 10\%$.

I used the stacking technique to measure average reverberation lags using the Hβ, Mg II, and C IV lines across the redshift-luminosity regime probed by the full OzDES RM AGN sample. Stacking circumvents the selection biases present in the lag recovery for individual sources, and is able to partially overcome the gaps in the observational window. I recover significant average lags in each luminosity bin for the Hβ sample, which are consistent with the Bentz et al. (2013) $R-L$ relation, and have low scatter and small uncertainties; signalling their potential to provide better constraints on the $R-L$ relation. For the Mg II and C IV samples, there is significant signal in the stacked cross-correlations, however, the data quality was insufficient to recover well-constrained average lags. The findings from the multi-line analysis are broadly consistent with the BLR ionisation stratification model.

The forthcoming large time-domain surveys, including LSST, SDSS-V BHM and TiDES, will increase the AGN sample size and improve the spectroscopic signal-to-noise. However, as demonstrated in Chapter 2, they will likely remain affected by inevitable seasonal gaps. This may have been a contributing factor to the large scatter in the RM measurements made by OzDES and SDSS-RM, particularly for C IV. With improved data quality, and the potential to combine these large datasets, future stacking analyses could concentrate this information to produce robust average lag measurements that supplement or surpass efforts using traditional individual measurements.

In this work I recovered average lags across the entire OzDES RM sample by utilising a stacking analysis, to supplement the individual lag recovery effort. The most significant results, for the Hβ sample, demonstrate potential to facilitate better constraints on the $R-L$ relation. These results demonstrate that individual source measurements can be complemented and strengthened by the statistical power provided by stacking techniques.

5.4 Future Work

5.4.1 More from the OzDES RM Program and DES

The lag recovery effort using the full program data from the OzDES RM Program has almost been completed for each emission-line sample. The survey has recovered 62 new reverberation lags and BH masses for AGN at $0.1< z <2.8$. This is comparable to the total number of RM measurements that existed at the time of the program's commencement. This includes 8 measurements with Hβ (Chapter 3, Malik et al. 2023), 25 with Mg II (Yu et al. 2021, 2023) and 29 with C IV (Hoormann et al. 2019;

Penton et al. 2022, Penton et al. in prep).

These measurements will be combined with the latest results from SDSS-RM (Shen et al. 2023) and the existing sample of RM lags, which will be used to constrain updated $R - L$ relations for each emission line. Following this, OzDES will pursue the main science goals of the program: measuring single-epoch virial BH masses to infer the BH mass function, and testing the application of AGN as a high-redshift standardisable candle.

There are further avenues of science beyond these key goals, which can be facilitated by this rich dataset. The high-quality, multi-band photometric light curves obtained by DES have been used to conduct continuum RM to measure accretion disk sizes (Mudd et al. 2018; Yu et al. 2020a). This can be applied to the full 7-year light curves available for each of the DES SN fields. This data has also been combined with other legacy data in these fields to produce photometric light curves with a 20-year baseline, which were used to revisit the DRW variability model in AGN (Stone et al. 2022a).

5.4.2 Second-generation of MOS-RM

As we enter the era of time-domain astronomy, there are several upcoming surveys that plan to conduct MOS-RM. These surveys will build upon the achievements of the first-generation MOS-RM programs undertaken by OzDES and SDSS-RM. The SDSS-V Black Hole Mapper, which began in 2021, is conducting a spectroscopic RM program in both the northern and southern hemispheres (Fries et al. 2023). Between the two observatories, it is targeting the four LSST deep-drilling fields, and continuing monitoring of the SDSS-RM field. Across these fields, the BHM RM program is targeting $\sim$ 1000 AGN (Kollmeier et al. 2017). With LSST to commence late 2024, high cadence photometry of the four deep-drilling fields will yield continuum light curves for thousands of AGN. The Time Domain Extragalactic Survey (TiDES) will begin spectroscopic follow-up of these deep-drilling fields in 2024 as part of its 5-year RM program targeting $\sim$ 700 AGN up to $z \sim 2.5$ (Swann et al. 2019).

This work has repeatedly demonstrated the importance for these surveys to consider the impact of their observational window on reverberation lag recovery. The observation strategies for LSST and TiDES are not yet confirmed, however the SDSS-V BHM RM program RM has obtained approximately 5-7 epochs per month over a 5-7 month season each year (Almeida et al. 2023). This is the maximum length where the respective field is visible for at least 2 hours below an airmass of 1.4. As demonstrated in this work, these large seasonal gaps will reduce lag recovery efficacy and reliability.

5.4.3 SMBH masses in the ELT era

An overview of the available SMBH mass measurement methods was given in Section 1.2. Presently, RM is the only method which can be used to measure BH masses beyond $z \sim 0.2$. In the upcoming era of extremely large telescopes, including the Giant Magellan Telescope (GMT) and European Extremely Large Telescope (E-ELT), these large apertures (> 25m), aided by adaptive optics, should achieve 10 mas angular resolution or better (Johns et al. 2012). If sufficient sensitivity can be achieved, these facilities will allow measurement of stellar and gas dynamical SMBH masses out to $z \sim 10$ or beyond (GMT Science Advisory Committee 2018; Gültekin et al. 2019). However, these high redshift measurements will be very observationally intensive, therefore MOS-RM will be necessary to complement these efforts in order to increase the sample of SMBH masses, and improve calibration of single-epoch virial BH mass estimators for survey-wide application.

5.5 Final remarks

Multiplexed spectroscopy and wide-field photometry have enabled the traditionally resource-intensive RM method to be performed more efficiently and with improved synergy with other science programs. As a result, the first generation of MOS-RM surveys have more than tripled the total number of RM measurements. However, the scaling up of RM to this industrial scale has not been without its challenges.

In this thesis, I measured new lags and BH masses using the full program data obtained by the OzDES RM Program. However, the less-than-ideal observational window of the survey limited the overall lag recovery efficacy. In light of this, I explored how the design of MOS-RM surveys can optimised to better capture AGN variability in order to facilitate more, reliable lag measurements. To compensate for the limitations of the OzDES data, I used a stacking analysis to leverage the bulk AGN sample in order to extract the maximum information from our data.

Reverberation mapping will remain an observationally expensive endeavour, but one that is necessary to extend direct BH mass measurements to the furthest reaches of the Universe. I hope the insights from this work will inform the design of future MOS-RM surveys, so that we can unlock the full, unmatched potential of RM to reveal the nature of supermassive black holes and their environments.

Bibliography

Abbott T. M. C., et al., 2019, ApJ, 872, L30

Akritas M. G., Bershady M. A., 1996, ApJ, 470, 706

Almeida A., et al., 2023, arXiv e-prints, p. arXiv:2301.07688

Antonucci R., 1993, ARA&A, 31, 473

Astropy Collaboration et al., 2013, A&A, 558, A33

Astropy Collaboration et al., 2018, AJ, 156, 123

Bañados E., et al., 2018, Nature, 553, 473

Balbus S. A., Hawley J. F., 1991, ApJ, 376, 214

Barth A. J., et al., 2013, ApJ, 769, 128

Bentz M. C., Katz S., 2015, PASP, 127, 67

Bentz M. C., Peterson B. M., Pogge R. W., Vestergaard M., Onken C. A., 2006, ApJ, 644, 133

Bentz M. C., Peterson B. M., Netzer H., Pogge R. W., Vestergaard M., 2009, ApJ, 697, 160

Bentz M. C., et al., 2010, ApJ, 720, L46

Bentz M. C., et al., 2013, ApJ, 767, 149

Bentz M. C., et al., 2014, ApJ, 796, 8

Bentz M. C., Cackett E. M., Crenshaw D. M., Horne K., Street R., Ou-Yang B., 2016a, ApJ, 830, 136

Bentz M. C., et al., 2016b, ApJ, 831, 2

Blandford R. D., McKee C. F., 1982, ApJ, 255, 419

Brandt W. N., et al., 2018, arXiv e-prints, p. arXiv:1811.06542

Brewer B. J., et al., 2011, ApJ, 733, L33

Burke D. L., et al., 2018, AJ, 155, 41

Cackett E. M., Bentz M. C., Kara E., 2021, iScience, 24, 102557

Cappellari M., Verolme E. K., van der Marel R. P., Verdoes Kleijn G. A., Illingworth G. D., Franx M., Carollo C. M., de Zeeuw P. T., 2002, ApJ, 578, 787

Childress M. J., et al., 2017, MNRAS, 472, 273

Clavel J., et al., 1991, ApJ, 366, 64

Czerny B., et al., 2019, ApJ, 880, 46

Dark Energy Survey Collaboration et al., 2016, MNRAS, 460, 1270

Davidson K., 1972, ApJ, 171, 213

De Rosa G., et al., 2015, ApJ, 806, 128

Dehghanian M., et al., 2019a, ApJ, 877, 119

Dehghanian M., et al., 2019b, ApJ, 882, L30

Diehl H. T., et al., 2018, in Observatory Operations: Strategies, Processes, and Systems VII. p. 107040D, doi:10.1117/12.2312113

Dietrich M., et al., 1993, ApJ, 408, 416

Du P., et al., 2014, ApJ, 782, 45

Du P., et al., 2015, ApJ, 806, 22

Du P., et al., 2016, ApJ, 825, 126

Du P., et al., 2018, ApJ, 856, 6

Event Horizon Telescope Collaboration et al., 2019, ApJ, 875, L6

Event Horizon Telescope Collaboration et al., 2022, ApJ, 930, L15

Fabian A. C., 2012, ARA&A, 50, 455

Fausnaugh M. M., et al., 2017, ApJ, 840, 97

Ferrarese L., Ford H., 2005, Space Sci. Rev., 116, 523

Ferrarese L., Merritt D., 2000, ApJ, 539, L9

Fine S., et al., 2012, MNRAS, 427, 2701

Fine S., et al., 2013, MNRAS, 434, L16

Flaugher B., et al., 2015, AJ, 150, 150

Fonseca Alvarez G., et al., 2020, ApJ, 899, 73

Fries L. B., et al., 2023, ApJ, 948, 5

GMT Science Advisory Committee 2018, Giant Magellan Telescope Science Book

GRAVITY Collaboration et al., 2020, A&A, 643, A154

Gaskell C. M., Peterson B. M., 1987, ApJS, 65, 1

Gaskell C. M., Sparke L. S., 1986, ApJ, 305, 175

Gebhardt K., Thomas J., 2009, ApJ, 700, 1690

Gebhardt K., et al., 2000a, ApJ, 543, L5

Gebhardt K., et al., 2000b, ApJ, 543, L5

Gebhardt K., Adams J., Richstone D., Lauer T. R., Faber S. M., Gültekin K., Murphy J., Tremaine S., 2011, ApJ, 729, 119

Genzel R., Eisenhauer F., Gillessen S., 2010, Reviews of Modern Physics, 82, 3121

Gerhard O. E., 1993, MNRAS, 265, 213

Ghez A. M., et al., 2008, ApJ, 689, 1044

Goad M. R., et al., 2016, ApJ, 824, 11

Gravity Collaboration et al., 2018, Nature, 563, 657

Greene J. E., et al., 2010, ApJ, 721, 26

Greenhill L. J., et al., 2003, ApJ, 590, 162

Grier C. J., et al., 2013a, ApJ, 764, 47

Grier C. J., et al., 2013b, ApJ, 773, 90

Grier C. J., et al., 2017, ApJ, 851, 21

Grier C. J., et al., 2019, ApJ, 887, 38

Gültekin K., et al., 2019, arXiv e-prints, p. arXiv:1904.01447

Harms R. J., et al., 1994, ApJ, 435, L35

Harris C. R., et al., 2020, Nature, 585, 357

Homayouni Y., et al., 2020, ApJ, 901, 55

Hoormann J. K., et al., 2019, MNRAS, 487, 3650

Horne K., Peterson B. M., Collier S. J., Netzer H., 2004, PASP, 116, 465

Horne K., et al., 2021, ApJ, 907, 76

Hoyle F., Fowler W. A., 1963, MNRAS, 125, 169

Hu C., et al., 2021, ApJS, 253, 20

Hunter J. D., 2007, Computing in Science & Engineering, 9, 90

Inayoshi K., Visbal E., Haiman Z., 2020, ARA&A, 58, 27

Johns M., et al., 2012, in Stepp L. M., Gilmozzi R., Hall H. J., eds, Society of Photo-Optical Instrumentation Engineers (SPIE) Conference Series Vol. 8444, Ground-based and Airborne Telescopes IV. p. 84441H, doi:10.1117/12.926716

Kasliwal V. P., Vogeley M. S., Richards G. T., Williams J., Carini M. T., 2015, MNRAS, 453, 2075

Kaspi S., Smith P. S., Netzer H., Maoz D., Jannuzi B. T., Giveon U., 2000, ApJ, 533, 631

Kaspi S., Brandt W. N., Maoz D., Netzer H., Schneider D. P., Shemmer O., 2007, ApJ, 659, 997

Kaspi S., Brandt W. N., Maoz D., Netzer H., Schneider D. P., Shemmer O., Grier C. J., 2021, ApJ, 915, 129

Kelly B. C., Shen Y., 2013, ApJ, 764, 45

Kelly B. C., Bechtold J., Siemiginowska A., 2009, ApJ, 698, 895

Kessler R., et al., 2015, AJ, 150, 172

Khadka N., Martínez-Aldama M. L., Zajaček M., Czerny B., Ratra B., 2022, MNRAS, 513, 1985

King A., 2003, ApJ, 596, L27

King A. L., Davis T. M., Denney K. D., Vestergaard M., Watson D., 2014, MNRAS, 441, 3454

King A. L., et al., 2015, MNRAS, 453, 1701

Kollmeier J. A., et al., 2017, arXiv e-prints, p. arXiv:1711.03234

Kormendy J., Ho L. C., 2013, ARA&A, 51, 511

Kormendy J., Richstone D., 1995, ARA&A, 33, 581

Kozłowski S., et al., 2010, ApJ, 708, 927

Kuo C. Y., et al., 2011, ApJ, 727, 20

Lewis I. J., et al., 2002, MNRAS, 333, 279

Li J., et al., 2017, ApJ, 846, 79

Li J. I.-H., et al., 2019, ApJ, 884, 119

Li S.-S., et al., 2021, ApJ, 920, 9

Lidman C., et al., 2020, MNRAS, 496, 19

Lira P., et al., 2018, ApJ, 865, 56

Lu K.-X., et al., 2016, ApJ, 827, 118

Lynden-Bell D., 1969, Nature, 223, 690

MacLeod C. L., et al., 2010, ApJ, 721, 1014

Magorrian J., et al., 1998, AJ, 115, 2285

Malik U., et al., 2022, MNRAS, 516, 3238

Malik U., et al., 2023, MNRAS, 520, 2009

Martínez-Aldama M. L., Czerny B., Kawka D., Karas V., Panda S., Zajaček M., Życki P. T., 2019, ApJ, 883, 170

Matthews T. A., Sandage A. R., 1963, ApJ, 138, 30

McConnell N. J., Ma C.-P., 2013, ApJ, 764, 184

McHardy I., 1988, Mem. Soc. Astron. Italiana, 59, 239

McLure R. J., Jarvis M. J., 2002, MNRAS, 337, 109

McMahon R. G., Banerji M., Gonzalez E., Koposov S. E., Bejar V. J., Lodieu N., Rebolo R., VHS Collaboration 2013, The Messenger, 154, 35

Metzroth K. G., Onken C. A., Peterson B. M., 2006, ApJ, 647, 901

Miyoshi M., Moran J., Herrnstein J., Greenhill L., Nakai N., Diamond P., Inoue M., 1995, Nature, 373, 127

Morganson E., et al., 2018, PASP, 130, 074501

Mudd D., et al., 2018, ApJ, 862, 123

Mushotzky R. F., Done C., Pounds K. A., 1993, ARA&A, 31, 717

Mushotzky R. F., Edelson R., Baumgartner W., Gandhi P., 2011, ApJ, 743, L12

Nemmen R. S., Georganopoulos M., Guiriec S., Meyer E. T., Gehrels N., Sambruna R. M., 2012, Science, 338, 1445

Netzer H., 2015, ARA&A, 53, 365

Onken C. A., Kollmeier J. A., 2008, ApJ, 689, L13

Onken C. A., Ferrarese L., Merritt D., Peterson B. M., Pogge R. W., Vestergaard M., Wandel A., 2004, ApJ, 615, 645

Onken C. A., et al., 2014, ApJ, 791, 37

Pancoast A., Brewer B. J., Treu T., 2011, ApJ, 730, 139

Pancoast A., Brewer B. J., Treu T., 2014a, MNRAS, 445, 3055

Pancoast A., Brewer B. J., Treu T., Park D., Barth A. J., Bentz M. C., Woo J.-H., 2014b, MNRAS, 445, 3073

Park D., Kelly B. C., Woo J.-H., Treu T., 2012, ApJS, 203, 6

Pei L., et al., 2014, ApJ, 795, 38

Penton A., et al., 2022, MNRAS, 509, 4008

Perlmutter S., et al., 1999, ApJ, 517, 565

Peters C. M., et al., 2015, ApJ, 811, 95

Peterson B. M., 1993, PASP, 105, 247

Peterson B. M., 1997, An Introduction to Active Galactic Nuclei

Peterson B. M., 2001, in Aretxaga I., Kunth D., Mújica R., eds, Advanced Lectures on the Starburst-AGN. p. 3 (arXiv:astro-ph/0109495), doi:10.1142/9789812811318˙0002

Peterson B. M., Horne K., 2004, Astronomische Nachrichten, 325, 248

Peterson B. M., Wanders I., Horne K., Collier S., Alexander T., Kaspi S., Maoz D., 1998, PASP, 110, 660

Peterson B. M., et al., 2005, ApJ, 632, 799

Pritchet C. J., Howell D. A., Sullivan M., 2008, ApJ, 683, L25

Rakshit S., et al., 2019, ApJ, 886, 93

Rees M. J., 1984, ARA&A, 22, 471

Riess A. G., et al., 1998, AJ, 116, 1009

Riess A. G., et al., 2004, ApJ, 607, 665

Riess A. G., et al., 2011, ApJ, 730, 119

Saglia R. P., et al., 2016, ApJ, 818, 47

Salpeter E. E., 1964, ApJ, 140, 796

Schmidt M., 1963, Nature, 197, 1040

Schwarzschild M., 1979, ApJ, 232, 236

Scolnic D., et al., 2022, ApJ, 938, 113

Seyfert C. K., 1943, ApJ, 97, 28

Shakura N. I., Sunyaev R. A., 1973, A&A, 24, 337

Sharp R., et al., 2006, in McLean I. S., Iye M., eds, Society of Photo-Optical Instrumentation Engineers (SPIE) Conference Series Vol. 6269, Society of Photo-Optical Instrumentation Engineers (SPIE) Conference Series. SPIE, p. 62690G (`arXiv:astro-ph/0606137`), doi:10.1117/12.671022

Shen Y., 2013, Bulletin of the Astronomical Society of India, 41, 61

Shen Y., Greene J. E., Strauss M. A., Richards G. T., Schneider D. P., 2008, ApJ, 680, 169

Shen Y., et al., 2011, ApJS, 194, 45

Shen Y., et al., 2015, ApJS, 216, 4

Shen Y., et al., 2019a, ApJS, 241, 34

Shen Y., et al., 2019b, ApJ, 883, L14

Shen Y., et al., 2023, arXiv e-prints, p. arXiv:2305.01014

Silk J., Rees M. J., 1998, A&A, 331, L1

Smith K. L., Mushotzky R. F., Boyd P. T., Malkan M., Howell S. B., Gelino D. M., 2018, ApJ, 857, 141

Stone Z., et al., 2022a, arXiv e-prints, p. arXiv:2201.02762

Stone Z., et al., 2022b, MNRAS, 514, 164

Sun M., Grier C. J., Peterson B. M., 2018, PyCCF: Python Cross Correlation Function for reverberation mapping studies (ascl:1805.032)

Swann E., et al., 2019, The Messenger, 175, 58

Tang J.-J., Wolf C., Tonry J., 2023, arXiv e-prints, p. arXiv:2301.01304

The MSE Science Team et al., 2019, arXiv e-prints, p. arXiv:1904.04907

Tie S. S., et al., 2017, AJ, 153, 107

Trakhtenbrot B., Netzer H., 2012, MNRAS, 427, 3081

Tremaine S., et al., 2002, ApJ, 574, 740

Trevese D., Perna M., Vagnetti F., Saturni F. G., Dadina M., 2014, ApJ, 795, 164

U V., et al., 2022, ApJ, 925, 52

Urry C. M., Padovani P., 1995, PASP, 107, 803

Vanden Berk D. E., et al., 2001, AJ, 122, 549

Vestergaard M., 2002, ApJ, 571, 733

Vestergaard M., Peterson B. M., 2006, ApJ, 641, 689

Virtanen P., et al., 2020, Nature Methods, 17, 261

Wandel A., Peterson B. M., Malkan M. A., 1999, ApJ, 526, 579

Wang J.-M., et al., 2014a, ApJ, 793, 108

Wang J.-M., Qiu J., Du P., Ho L. C., 2014b, ApJ, 797, 65

Wang F., et al., 2021, ApJ, 907, L1

Waskom M. L., 2021, Journal of Open Source Software, 6, 3021

Watson D., Denney K. D., Vestergaard M., Davis T. M., 2011, ApJ, 740, L49

Welsh W. F., 1999, PASP, 111, 1347

White R. J., Peterson B. M., 1994, PASP, 106, 879

Woo J.-H., et al., 2010, ApJ, 716, 269

Woo J.-H., Yoon Y., Park S., Park D., Kim S. C., 2015, ApJ, 801, 38

Woo J.-H., Le H. A. N., Karouzos M., Park D., Park D., Malkan M. A., Treu T., Bennert V. N., 2018, ApJ, 859, 138

Wright E. L., et al., 2010, AJ, 140, 1868

Wu Q., Shen Y., 2022, ApJS, 263, 42

Yu Z., et al., 2020a, ApJS, 246, 16

Yu Z., Kochanek C. S., Peterson B. M., Zu Y., Brandt W. N., Cackett E. M., Fausnaugh M. M., McHardy I. M., 2020b, MNRAS, 491, 6045

Yu Z., et al., 2021, MNRAS, 507, 3771

Yu Z., et al., 2023, MNRAS, 522, 4132

Yuan F., et al., 2015, MNRAS, 452, 3047

Zajaček M., et al., 2020, ApJ, 896, 146

Zajaček M., et al., 2021, ApJ, 912, 10

Zel'dovich Y. B., 1964, Soviet Physics Doklady, 9, 195

Zhang Z.-X., et al., 2019, ApJ, 876, 49

Zu Y., Kochanek C. S., Peterson B. M., 2011, ApJ, 735, 80

Zu Y., Kochanek C. S., Kozłowski S., Udalski A., 2013, ApJ, 765, 106

de Jong R. S., et al., 2019, The Messenger, 175, 3

den Brok M., et al., 2015, ApJ, 809, 101

Appendix

Appendix

This appendix contains supplementary material to the work presented in Chapter 4.

A Source properties

The source properties are given for the Hβ sample of 69 AGN in Table A1, the Mg II sample of 450 AGN in Table A2, and the C IV sample of 290 AGN in Table A3.

Table A1: Properties for our OzDES Hβ stacking sample. Columns left to right: DES name (J2000), redshift, r-band apparent AB magnitude, monochromatic luminosity at 5100Å. The superscript a flags sources which also have Mg II data.

DES ID	z	m_r	$\log(\lambda L_{5100})$ (erg s^{-1})
DES J002802.42-424913.52	0.127	17.88	43.67
DES J033633.16-284027.18	0.129	17.73	43.74
DES J022024.92-061731.51	0.139	18.04	43.69
DES J003515.60-433357.64	0.145	17.75	43.84
DES J003245.59-421441.67	0.183	18.85	43.62
DES J025007.02+002525.49	0.198	18.02	44.03
DES J024347.34-005354.84	0.237	19.19	43.73
DES J024340.97-002601.16	0.268	19.16	43.86
DES J025021.72-005413.02	0.271	19.87	43.59
DES J025211.61-003629.35	0.294	20.10	43.58
DES J034028.46-292902.41	0.310	18.09	44.43
DES J022249.67-051453.01	0.314	19.03	44.07
DES J025240.59-002117.04	0.315	20.37	43.53
DES J022851.50-051223.00	0.317	18.01	44.48
DES J003954.13-440509.97	0.332	19.53	43.92
DES J022330.16-054758.06	0.354	19.87	43.85
DES J024325.53-000412.67	0.356	20.47	43.62
DES J024902.03-004322.43	0.360	20.75	43.52
DES J024320.36-001825.41	0.373	19.47	44.07
DES J024519.82-010245.63	0.381	20.46	43.69
DES J024225.86-004142.50	0.383	20.74	43.59
DES J003622.82-424759.11	0.390	21.02	43.49
DES J004009.06-431255.29	0.434	19.04	44.40
DES J003834.47-433807.12	0.453	20.61	43.82
DES J025042.90-004138.74	0.457	20.54	43.86
DES J022258.90-045852.28	0.466	19.77	44.20
DES J024712.89-011106.21	0.486	20.56	43.92
DES J024211.93-010959.69	0.488	20.18	44.08
DES J024538.29-004705.32	0.488	20.49	43.96
DES J003017.47-422446.39	0.491	18.48	44.77
DES J022133.82-054842.69	0.501	18.77	44.67
DES J024643.04-013149.55	0.502	19.32	44.45
DES J033002.93-273248.31	0.527	20.33	44.10
DES J003552.21-423352.14	0.530	21.29	43.72
DES J022019.61-060729.77	0.541	20.07	44.23
DES J021910.57-055114.76	0.558	19.49	44.49
DES J025119.79-004831.62	0.559	19.98	44.30
DES J033758.00-294618.46	0.561	19.27	44.58
DES J024939.57+000700.39	0.564	20.90	43.94
DES J024646.73-001220.60	0.564	19.73	44.41
DES J022717.88-051623.78	0.566	20.87	43.95

Table A1: Hβ sample

DES ID	z	m_r	$\log(\lambda L_{5100})$ (erg s^{-1})
DES J033946.12-295030.94	0.582	20.33	44.20
DES J003114.43-424227.81	0.591	20.53	44.13
DES J033905.07-292134.36	0.600	18.66	44.89
DES J022329.27-045451.85	0.604	20.78	44.05
DES J033738.50-272306.75	0.613	18.60	44.94
DES J022246.23-041450.67	0.614	19.94	44.40
DES J024651.86-010732.56	0.622	20.36	44.25
DES J033910.13-264311.77	0.622	21.39	43.84
DES J024442.77-004223.14	0.628	19.92	44.43
DES J021923.29-045148.69	0.630	19.36	44.66
DES J033051.45-271254.90	0.633	20.24	44.31
DES J032718.70-281857.85	0.634	19.52	44.60
DES J002904.43-425243.04	0.644	19.54	44.61
DES J021820.49-050426.42	0.650	19.59	44.60
DES J034056.37-293339.67	0.652	20.44	44.26
DES J003013.70-425733.44 [a]	0.654	20.31	44.32
DES J024533.65-000744.91 [a]	0.655	19.66	44.58
DES J003010.25-423356.22 [a]	0.667	20.14	44.40
DES J003231.39-433511.71 [a]	0.679	20.39	44.32
DES J004334.89-440546.53 [a]	0.681	19.62	44.63
DES J021952.14-040919.86 [a]	0.692	20.30	44.37
DES J022452.19-040519.38 [a]	0.695	19.85	44.55
DES J002906.71-423904.49 [a]	0.703	18.69	45.03
DES J021514.27-053321.33 [a]	0.703	20.01	44.50
DES J033819.34-274346.33 [a]	0.706	18.81	44.98
DES J022617.85-043108.99 [a]	0.708	19.52	44.70
DES J021524.99-045353.83 [a]	0.714	20.51	44.31
DES J021808.24-045845.20 [a]	0.716	18.18	45.25

Table A2: Properties for our OzDES Mg II stacking sample. Columns left to right: DES name (J2000), redshift, r-band apparent AB magnitude, monochromatic luminosity at 3000Å. The superscript a flags sources which also have Hβ data, and b flags sources which also have C IV data.

DES ID	z	m_r	$\log(\lambda L_{3000})$ (erg s^{-1})
DES J003013.70-425733.44 ^{a}	0.654	20.31	44.47
DES J024533.65-000744.91 ^{a}	0.655	19.66	44.73
DES J003010.25-423356.22 ^{a}	0.667	20.14	44.56
DES J003231.39-433511.71 ^{a}	0.679	20.39	44.47
DES J004334.89-440546.53 ^{a}	0.681	19.62	44.78
DES J021952.14-040919.86 ^{a}	0.692	20.30	44.53
DES J022452.19-040519.38 ^{a}	0.695	19.85	44.71
DES J002906.71-423904.49 ^{a}	0.703	18.69	45.18
DES J021514.27-053321.33 ^{a}	0.703	20.01	44.66
DES J033819.34-274346.33 ^{a}	0.706	18.81	45.14
DES J022617.85-043108.99 ^{a}	0.708	19.52	44.86
DES J021524.99-045353.83 ^{a}	0.714	20.51	44.47
DES J021808.24-045845.20 ^{a}	0.716	18.18	45.40
DES J033545.58-293216.49	0.724	20.30	44.56
DES J024126.71-004526.12	0.727	18.92	45.12
DES J033227.00-274105.28	0.730	19.81	44.77
DES J024727.97-013008.97	0.741	20.26	44.60
DES J022421.67-064613.71	0.755	20.48	44.53
DES J032724.94-274202.77	0.756	19.78	44.81
DES J021902.96-062107.22	0.758	20.42	44.55
DES J022244.40-043346.88	0.761	19.23	45.03
DES J025048.65+000207.62	0.766	19.12	45.08
DES J003155.93-434225.34	0.768	19.30	45.01
DES J021705.51-042253.46	0.788	20.24	44.66
DES J033459.10-293317.41	0.801	19.99	44.77
DES J032850.20-271207.84	0.802	19.42	45.00
DES J003350.95-435606.17	0.806	19.61	44.93
DES J022155.25-064916.59	0.807	18.06	45.55
DES J024801.09-004015.63	0.811	20.05	44.76
DES J025146.78-004035.49	0.813	19.63	44.93
DES J022326.46-045705.99	0.825	20.72	44.50
DES J025100.99+004802.99	0.829	20.03	44.78
DES J021628.43-040147.11	0.831	19.52	44.99
DES J033246.02-282232.12	0.839	20.07	44.78
DES J033328.93-275641.20	0.839	20.29	44.69
DES J022255.89-051351.61	0.849	19.01	45.21
DES J004042.70-440341.05	0.851	19.78	44.91
DES J033332.81-282220.34	0.858	19.14	45.17
DES J024637.94-004105.24	0.859	20.10	44.79
DES J033137.70-284808.03	0.862	21.68	44.16
DES J033230.63-284750.36	0.862	20.70	44.55

Table A2: Mg II sample

DES ID	z	m_r	$\log(\lambda L_{3000})$ (erg s^{-1})
DES J033235.64-290202.05	0.866	19.33	45.10
DES J003527.80-443411.36	0.869	19.90	44.88
DES J002831.10-421538.06	0.871	18.98	45.25
DES J033523.52-280723.67	0.871	17.25	45.94
DES J003331.34-441039.28	0.878	19.64	44.99
DES J004020.36-432053.98	0.880	19.49	45.05
DES J002641.26-424900.31	0.882	19.95	44.87
DES J021557.63-045009.52	0.884	18.73	45.36
DES J003301.72-440750.87	0.886	19.86	44.91
DES J024831.08-005025.58	0.887	20.42	44.69
DES J002951.05-433629.34	0.892	20.66	44.60
DES J002702.17-431755.99	0.900	20.15	44.81
DES J021413.01-042930.02	0.901	19.08	45.24
DES J024159.74-010512.38	0.904	20.16	44.81
DES J024357.90-011330.42	0.905	20.22	44.79
DES J022440.72-043657.71	0.907	20.14	44.82
DES J025217.48-005249.30	0.912	20.52	44.67
DES J002930.76-432724.34	0.914	18.35	45.54
DES J003437.73-424318.36	0.915	19.09	45.25
DES J033520.08-284258.52	0.931	20.14	44.84
DES J003435.26-441127.90	0.933	19.40	45.14
DES J024425.38-004652.99	0.937	18.90	45.34
DES J003809.48-435241.29	0.937	19.40	45.14
DES J033435.50-282812.24	0.940	19.88	44.95
DES J002926.51-431250.54	0.944	18.96	45.33
DES J002917.61-433759.92	0.951	18.58	45.48
DES J024237.79-012354.10	0.957	19.65	45.06
DES J033435.49-283631.56	0.963	20.09	44.89
DES J022049.53-053731.08	0.974	20.00	44.94
DES J022344.57-064039.01	0.983	20.83	44.61
DES J022712.98-044636.25	0.983	18.13	45.69
DES J033945.79-275333.88	0.984	21.29	44.43
DES J033404.10-275629.92	0.984	20.75	44.65
DES J033339.36-281724.26	0.987	20.02	44.94
DES J033509.98-283255.27	0.993	18.03	45.74
DES J002933.85-435240.66	0.995	18.06	45.73
DES J022114.78-050832.95	0.996	20.60	44.72
DES J032853.99-281706.94	1.000	20.29	44.84
DES J024514.00-003535.43	1.005	19.41	45.20
DES J025237.80-004627.79	1.008	19.49	45.17
DES J021500.22-043007.46	1.012	19.76	45.06
DES J024300.44-003030.10	1.018	20.52	44.76
DES J022449.86-043025.80	1.024	20.44	44.80
DES J024924.67+002536.38	1.025	19.93	45.00

Table A2: Mg II sample

DES ID	z	m_r	$\log(\lambda L_{3000})$ (erg s^{-1})
DES J033531.95-271825.19	1.029	19.14	45.32
DES J033408.25-274337.81	1.029	20.69	44.70
DES J003914.17-443844.22	1.033	19.62	45.13
DES J033854.56-291001.97	1.049	20.21	44.91
DES J032831.40-285249.79	1.050	20.47	44.80
DES J022104.63-044239.89	1.052	20.25	44.89
DES J002826.18-433829.09	1.063	20.90	44.64
DES J003710.86-444048.06	1.067	18.53	45.59
DES J033810.75-275153.11	1.077	19.45	45.23
DES J033948.28-275438.98	1.077	17.51	46.01
DES J021817.44-045112.40	1.083	19.25	45.32
DES J002949.39-434806.73	1.088	19.29	45.31
DES J025228.55+003109.14	1.110	18.81	45.52
DES J025128.38+001144.60	1.117	20.17	44.98
DES J033045.54-284150.29	1.119	19.57	45.22
DES J003145.76-421747.61	1.129	19.38	45.30
DES J003834.04-432457.69	1.133	20.29	44.94
DES J034020.28-291750.48	1.135	18.28	45.75
DES J003536.95-443104.40	1.136	20.06	45.04
DES J002639.87-432307.71	1.139	19.58	45.23
DES J024617.07-000602.60	1.143	18.42	45.70
DES J003452.22-434613.99	1.146	20.77	44.76
DES J024854.80+001054.04	1.146	19.57	45.24
DES J033836.19-295113.53	1.148	20.95	44.69
DES J003444.53-433749.06	1.153	20.12	45.03
DES J021631.35-043207.93	1.155	19.74	45.18
DES J022501.68-040754.18	1.157	19.67	45.21
DES J003332.28-430526.16	1.159	18.53	45.67
DES J022718.54-053124.86	1.159	21.06	44.66
DES J033350.23-284244.42	1.161	21.12	44.63
DES J021849.86-035835.29	1.162	19.18	45.41
DES J033612.01-290152.96	1.164	19.58	45.25
DES J033353.02-283022.38	1.165	18.51	45.68
DES J033429.54-293904.49	1.167	20.57	44.86
DES J033416.89-274504.73	1.168	20.12	45.04
DES J033719.99-262418.84	1.169	19.56	45.27
DES J003725.23-431710.85	1.173	19.94	45.12
DES J022556.83-045853.05	1.180	21.09	44.66
DES J022823.19-041223.67	1.181	17.57	46.07
DES J022533.79-050801.95	1.183	18.40	45.74
DES J033744.23-262559.74	1.187	18.85	45.56
DES J025036.99-002408.04	1.195	20.68	44.84
DES J033335.92-264915.24	1.199	19.99	45.12
DES J024840.98-001228.80	1.199	19.11	45.47
DES J003848.77-434518.55	1.200	21.03	44.70

Table A2: Mg II sample

DES ID	z	m_r	$\log(\lambda L_{3000})$ (erg s^{-1})
DES J003549.87-424526.29	1.208	20.26	45.02
DES J033627.43-294149.95	1.218	18.59	45.69
DES J022212.40-061246.20	1.220	20.71	44.85
DES J022108.60-061753.21	1.225	20.00	45.13
DES J033534.69-283149.26	1.225	19.71	45.25
DES J022134.35-062941.64	1.228	20.71	44.85
DES J024544.78-004415.24	1.229	19.82	45.21
DES J022423.52-065001.40	1.229	20.15	45.08
DES J022023.48-064959.19	1.232	20.35	45.00
DES J033525.23-270200.72	1.233	19.31	45.42
DES J022055.16-060136.43	1.234	20.55	44.92
DES J003703.65-434759.50	1.236	19.87	45.20
DES J004111.46-441014.38	1.237	20.20	45.06
DES J033211.42-284323.98	1.237	21.86	44.40
DES J033928.30-291714.73	1.241	20.08	45.12
DES J003125.94-434743.50	1.243	20.25	45.05
DES J024918.24-001731.03	1.244	19.82	45.22
DES J021906.15-063000.89	1.250	20.12	45.10
DES J002743.35-425258.79	1.252	19.94	45.18
DES J033635.40-273427.02	1.254	20.17	45.09
DES J003322.53-442412.38	1.257	19.47	45.37
DES J022445.39-065556.80	1.261	21.11	44.72
DES J022115.87-062217.45	1.273	18.82	45.64
DES J024306.66-002531.29	1.279	20.36	45.03
DES J022245.85-041932.10	1.283	20.61	44.93
DES J034106.19-291410.86	1.287	21.20	44.70
DES J022529.40-050946.39	1.288	20.93	44.81
DES J024939.57-001157.73	1.295	20.97	44.80
DES J024621.09-000152.02	1.296	18.64	45.73
DES J021957.86-060534.66	1.296	20.74	44.89
DES J025323.64+000446.97	1.297	20.18	45.12
DES J022024.34-061401.95	1.297	21.31	44.66
DES J033911.64-290601.76	1.298	20.06	45.16
DES J025224.97+001308.30	1.300	20.68	44.92
DES J003819.73-443134.02	1.305	18.80	45.67
DES J024455.17-002501.41	1.308	19.29	45.48
DES J034032.74-270521.33	1.310	20.91	44.83
DES J024811.51-012609.51	1.313	19.29	45.48
DES J003639.49-430400.30	1.317	20.20	45.12
DES J033308.48-285832.12	1.318	19.72	45.31
DES J025005.69-004054.86	1.320	20.41	45.04
DES J033030.59-282135.43	1.322	18.89	45.65
DES J022024.93-053744.40	1.322	21.14	44.75
DES J003245.16-440451.51	1.323	20.84	44.87
DES J033216.20-273930.61	1.324	20.60	44.96

Table A2: Mg II sample

DES ID	z	m_r	$\log(\lambda L_{3000})$ (erg s^{-1})
DES J033525.44-265531.09	1.325	17.55	46.19
DES J033939.33-272454.08	1.325	19.19	45.53
DES J033303.99-271531.43	1.329	20.13	45.16
DES J033533.91-264847.02	1.330	20.25	45.11
DES J002855.47-434210.06	1.331	20.14	45.15
DES J024214.97-003131.71	1.332	19.93	45.24
DES J033057.32-284737.42	1.335	20.99	44.81
DES J033635.49-263735.76	1.336	19.99	45.22
DES J033824.55-263527.10	1.340	19.65	45.35
DES J024652.16-011242.95	1.340	19.44	45.44
DES J024326.61-002056.06	1.345	20.51	45.01
DES J022351.09-053750.25	1.347	18.61	45.77
DES J033723.98-294917.22	1.351	19.00	45.62
DES J022446.16-050827.57	1.357	18.85	45.69
DES J022436.17-065912.26	1.360	20.78	44.91
DES J022419.74-062142.31	1.361	18.52	45.82
DES J025324.69-002655.67	1.364	19.41	45.47
DES J003922.97-430230.45	1.369	19.71	45.35
DES J024234.93-010351.83	1.371	19.46	45.45
DES J025252.02-002211.61	1.371	20.68	44.96
DES J025318.92+001559.61	1.374	20.92	44.87
DES J002857.80-424644.03	1.377	18.74	45.74
DES J033923.53-265229.48	1.379	20.57	45.01
DES J034027.16-285641.30	1.379	18.74	45.74
DES J004055.63-441249.41	1.383	20.42	45.08
DES J033444.13-264215.40	1.384	19.57	45.42
DES J003738.22-443838.25	1.385	20.13	45.19
DES J025145.09-004639.64	1.386	19.81	45.32
DES J021749.09-041215.57	1.386	20.13	45.19
DES J022815.08-041942.59	1.387	20.10	45.21
DES J024746.99-011334.42	1.389	20.63	44.99
DES J003814.08-433314.92	1.390	18.27	45.94
DES J022032.25-044217.60	1.401	20.25	45.16
DES J021451.07-044236.60	1.401	20.97	44.87
DES J022446.95-055739.13	1.409	20.88	44.91
DES J022402.07-062943.14	1.412	20.17	45.20
DES J022124.53-050205.23	1.415	19.02	45.66
DES J032942.54-272012.09	1.415	19.94	45.29
DES J003827.69-433518.19	1.419	19.96	45.28
DES J022436.64-063255.90	1.423	20.95	44.89
DES J024935.55-001336.76	1.423	19.99	45.28
DES J024606.20-005531.75	1.426	20.38	45.12
DES J003052.76-430301.10	1.428	19.39	45.52
DES J024929.19-002104.15	1.428	19.00	45.67
DES J022216.72-041719.73	1.432	19.89	45.32

Table A2: Mg II sample

DES ID	z	m_r	$\log(\lambda L_{3000})$ (erg s^{-1})
DES J033918.13-293008.14	1.436	21.12	44.83
DES J024340.09-001749.37	1.436	19.68	45.41
DES J024753.20-002137.75	1.437	20.16	45.22
DES J024212.65-010339.46	1.438	20.77	44.97
DES J033435.10-262635.67	1.441	19.45	45.50
DES J021939.92-061407.00	1.446	20.60	45.05
DES J022041.19-055039.80	1.454	20.27	45.19
DES J022006.60-061936.36	1.460	19.83	45.37
DES J033630.87-291753.39	1.462	19.63	45.45
DES J024820.90-002546.67	1.463	19.98	45.31
DES J025030.77-000801.72	1.466	18.31	45.98
DES J002940.83-424308.05	1.472	19.66	45.44
DES J025024.52-001419.03	1.472	19.98	45.31
DES J033310.16-282433.18	1.476	20.99	44.91
DES J003253.01-435626.33	1.476	20.01	45.30
DES J022644.23-040720.13	1.479	19.76	45.41
DES J003035.42-433249.60	1.480	18.77	45.80
DES J024944.09+003317.50	1.480	19.71	45.43
DES J003053.45-432344.99	1.490	20.58	45.09
DES J033213.36-283621.03	1.492	20.36	45.18
DES J003232.61-433303.00	1.492	19.77	45.41
DES J032604.02-275629.36	1.494	18.53	45.91
DES J022429.11-045807.69	1.498	20.30	45.20
DES J003621.41-435139.13	1.501	20.21	45.24
DES J034101.59-293056.44	1.504	20.49	45.13
DES J022350.77-043158.10	1.504	19.90	45.37
DES J021620.91-053417.45	1.508	20.11	45.29
DES J033253.86-283139.33	1.509	20.61	45.09
DES J024959.77-000104.11	1.512	20.09	45.30
DES J024920.97+004206.39	1.524	20.66	45.08
DES J021630.87-042051.45	1.528	19.90	45.39
DES J024455.45-011500.42	1.529	20.51	45.15
DES J033951.49-291713.89	1.530	20.83	45.02
DES J032643.99-280657.07	1.532	19.73	45.46
DES J004232.48-440757.18	1.532	18.38	46.00
DES J003207.44-433049.00	1.533	19.65	45.50
DES J033400.71-271540.89	1.538	20.04	45.35
DES J003254.85-420236.96	1.541	20.28	45.25
DES J022338.53-063246.90	1.546	21.24	44.88
DES J025311.70-004241.62	1.547	20.36	45.23
DES J022059.48-044917.03	1.547	18.51	45.97
DES J033355.67-282651.58	1.551	20.39	45.22
DES J033853.03-271735.34	1.553	21.16	44.91
DES J022509.54-040838.19	1.553	20.43	45.21
DES J003006.53-435107.85	1.555	20.46	45.20

Table A2: Mg II sample

DES ID	z	m_r	$\log(\lambda L_{3000})$ (erg s^{-1})
DES J022520.75-041246.56	1.559	20.38	45.23
DES J022154.21-061941.56	1.559	20.13	45.33
DES J021612.83-044634.12	1.560	19.86	45.44
DES J003433.01-423342.34	1.561	20.28	45.27
DES J033410.83-280949.16	1.562	21.54	44.77
DES J033058.53-275148.31	1.562	20.90	45.03
DES J025318.76+000414.19	1.563	20.15	45.33
DES J033101.15-275125.44	1.563	19.12	45.74
DES J004016.88-442556.16	1.565	20.24	45.29
DES J003829.91-434454.27	1.567	17.83	46.26
DES J003858.70-443045.51	1.569	19.95	45.41
DES J003653.08-435441.53	1.572	19.32	45.67
DES J033211.64-273726.16	1.574	19.22	45.71
DES J033325.92-290142.07	1.574	20.77	45.09
DES J022422.63-061943.20	1.575	21.53	44.78
DES J002939.03-431253.68	1.577	20.70	45.12
DES J033553.51-275044.68	1.578	18.99	45.80
DES J025148.53-004637.61	1.579	19.50	45.60
DES J003413.73-432600.36	1.588	21.23	44.91
DES J022733.98-042523.34	1.590	20.57	45.18
DES J032801.84-273815.71	1.590	20.14	45.35
DES J003952.64-442753.23	1.591	20.03	45.40
DES J003254.79-423926.69	1.597	19.28	45.70
DES J003307.13-424912.19	1.598	20.49	45.22
DES J024603.67-003211.73 [b]	1.601	18.99	45.82
DES J033304.62-291230.05 [b]	1.603	20.19	45.34
DES J024823.76-010002.36	1.603	20.48	45.23
DES J022152.62-062834.38 [b]	1.604	20.96	45.03
DES J033617.72-300224.76 [b]	1.605	19.88	45.47
DES J033604.07-292659.88 [b]	1.610	20.07	45.39
DES J021505.09-045855.98	1.610	19.33	45.69
DES J033721.40-292323.42 [b]	1.612	19.99	45.43
DES J033918.18-293142.92 [b]	1.612	21.04	45.01
DES J033407.62-291607.55 [b]	1.615	19.59	45.59
DES J002950.78-423801.20 [b]	1.616	20.69	45.15
DES J003723.59-442258.09 [b]	1.618	19.98	45.44
DES J033139.43-284939.85	1.619	20.93	45.06
DES J003426.66-422807.96	1.622	21.07	45.00
DES J022016.53-043209.15	1.624	21.22	44.94
DES J025225.52+003405.92	1.624	19.97	45.44
DES J021600.36-043829.30 [b]	1.624	20.33	45.30
DES J033220.31-280214.82	1.625	21.11	44.99
DES J021947.13-043754.70 [b]	1.626	20.63	45.18
DES J033835.80-274224.52 [b]	1.629	20.00	45.44
DES J003501.58-425344.26 [b]	1.632	19.98	45.45

Table A2: Mg II sample

DES ID	z	m_r	$\log(\lambda L_{3000})$ (erg s^{-1})
DES J003454.09-425716.21 [b]	1.633	20.62	45.19
DES J022247.88-043330.04 [b]	1.635	20.24	45.34
DES J003234.33-431937.83 [b]	1.641	19.40	45.68
DES J022224.82-062626.69 [b]	1.641	20.16	45.38
DES J025254.18-001119.67 [b]	1.641	21.25	44.94
DES J022716.52-050008.33 [b]	1.642	20.50	45.24
DES J022337.73-062354.60	1.646	20.91	45.08
DES J034044.75-270720.15	1.647	21.14	44.99
DES J024207.50-004423.41	1.647	22.32	44.52
DES J033437.58-275826.84 [b]	1.648	18.69	45.97
DES J022008.73-045905.31 [b]	1.649	20.52	45.24
DES J033657.91-274244.39 [b]	1.649	20.14	45.39
DES J003015.00-430333.45 [b]	1.650	19.97	45.46
DES J022029.60-051022.59 [b]	1.652	20.68	45.18
DES J024422.20-011247.11	1.654	20.14	45.40
DES J022228.25-060547.60	1.658	20.34	45.32
DES J022319.01-070927.36	1.659	21.32	44.93
DES J003143.64-425420.21 [b]	1.662	20.03	45.44
DES J022208.15-065550.48	1.662	21.12	45.01
DES J003245.74-431453.18	1.671	20.78	45.15
DES J003548.43-431444.38 [b]	1.673	20.47	45.27
DES J022424.16-043229.83 [b]	1.674	20.32	45.34
DES J025340.94+001110.20 [b]	1.675	18.31	46.14
DES J024906.74+000823.79	1.677	20.68	45.19
DES J003956.32-442047.73 [b]	1.680	20.08	45.44
DES J021439.12-051355.34	1.683	20.96	45.08
DES J033903.66-293326.48 [b]	1.684	21.85	44.73
DES J003948.24-445323.16 [b]	1.684	19.59	45.63
DES J025429.12-000404.45	1.685	21.98	44.68
DES J003635.93-434636.05 [b]	1.689	19.90	45.51
DES J025220.53+002735.19 [b]	1.690	19.86	45.53
DES J033341.61-284603.55	1.693	21.02	45.07
DES J021902.58-044628.33 [b]	1.694	19.92	45.51
DES J025356.07+001057.54 [b]	1.695	19.47	45.69
DES J003325.69-434826.13 [b]	1.696	20.26	45.37
DES J024527.72-010602.84 [b]	1.696	20.05	45.46
DES J003030.66-420243.68	1.696	20.65	45.22
DES J033457.77-274956.61	1.700	21.58	44.85
DES J022445.77-061149.99 [b]	1.701	20.19	45.40
DES J003213.12-434553.39	1.706	17.34	46.55
DES J003256.53-441451.15	1.708	19.89	45.53
DES J022907.98-045102.02	1.714	20.91	45.12
DES J022014.98-062253.15 [b]	1.716	19.91	45.52
DES J024207.18-002818.79	1.716	19.83	45.56
DES J003721.82-443051.40	1.716	20.33	45.36

Table A2: Mg II sample

DES ID	z	m_r	$\log(\lambda L_{3000})$ (erg s^{-1})
DES J003221.43-423908.40	1.719	21.21	45.01
DES J024632.55-003439.14 [b]	1.724	19.87	45.55
DES J022134.97-070831.84 [b]	1.728	20.70	45.22
DES J032940.47-275143.61 [b]	1.730	19.87	45.55
DES J022602.20-061626.10 [b]	1.736	19.97	45.51
DES J003734.68-441539.48	1.738	20.15	45.44
DES J024611.20-003134.33	1.738	20.52	45.29
DES J021647.25-044029.81	1.746	21.58	44.87
DES J003206.50-425325.23 [b]	1.750	19.84	45.57
DES J033814.33-294213.78 [b]	1.750	19.94	45.53
DES J002920.73-420425.08	1.750	19.66	45.64
DES J033453.60-264121.34 [b]	1.751	20.14	45.45
DES J033817.74-290324.90 [b]	1.753	19.61	45.67
DES J021732.31-052950.95	1.755	21.84	44.77
DES J033211.80-284257.07	1.755	20.26	45.41
DES J022115.04-043155.51 [b]	1.757	21.33	44.98
DES J033452.89-265215.54 [b]	1.757	19.10	45.87
DES J033451.51-280041.23	1.758	21.49	44.92
DES J022117.44-063856.45 [b]	1.763	19.83	45.58
DES J024140.99-012712.41	1.768	20.33	45.39
DES J024257.19-004549.41 [b]	1.770	21.08	45.09
DES J022119.91-045948.62 [b]	1.770	20.76	45.22
DES J003120.86-425145.98 [b]	1.771	20.14	45.47
DES J002859.58-423239.47	1.776	19.43	45.75
DES J022024.08-045709.48	1.776	19.84	45.59
DES J033912.33-293043.57	1.778	21.35	44.98
DES J004029.04-441704.97 [b]	1.783	20.04	45.51
DES J003255.12-435757.56 [b]	1.784	20.07	45.50
DES J022533.36-065917.56	1.784	18.95	45.95
DES J032759.97-271921.90 [b]	1.785	20.37	45.38
DES J024222.95-011527.57 [b]	1.785	20.24	45.43
DES J032914.81-290130.69	1.787	20.50	45.33
DES J033328.60-290314.66 [b]	1.787	19.58	45.70
DES J022027.32-045115.53 [b]	1.788	21.14	45.08
DES J033922.52-292857.78	1.789	21.27	45.02
DES J022002.08-050101.91 [b]	1.791	19.69	45.66
DES J022751.50-044252.66 [b]	1.795	20.60	45.30
DES J003939.41-444612.90 [b]	1.797	20.17	45.47
DES J022503.11-065258.79 [b]	1.798	20.09	45.50
DES J032835.62-274406.09 [b]	1.800	19.94	45.56
DES J033722.89-274020.85 [b]	1.804	19.93	45.57
DES J003921.57-441844.65	1.813	19.91	45.58
DES J003920.50-440441.16 [b]	1.814	19.79	45.63
DES J003739.59-432521.40 [b]	1.815	20.40	45.39
DES J022231.63-043256.29	1.816	19.67	45.68

Table A2: Mg II sample

DES ID	z	m_r	$\log(\lambda L_{3000})$ ($\mathrm{erg\,s^{-1}}$)
DES J033047.84-281521.39	1.818	21.53	44.94
DES J034001.87-270136.24	1.819	21.05	45.13
DES J004156.96-435856.50	1.821	20.36	45.41
DES J024635.61-000850.46 [b]	1.822	19.26	45.85
DES J033002.51-274858.28 [b]	1.823	20.70	45.27
DES J033017.79-280231.25	1.823	20.61	45.31
DES J033548.18-290943.65 [b]	1.826	20.33	45.42
DES J022352.09-064029.96 [b]	1.827	20.50	45.35
DES J022409.89-044718.00 [b]	1.832	20.11	45.51
DES J033319.58-290431.65 [b]	1.833	20.73	45.27
DES J024716.32-010401.36 [b]	1.834	21.10	45.12
DES J021958.13-041707.68	1.837	21.09	45.12
DES J033222.47-285935.09 [b]	1.837	20.68	45.29
DES J033301.69-275818.80 [b]	1.840	20.94	45.19
DES J004014.18-431716.29 [b]	1.842	19.87	45.62
DES J021643.70-052236.21	1.844	20.57	45.34
DES J021903.49-043935.00 [b]	1.845	20.48	45.37
DES J033539.94-265025.37	1.846	19.68	45.69
DES J024737.50-000458.97 [b]	1.847	19.88	45.62
DES J024608.67-013933.97 [b]	1.848	19.68	45.70
DES J022515.35-044008.91 [b]	1.850	19.82	45.64
DES J025038.68-004739.06 [b]	1.856	18.67	46.10
DES J002729.28-431501.02 [b]	1.863	19.67	45.71
DES J024723.54-002536.48 [b]	1.864	19.42	45.81
DES J022845.57-043350.18 [b]	1.864	17.41	46.61
DES J024748.87-000147.41 [b]	1.868	19.58	45.75
DES J024133.65-010724.20 [b]	1.874	20.86	45.24
DES J003940.80-443718.32 [b]	1.875	19.49	45.79
DES J024838.93-000325.87	1.876	20.61	45.34
DES J022047.63-051835.83 [b]	1.878	19.55	45.77
DES J021544.02-053607.56	1.885	21.31	45.06
DES J025513.03+000639.59	1.885	19.78	45.68
DES J021707.96-055152.07 [b]	1.885	19.70	45.71
DES J033145.20-275435.75 [b]	1.891	21.19	45.12
DES J033225.90-282208.45	1.894	21.55	44.97
DES J022213.31-041030.05	1.903	20.14	45.54
DES J024242.50-002212.87 [b]	1.904	20.57	45.37
DES J022828.19-040044.25 [b]	1.905	18.31	46.28
DES J003626.44-430820.66 [b]	1.907	19.80	45.68
DES J022050.39-061748.80 [b]	1.908	21.89	44.85
DES J021953.45-061123.39 [b]	1.910	19.90	45.64
DES J003150.13-432726.88 [b]	1.912	18.68	46.13
DES J022328.88-040134.71 [b]	1.915	19.82	45.68
DES J033739.88-272045.97 [b]	1.916	19.21	45.92
DES J033924.44-271250.15 [b]	1.918	20.52	45.40

Table A2: Mg II sample

DES ID	z	m_r	$\log(\lambda L_{3000})$ (erg s^{-1})
DES J025428.31+002418.43 [b]	1.918	20.42	45.44
DES J033415.37-265535.62 [b]	1.922	19.85	45.67
DES J033011.77-283636.65 [b]	1.922	20.99	45.21
DES J022327.85-040119.16 [b]	1.922	20.81	45.29
DES J024639.22-012731.85 [b]	1.923	20.34	45.47

Table A3: Properties for our OzDES C IV stacking sample. Columns left to right: DES name (J2000), redshift, r-band apparent AB magnitude, monochromatic luminosity at 1350Å. The superscript b flags sources which also have Mg II data.

DES ID	z	m_r	$\log(\lambda L_{1350})$ (erg s^{-1})
DES J024603.67-003211.73 [a]	1.601	18.99	45.93
DES J033304.62-291230.05 [a]	1.603	20.19	45.45
DES J022152.62-062834.38 [a]	1.604	20.96	45.14
DES J033617.72-300224.76 [a]	1.605	19.88	45.57
DES J033604.07-292659.88 [a]	1.610	20.07	45.50
DES J033721.40-292323.42 [a]	1.612	19.99	45.53
DES J033918.18-293142.92 [a]	1.612	21.04	45.11
DES J033407.62-291607.55 [a]	1.615	19.59	45.70
DES J002950.78-423801.20 [a]	1.616	20.69	45.26
DES J003723.59-442258.09 [a]	1.618	19.98	45.54
DES J021600.36-043829.30 [a]	1.624	20.33	45.41
DES J021947.13-043754.70 [a]	1.626	20.63	45.29
DES J033835.80-274224.52 [a]	1.629	20.00	45.54
DES J003501.58-425344.26 [a]	1.632	19.98	45.55
DES J003454.09-425716.21 [a]	1.633	20.62	45.30
DES J022247.88-043330.04 [a]	1.635	20.24	45.45
DES J003234.33-431937.83 [a]	1.641	19.40	45.79
DES J022224.82-062626.69 [a]	1.641	20.16	45.48
DES J025254.18-001119.67 [a]	1.641	21.25	45.05
DES J022716.52-050008.33 [a]	1.642	20.50	45.35
DES J033437.58-275826.84 [a]	1.648	18.69	46.08
DES J022008.73-045905.31 [a]	1.649	20.52	45.35
DES J033657.91-274244.39 [a]	1.649	20.14	45.50
DES J003015.00-430333.45 [a]	1.650	19.97	45.57
DES J022029.60-051022.59 [a]	1.652	20.68	45.28
DES J003143.64-425420.21 [a]	1.662	20.03	45.55
DES J003548.43-431444.38 [a]	1.673	20.47	45.38
DES J022424.16-043229.83 [a]	1.674	20.32	45.44
DES J025340.94+001110.20 [a]	1.675	18.31	46.25
DES J003956.32-442047.73 [a]	1.680	20.08	45.54
DES J033903.66-293326.48 [a]	1.684	21.85	44.84

Table A3: C IV sample

DES ID	z	m_r	$\log(\lambda L_{1350})$ (erg s^{-1})
DES J003948.24-445323.16 [a]	1.684	19.59	45.74
DES J003635.93-434636.05 [a]	1.689	19.90	45.62
DES J025220.53+002735.19 [a]	1.690	19.86	45.63
DES J021902.58-044628.33 [a]	1.694	19.92	45.61
DES J025356.07+001057.54 [a]	1.695	19.47	45.79
DES J003325.69-434826.13 [a]	1.696	20.26	45.48
DES J024527.72-010602.84 [a]	1.696	20.05	45.56
DES J022445.77-061149.99 [a]	1.701	20.19	45.51
DES J022014.98-062253.15 [a]	1.716	19.91	45.63
DES J024632.55-003439.14 [a]	1.724	19.87	45.65
DES J022134.97-070831.84 [a]	1.728	20.70	45.32
DES J032940.47-275143.61 [a]	1.730	19.87	45.66
DES J022602.20-061626.10 [a]	1.736	19.97	45.62
DES J003206.50-425325.23 [a]	1.750	19.84	45.68
DES J033814.33-294213.78 [a]	1.750	19.94	45.64
DES J033453.60-264121.34 [a]	1.751	20.14	45.56
DES J033817.74-290324.90 [a]	1.753	19.61	45.77
DES J022115.04-043155.51 [a]	1.757	21.33	45.09
DES J033452.89-265215.54 [a]	1.757	19.10	45.98
DES J022117.44-063856.45 [a]	1.763	19.83	45.69
DES J024257.19-004549.41 [a]	1.770	21.08	45.20
DES J022119.91-045948.62 [a]	1.770	20.76	45.32
DES J003120.86-425145.98 [a]	1.771	20.14	45.57
DES J004029.04-441704.97 [a]	1.783	20.04	45.62
DES J003255.12-435757.56 [a]	1.784	20.07	45.61
DES J032759.97-271921.90 [a]	1.785	20.37	45.49
DES J024222.95-011527.57 [a]	1.785	20.24	45.54
DES J033328.60-290314.66 [a]	1.787	19.58	45.80
DES J022027.32-045115.53 [a]	1.788	21.14	45.18
DES J022002.08-050101.91 [a]	1.791	19.69	45.76
DES J022751.50-044252.66 [a]	1.795	20.60	45.40
DES J003939.41-444612.90 [a]	1.797	20.17	45.58
DES J022503.11-065258.79 [a]	1.798	20.09	45.61
DES J032835.62-274406.09 [a]	1.800	19.94	45.67
DES J033722.89-274020.85 [a]	1.804	19.93	45.67
DES J003920.50-440441.16 [a]	1.814	19.79	45.74
DES J003739.59-432521.40 [a]	1.815	20.40	45.49
DES J024635.61-000850.46 [a]	1.822	19.26	45.95
DES J033002.51-274858.28 [a]	1.823	20.70	45.38
DES J033548.18-290943.65 [a]	1.826	20.33	45.53
DES J022352.09-064029.96 [a]	1.827	20.50	45.46
DES J022409.89-044718.00 [a]	1.832	20.11	45.62
DES J033319.58-290431.65 [a]	1.833	20.73	45.37
DES J024716.32-010401.36 [a]	1.834	21.10	45.23
DES J033222.47-285935.09 [a]	1.837	20.68	45.40

Table A3: C IV sample

DES ID	z	m_r	$\log(\lambda L_{1350})$ (erg s^{-1})
DES J033301.69-275818.80 [a]	1.840	20.94	45.29
DES J004014.18-431716.29 [a]	1.842	19.87	45.72
DES J021903.49-043935.00 [a]	1.845	20.48	45.48
DES J024737.50-000458.97 [a]	1.847	19.88	45.72
DES J024608.67-013933.97 [a]	1.848	19.68	45.80
DES J022515.35-044008.91 [a]	1.850	19.82	45.75
DES J025038.68-004739.06 [a]	1.856	18.67	46.21
DES J002729.28-431501.02 [a]	1.863	19.67	45.81
DES J024723.54-002536.48 [a]	1.864	19.42	45.92
DES J022845.57-043350.18 [a]	1.864	17.41	46.72
DES J024748.87-000147.41 [a]	1.868	19.58	45.85
DES J024133.65-010724.20 [a]	1.874	20.86	45.34
DES J003940.80-443718.32 [a]	1.875	19.49	45.89
DES J022047.63-051835.83 [a]	1.878	19.55	45.87
DES J021707.96-055152.07 [a]	1.885	19.70	45.82
DES J033145.20-275435.75 [a]	1.891	21.19	45.22
DES J024242.50-002212.87 [a]	1.904	20.57	45.48
DES J022828.19-040044.25 [a]	1.905	18.31	46.38
DES J003626.44-430820.66 [a]	1.907	19.80	45.79
DES J022050.39-061748.80 [a]	1.908	21.89	44.95
DES J021953.45-061123.39 [a]	1.910	19.90	45.75
DES J003150.13-432726.88 [a]	1.912	18.68	46.24
DES J022328.88-040134.71 [a]	1.915	19.82	45.78
DES J033739.88-272045.97 [a]	1.916	19.21	46.03
DES J033924.44-271250.15 [a]	1.918	20.52	45.51
DES J025428.31+002418.43 [a]	1.918	20.42	45.55
DES J033415.37-265535.62 [a]	1.922	19.85	45.78
DES J033011.77-283636.65 [a]	1.922	20.99	45.32
DES J022327.85-040119.16 [a]	1.922	20.81	45.39
DES J024639.22-012731.85 [a]	1.923	20.34	45.58
DES J022250.47-060104.89	1.925	21.54	45.10
DES J022206.47-060746.70	1.927	20.89	45.36
DES J022514.39-044700.14	1.928	18.83	46.19
DES J034005.69-292312.82	1.928	19.04	46.10
DES J033701.63-282753.94	1.933	20.20	45.64
DES J034016.06-270925.57	1.935	19.72	45.84
DES J033832.50-291215.65	1.935	20.77	45.41
DES J022537.03-050109.34	1.936	20.03	45.71
DES J033316.17-292917.48	1.947	19.95	45.75
DES J033607.36-263207.88	1.948	20.02	45.72
DES J033401.79-265054.28	1.952	19.72	45.84
DES J033232.00-280309.98	1.954	19.98	45.74
DES J025233.79+004340.74	1.954	20.60	45.49
DES J033646.40-291617.17	1.956	20.47	45.54
DES J033052.19-274926.84	1.958	21.49	45.14

Table A3: C IV sample

DES ID	z	m_r	$\log(\lambda L_{1350})$ (erg s^{-1})
DES J033559.60-280324.41	1.965	20.60	45.49
DES J024918.63+000548.34	1.966	20.66	45.47
DES J033650.66-293142.07	1.972	21.68	45.06
DES J032926.49-271844.01	1.978	20.33	45.61
DES J021949.99-064208.13	1.984	19.93	45.77
DES J033839.06-292351.17	1.987	20.33	45.61
DES J025159.70-005159.89	1.988	21.84	45.01
DES J022812.23-043227.58	1.992	21.04	45.33
DES J004016.18-435116.09	1.995	19.98	45.75
DES J033912.95-273516.85	2.006	20.08	45.72
DES J032821.07-282055.17	2.011	19.50	45.95
DES J022352.19-043031.68	2.012	19.75	45.85
DES J033040.28-274203.95	2.013	19.96	45.77
DES J022657.24-035944.42	2.018	20.17	45.68
DES J025019.26+003100.81	2.018	20.26	45.65
DES J022530.19-065458.19	2.030	19.49	45.96
DES J032703.62-274425.27	2.031	19.45	45.98
DES J022034.93-052956.02	2.036	18.20	46.48
DES J034036.10-284811.29	2.039	20.13	45.71
DES J022629.26-043057.07	2.040	20.18	45.69
DES J002959.21-434835.24	2.041	17.77	46.65
DES J022045.50-045121.91	2.045	19.92	45.80
DES J021935.78-064227.17	2.060	21.83	45.04
DES J003146.74-423601.03	2.061	19.54	45.95
DES J033635.40-280828.78	2.067	20.28	45.66
DES J021905.63-055958.78	2.069	20.11	45.73
DES J003549.05-440236.08	2.072	19.23	46.08
DES J021957.25-043952.46	2.077	18.90	46.22
DES J004143.04-440234.42	2.081	20.32	45.65
DES J024453.25-011256.33	2.083	20.73	45.49
DES J024344.30-000201.08	2.083	20.04	45.77
DES J032602.35-281031.00	2.085	20.01	45.78
DES J021850.07-050954.10	2.091	19.52	45.98
DES J021921.81-043642.21	2.092	20.04	45.77
DES J021941.16-044100.36	2.096	21.15	45.33
DES J033015.97-280219.79	2.097	20.18	45.72
DES J004022.52-442820.25	2.100	19.42	46.02
DES J022431.59-052818.78	2.102	17.53	46.78
DES J024628.49-004457.13	2.104	19.94	45.81
DES J003848.52-440202.07	2.105	19.72	45.90
DES J024357.91-005447.75	2.105	21.03	45.38
DES J022044.45-050905.95	2.108	21.19	45.32
DES J025209.79+000549.21	2.108	19.95	45.81
DES J024756.35-001555.92	2.119	18.70	46.32
DES J022813.61-042251.65	2.121	19.63	45.95

Table A3: C IV sample

DES ID	z	m_r	$\log(\lambda L_{1350})$ (erg s^{-1})
DES J033640.29-284423.00	2.124	20.80	45.48
DES J024739.11-005221.01	2.124	20.50	45.60
DES J022411.52-060915.92	2.128	19.82	45.87
DES J024550.79-004328.13	2.131	20.52	45.59
DES J003816.16-434647.44	2.141	19.54	45.99
DES J003936.81-443439.72	2.144	19.97	45.82
DES J022219.46-062539.66	2.146	19.04	46.19
DES J032829.96-274212.23	2.150	20.12	45.76
DES J024632.44-003214.12	2.152	18.89	46.25
DES J021441.86-043709.03	2.152	22.17	44.94
DES J022028.95-045802.58	2.153	20.53	45.60
DES J033326.24-275829.85	2.161	20.53	45.60
DES J022351.07-044729.93	2.163	20.93	45.44
DES J033217.15-271956.41	2.169	19.24	46.12
DES J032923.16-280022.78	2.175	19.77	45.91
DES J002913.21-433044.56	2.180	20.11	45.78
DES J025335.12-003039.26	2.184	20.41	45.66
DES J032939.97-284952.40	2.188	20.22	45.73
DES J024557.22-000823.36	2.199	20.05	45.81
DES J022001.63-052216.92	2.219	20.17	45.77
DES J003320.08-430428.45	2.231	20.19	45.76
DES J024840.78-003548.15	2.235	18.89	46.28
DES J022358.64-045351.63	2.235	20.29	45.72
DES J003448.83-442519.26	2.237	20.13	45.79
DES J033852.79-282256.93	2.246	19.78	45.93
DES J022402.32-061740.34	2.246	19.91	45.88
DES J002907.77-420916.39	2.247	20.77	45.54
DES J024907.29-000649.35	2.251	20.31	45.72
DES J003743.89-434715.68	2.257	19.60	46.01
DES J022725.81-033837.75	2.257	18.20	46.57
DES J021757.52-045059.15	2.257	20.73	45.56
DES J003516.08-432451.82	2.260	19.47	46.06
DES J022557.62-045005.32	2.271	19.55	46.03
DES J022229.62-044941.93	2.275	21.22	45.37
DES J033604.00-274203.95	2.277	21.41	45.29
DES J022729.22-043227.66	2.280	19.75	45.96
DES J033655.83-290218.23	2.283	19.41	46.09
DES J024204.58-003835.64	2.287	20.21	45.77
DES J022451.98-041210.79	2.294	20.14	45.80
DES J022612.64-043401.32	2.306	21.08	45.43
DES J022748.85-042820.90	2.311	20.08	45.84
DES J022410.96-050653.95	2.315	20.66	45.60
DES J024950.74-004224.16	2.317	20.45	45.69
DES J024520.05-004534.45	2.321	20.79	45.55
DES J021730.92-041823.54	2.322	19.75	45.97

Table A3: C IV sample

DES ID	z	m_r	$\log(\lambda L_{1350})$ ($\mathrm{erg\,s^{-1}}$)
DES J033843.76-294922.54	2.328	20.67	45.60
DES J022824.68-041545.71	2.328	19.63	46.02
DES J003436.78-440043.41	2.330	19.58	46.04
DES J025128.73-002650.64	2.330	19.95	45.89
DES J022055.10-061842.21	2.340	21.09	45.44
DES J024337.15-002340.17	2.347	19.36	46.14
DES J033822.77-275910.73	2.349	19.64	46.02
DES J024505.03-003441.97	2.350	20.60	45.64
DES J025033.20+003829.22	2.364	19.96	45.90
DES J004056.56-431446.40	2.384	19.56	46.07
DES J033734.80-294213.92	2.390	19.84	45.96
DES J033953.34-270053.36	2.410	18.53	46.49
DES J003430.47-433311.36	2.415	20.75	45.60
DES J025102.06-004142.78	2.425	22.15	45.05
DES J032942.28-281906.69	2.436	20.42	45.74
DES J033605.57-290354.17	2.450	20.17	45.85
DES J022354.81-044814.94	2.452	18.74	46.42
DES J022014.33-042917.10	2.458	19.30	46.20
DES J024511.94-011317.50	2.462	20.46	45.74
DES J024757.67+001542.65	2.467	20.87	45.57
DES J033430.30-275958.91	2.472	21.32	45.40
DES J022540.58-043825.15	2.477	20.27	45.82
DES J032640.93-283206.80	2.492	20.28	45.82
DES J024717.40-000052.27	2.497	20.30	45.81
DES J003017.36-423144.34	2.497	20.00	45.93
DES J003957.42-434107.92	2.500	20.14	45.88
DES J033237.62-271448.07	2.519	20.30	45.82
DES J033608.10-285245.81	2.522	20.30	45.82
DES J003145.23-424618.45	2.523	20.70	45.66
DES J033545.52-275451.69	2.540	20.28	45.83
DES J003341.34-420811.51	2.541	19.80	46.02
DES J033216.69-272411.37	2.547	19.77	46.04
DES J022259.87-063326.65	2.563	20.60	45.71
DES J003547.38-430558.81	2.565	20.03	45.94
DES J022434.33-043200.27	2.568	20.06	45.93
DES J033518.30-275304.01	2.576	19.33	46.22
DES J003530.07-444539.88	2.587	20.06	45.93
DES J003352.72-425452.55	2.593	19.10	46.32
DES J033331.37-275634.38	2.602	20.37	45.81
DES J024719.59-003313.11	2.607	20.48	45.77
DES J032739.71-281934.84	2.616	20.18	45.89
DES J034121.52-265901.04	2.621	19.44	46.19
DES J021457.21-043011.44	2.636	18.34	46.63
DES J022104.88-060728.52	2.648	20.05	45.95
DES J022631.82-045127.47	2.655	20.77	45.66

Table A3: C IV sample

DES ID	z	m_r	$\log(\lambda L_{1350})$ (erg s^{-1})
DES J022330.15-043004.09	2.677	20.78	45.66
DES J021719.45-052305.27	2.695	19.36	46.23
DES J022034.52-045132.47	2.732	20.40	45.83
DES J033944.09-284604.07	2.744	19.33	46.27
DES J022620.86-045946.48	2.745	21.30	45.48
DES J025223.48-003623.57	2.769	20.20	45.93
DES J033526.38-285747.93	2.770	18.08	46.78
DES J033938.51-291019.54	2.778	21.16	45.55
DES J021921.22-044315.03	2.794	20.17	45.95
DES J022636.07-043428.92	2.801	19.88	46.07
DES J022354.85-054839.89	2.814	19.31	46.30
DES J021659.87-053203.49	2.818	17.60	46.99
DES J022305.97-054015.26	2.823	20.04	46.01
DES J022321.26-055600.27	2.846	21.55	45.42
DES J022255.51-044410.32	2.871	20.31	45.92
DES J033720.58-272434.70	2.896	20.16	45.99
DES J003255.24-430948.41	3.010	19.57	46.26
DES J022423.43-070627.92	3.030	21.48	45.50
DES J003318.29-434301.10	3.082	19.31	46.38
DES J033246.76-280846.78	3.180	19.17	46.47
DES J021438.15-052024.38	3.214	20.93	45.77
DES J025250.10+000830.68	3.237	20.27	46.04
DES J003133.50-422953.97	3.248	20.62	45.90
DES J021906.24-041933.94	3.330	21.60	45.54
DES J033712.16-285146.74	3.364	20.33	46.06
DES J003411.44-424329.48	3.373	20.83	45.86
DES J002926.44-420752.35	3.403	19.71	46.32
DES J022543.53-042834.48	3.411	20.64	45.95
DES J024325.96-003145.11	3.435	19.63	46.36
DES J022133.35-065713.47	3.440	20.16	46.15
DES J034122.60-291302.04	3.470	20.33	46.09
DES J033512.61-292351.14	3.712	19.98	46.27
DES J024509.76-010001.28	3.807	20.58	46.05
DES J022144.21-062745.18	3.856	20.14	46.24